Quantum Dot Microlasers subject to Delayed Optical Feedback

vorgelegt von
M. Sc.
Steffen Karl Holzinger
ORCID: 0000-0001-7476-5506

von der Fakultät II - Mathematik und Naturwissenschaften
der Technischen Universität Berlin
zur Erlangung des akademischen Grades

Doktor der Naturwissenschaften
Dr. rer. nat.

genehmigte Dissertation

Promotionsausschuss:
Vorsitzender: Prof. Dr. Michael Lehmann
Gutachter: Prof. Dr. Stephan Reitzenstein
Gutachter: Prof. Dr. Gian Luca Lippi
Tag der wissenschaftlichen Aussprache: 29.10.2019

Berlin 2019

Kurzdarstellung

Halbleiterlaser reagieren sehr empfindlich auf die Rückkopplung ihrer eigenen Lichtemission. Während entsprechende Laserreflektionen in vielen Anwendungen als nachteilig angesehen werden, ist die zugrunde liegende Physik schon seit vielen Jahren ein wichtiges und attraktives Forschungsthema im Feld der nichtlinearen Dynamik. Bisher wurde die komplexe Dynamik solcher rückgekoppelter Halbleiterlaser sowohl in der Theorie als auch in Experimenten hauptsächlich im klassischen Regime bei Lichtleistungen im Bereich von mW und darüber untersucht. Im Vergleich dazu stellen nichtlineare Rückkopplungseffekte im Bereich geringer Lichtleistungen und vor allem das Quantenregime einzelner Photonen weitestgehend unerforschtes wissenschaftliches Neuland dar. Elektrisch betriebene Quantenpunkt-Mikrosäulenlaser bieten in diesem Zusammenhang eine vielseitige Technologieplattform, um Rückkopplungsexperimente im Regime der Kavitäts-Quantenelektrodynamik zu realisieren. Sie erlauben es damit erstmals, eine Brücke zwischen den Forschungsfeldern der Nanophotonik und der nichtlinearen Laserdynamik zu etablieren. Hier bekommen insbesondere die Effekte einzelner Emitter sowie zusätzliches Rauschen aufgrund einer hohen Rate der spontanen Emission in die Lasermode eine zentrale Bedeutung.

In der vorliegenden Arbeit untersuchen wir nichtlineare dynamische Effekte in Quantenpunkt-Mikrolasern mit hohen Kopplungseffizienzen der spontanen Emission unter externer optische Rückkopplung. Dies beinhaltet zunächst den Einfluss optischer Rückkopplung sowohl auf das optische Spektrum als auch auf die Photonenstatistik der Mikrolaser. Von besonderem Interesse ist der bimodale Charakter der untersuchten Mikrosäulenresonatoren, in denen zwei linear, orthogonal zueinander polarisierte Moden um das gemeinsame Verstärkungsmedium konkurrieren, was zu einem stochastischen Umschalten zwischen den Moden oberhalb der Laserschwelle führen kann. In Gegenwart einer externen Kavität im inkohärenten Regime, das heißt mit einer Rückkopplungszeit oberhalb der Kohärenzzeit des Mikroasers, untersuchen wir experimentell den Einfluss des Pumpstroms und der Rückkopplungs-

stärke auf diese Modendynamik, welche über die numerische Modellierung durch ein semi-klassisches Ratengleichungsmodell erfolgreich beschrieben wird. Entsprechend theoretisch abgeleitete Vorhersagen können wiederum als Richtlinien für die Empfindlichkeit von Mikrosäulenlasern gegenüber externer optischer Rückkopplung genutzt werden. Zusätzlich zur Untersuchung der Laserdynamik mittels Autokorrelationsmessungen wird die Photonenzahl-Verteilung der Emission auch direkt mittels eines kalorimetrischen Detektors aufgenommen, was eine Untersuchung des Einflusses der Rückkopplungseffekte auf die Modenstabilität zulässt.

Darüber hinausgehend wird die zeitverzögerte, kohärente Rückkopplung für den Grenzfall einer kurzen externen Kavität analysiert. Hierbei wird der Einfluss der Länge der externen Kavität, die vergleichbar mit der Kohärenzlänge des Mikrolasers ist, auf spektrale und dynamische Eigenschaften des Mikrosäulenlasers untersucht. Dabei wird insbesondere der Übergang von kohärenter zu inkohärenter Rückkopplung erforscht, was eine detaillierte Studie des Einflusses der Phase des rückgekoppelten Lichts beinhaltet. Des Weiteren bestimmen wir die Relaxationsoszillations-Frequenz von Mikrosäulenlasern verschiedener Durchmesser, indem wir in den Mikrolaser im Gleichstrombetrieb einen externen optischen Puls injizieren. Diese Frequenz stellt eine wichtige Gütezahl in der theoretischen Beschreibung der Anschalt- und Rückkopplungsdynamik von Lasern dar. Man kann den optischen Puls zusätzlich nutzen, um den rückgekoppelte Laser auf den rückkopplungsfreien Zustand zurückzusetzen. Das System kehrt dann nach einem Umlauf des Emissionspulses in der externen Kavität in den „stationären“ Rückkopplungszustand zurück.

Schließlich wird ein vielseitiger Messaufbau vorgestellt, der sowohl laterale als auch axiale Anregung und Detektion ermöglicht. Hiermit kann der Linienverbreiterungsfaktor α erstmals in Abhängigkeit des Pumpstroms für Mikrolaser bestimmt werden. Dieser ist ein weiterer wesentlicher Parameter für die Beschreibung spektraler und dynamischer Eigenschaften von Halbleiterlasern. Die vorgestellte Methode basiert dabei auf einer direkten Messung der Änderung der Verstärkung des Lasers sowie seines Emissionsspektrums unter optischer Rückkopplung. Dieses Verfahren ist daher nicht nur verheißungsvoll für Quantenpunkt-Mikrolaser, sondern auch für Nanolaser im Allgemeinen. Der vorgestellte Ansatz wird durch einen Vergleich mit etablierten Methoden zur Bestimmung von α sowie einem quantenoptischen Modell evaluiert. Darüber hinaus wird die entwickelte Messkonfiguration verwendet, um eine gleichzeitige laterale optische Injektion und axiale Rückkopplung zu ermöglichen. Es wird

gezeigt, dass die Rückkopplung zur Verstärkung des Rauschens in der Lasermode führt, was wiederum zu einem vergrößerten Bereich von teilweise synchronisierter Emission führt. Letzteres ist ein interessantes Phänomen, das durch einen hohen Anteil spontaner Emission erklärt werden kann, die in der Kavität verstärkt wird.

Die vorgestellten Resultate vermitteln ein tiefes Verständnis für Rückkopplungsphänomene in Mikrosäulenlasern in der neuartigen Region ultrageringer Lichtleistungen im Bereich von nW bis μW. Durch die Bestimmung verschiedener wichtiger Parameter können die Voraussetzungen ermittelt werden, die für eine gezielte Manipulation der Photonenstatistik und Dynamik von Mikrolasern mit hohem β-Faktor erforderlich sind. Darüber hinaus sind diese Untersuchungen nahe dem Quantenlimit wegweisend für zukünftige Studien zur externen Kontrolle von nanophotonischen Quantensystemen.

Abstract

Semiconductor lasers have been found to be extremely sensitive to back reflections of there own light emission. While corresponding laser reflections are mostly considered a disturbance for many applications, their underlying physics have been an important and attractive research topic in the field of nonlinear dynamics for many years. So far the complex dynamics of feedback-coupled semiconductor lasers have been investigated both theoretically and experimentally mainly in the classical regime at optical output powers on the order of 1 mW and above. In comparison, nonlinear feedback effects in the region of low light intensities and especially the quantum regime of single photons constitute new scientific territory. In this regard, electrically pumped quantum dot micropillar lasers provide a versatile technology platform for the realization of delay-coupled experiments in the field of cavity quantum electrodynamics. Therefore, they allow for the first time to establish a bridge between the scientific fields of nanophotonics and nonlinear laser dynamics. Here, single emitter effects and additional noise contributions caused by a high rate of spontaneous emission into the lasing mode become of significant importance.

In this thesis, we examine nonlinear dynamical effects in quantum dot microlasers with high spontaneous emission coupling efficiencies in the presence of external optical feedback. This includes the influence of optical feedback on both the optical spectrum as well as the photon statistics of the microlaser. It is of particular interest to investigate the bimodal character of the micropillar resonators, in which two linear, orthogonally polarized modes compete for a common gain medium resulting in characteristic switching dynamics above the lasing threshold. In the presence of an external cavity in the incoherent regime, i.e. with a delay time greater than the coherence time of the microlaser, we experimentally investigate the influence of different pump current conditions and varying feedback strength on these mode dynamics, which are successfully described via numerical modeling with a semi-classical rate equation model. The corresponding theoretically deduced predictions in turn

can be used as general guidelines for the sensitivity of micropillar lasers to optical feedback. In addition to investigations of the laser dynamics with autocorrelation measurements, we record the photon-number distribution of the emission directly with a transition-edge sensor detector, which allows an analysis of the feedback effects on the stability of the modes.

Afterwards, we examine delayed coherent feedback in the limit of a short external cavity. Here, one studies the influence of the external cavity length, which is similar to the microlaser's coherence length, on the spectral and dynamical properties of the micropillar laser. In particular, the transition from coherent to incoherent feedback is investigated including a detailed analysis of the phase sensitivity of the feedback-coupled light. Furthermore, we extract the relaxation oscillation frequency of micropillar lasers of different diameters by superimposing optical pulse injection to the direct current. This frequency is a crucial figure of merit in the theoretical description of the turn-on and feedback dynamics of lasers. Additionally, the optical pulse can be used to reset the feedback-coupled laser so that it reaches the same state as if no feedback was present. The system returns to the "stationary" feedback condition after one cavity round-trip of the emission pulse.

Finally, we introduce a versatile experimental setup that allows for simultaneous lateral and axial excitation and detection. We hereby determine the linewidth enhancement factor α in dependence of the pump current for the first time in microlasers. This is another crucial parameter for describing the spectral and dynamical properties of semiconductor lasers. The presented method is based on a direct measurement of variations in the laser gain and emission spectrum when subject to delayed optical feedback. Therefore, this technique is not only promising for quantum dot micropillar lasers but also high-β nanolasers in general. Our approach is evaluated by comparing it to established conventional methods of determining α as well as numerical simulations based on a quantum optical model. Additionally, this configuration is exploited for simultaneous lateral optical injection and axial feedback. Here feedback-coupling is shown to enhance the noise in the lasing mode leading to a wider range of partial injection locking. The latter is an interesting phenomenon that is understood by the high spontaneous emission rate which is enhanced in the cavity.

The presented results provide a deeper understanding of feedback-induced phenomena in micropillar lasers in the novel region of ultra-low light powers on the

order of nW to μW. By extracting several crucial system parameters, we obtain the requirements for tailoring the photon statistics and nonlinear dynamics of high-β microlasers. Moreover, the investigations close to the quantum limit pave the way for future studies on the external control of nanophotonic quantum systems.

Contents

1 Introduction

The demonstration of the first laser in 1960 by Theodore Maiman [Mai60] is one of the greatest success stories in science and technology. It initiated extensive research activities in this topic which led to a broad presence in technology with a market value of US$ 7 Billion in 2017 [Ima17]. Lasers (which is an acronym for **l**ight **a**mplification by **s**timulated **e**mission of **r**adiation) are sources of coherent light which find widespread application use not only in consumer electronics but also in medical systems and natural sciences. Already in 1962 there were several reports of semiconductor lasers based on GaAs [Hal62, Nat62, Hol62] which is still a material system of choice today. Yet, these first homostructure devices, which were operated at liquid nitrogen temperature, suffered from very high lasing threshold current densities of $J_{\mathrm{th}} = 10\text{-}50\ \frac{\mathrm{kA}}{\mathrm{cm}^2}$ [Hay70] which made them incapable of performing continuous-wave (CW) operation. The first crucial step to tackle this issue was the invention of advanced semiconductor lasers based on double heterostructures in 1969 by Zhores Alferov [Alf69] which led to the Nobel Prize in 2000. This way one could not only achieve a higher density of injected charge carriers but also optical and electronic confinement [Alf96] which led to the realization of the first room-temperature CW semiconductor laser with $J_{\mathrm{th}} \sim 1\ \frac{\mathrm{kA}}{\mathrm{cm}^2}$ in 1970 [Alf70].

Since then significant effort has been undertaken to reduce the size and power consumption of semiconductor lasers. Here vertical-cavity surface-emitting lasers (VCSELs) have been found to be a key component for so called "green photonics" [Eis17]. It was perceived in the early 1990s that these two goals can be jointly achieved as the reduction of at least one dimension of a resonator on the order of the wavelength of light leads to an increase of the optical density of states of the laser mode [Yok92]. By reducing the resonator size, the gain medium can couple to fewer optical modes, which increases the spontaneous emission factor β, that describes the fraction of spontaneous emission coupled into the lasing mode [Yam91, Ma19]. In such lasers a large amount of spontaneous emission is funneled into the lasing mode

reducing the threshold power to achieve stimulated emission [Nod06] by reducing photon losses into leaky modes. In the limiting case $\beta \to 1$ so-called *thresholdless lasing* is reached, which occurs when every photon spontaneously emitted by the gain medium is coupled into the lasing mode [Kha12].

Additionally, semiconductor lasers are close to ideal candidates to explore the complex temporal dynamics of feedback-coupled nonlinear oscillators in table-top experiments [Lan80, Sor13]. These dynamics have been studied extensively in the regime of classical lasers with at least $\sim 1\,\mathrm{mW}$ output power [Sci15] which led to deep insight into the underlying physics and paved the way for numerous applications ranging from ultra-fast random number generation [Uch08] to chaos communication [Fis00]. In contrast, only sparse research has been devoted to miniaturized semiconductor lasers with high β-factors leaving open the question about the limit of feedback effects in the few photon regime.

The system of choice to explore the interesting physics, that is located at the crossroads between the important research fields of nanophotonics, quantum optics and nonlinear dynamics, are quantum dot (QD) micropillar lasers. Their small dimensions result in high β-factors of 10^{-3} to 10^{-1} and single-mode operation with intrinsic dynamics that originate from oscillation on two different states of polarization in case of bimodal micropillars. Micropillar lasers resemble VCSELs which exhibit fascinating dynamics like low frequency fluctuations [Nau03] and even polarization chaos [Vir12]. Moreover, micropillars with only few quantum dots as gain medium are widely used in the field of quantum nanophotonics. This includes for instance the demonstration of weak coupling [Gér98] and strong coupling [Rei04] in the regime of cavity quantum electrodynamics (cQED). Additionally, the system of a QD in a cavity can be used for the generation of triggered sources of single indistinguishable photons [San02, Gaz13, Din16, Uns16]. Beyond that, by either increasing the pump rate or the QD density, one can investigate the transition to lasing in QD micropillars [Gie17] as well as superradiant emitter coupling [Kre17]. Regarding nonlinear dynamics, high-β systems show noise-enhanced nonlinear phenomena that can result for instance in partial locking [Sch16], which has been shown explicitly for QD micropillar lasers, as well as spontaneous symmetry breaking [Ham15] or even extreme events [Sel16].

There are two early works [Alb11, Hop13] that paved the way for investigating QD microlasers in the presence of time-delayed optical feedback. In particular, they

give insight into a feedback induced change in the photon statistics. It has to be highlighted that these publications only depict a very limited range of parameters. Consequently, this work aims at providing a comprehensive and profound understanding of the feedback effects on the underlying intrinsic switching dynamics of the micropillar in a wide parameter range. By describing the experimental data by numerical modeling, we obtain important insight into the involved physical processes and trends can be extrapolated, thus, clarifying what parameters are relevant for sensitivity to optical feedback. The obtained knowledge can be applied for controlling of the system's dynamics which is vital for aforementioned applications which could be expanded by integrated photonic circuits [Bau04, Too15]. Moreover, feedback experiments are exploited to obtain deeper insight into intrinsic parameters of the QD micropillar lasers such as the relaxation oscillation frequency and the linewidth enhancement factor which were determined for the first time for cavity-enhanced microlasers. These in turn are very useful for a more accurate numerical modeling and prediction of the laser dynamics which can lead to design rules for optimized nanophotonic devices to explore the quantum regime of optical feedback in the future.

This dissertation is structured as follows: Chapter 2 explains the fundamental physics relevant for understanding the experimental studies in is thesis. In particular, this includes semiconductor QDs which serve as active medium for the microlasers that are investigated. Subsequently, we discuss optical microcavities. Here, the basic concepts of cavity quantum electrodynamics are introduced that highlight the effects of miniaturization and mode confinement with regard to spontaneous emission coupling to the cavity mode. Then, photon statistics is introduced which enables a distinction between non-classical, thermal and coherent light sources. This important quantum optical characteristic is needed to prove lasing in high-β devices in an unequivocal manner. Finally, the effects of optical feedback are highlighted for semiconductor lasers in a basic theory and the transition towards microlasers is sketched.
Chapter 3 describes the nano-fabrication of the QD microlasers investigated in this work. Furthermore, all experimental methods used to determine their spectral and dynamical properties are depicted. Finally, a transition-edge sensor system is presented that enables a direct measurement of the photon-number distribution of

emission.

In chapter 4 bimodal QD microlasers are investigated in the presence of incoherent time-delayed feedback. This comprises a detailed experimental and theoretical analysis of the parameters that are required for a QD microlaser to be sensitive to optical feedback. First, the input-output characteristics and second-order autocorrelation are measured. Subsequently, the photon-number distribution is measured directly to investigate the effect of feedback on the stability of the lasing modes. Furthermore, the alignment procedure of the external cavity and the implications on its precision with regard to feedback strength are discussed.

In chapter 5 the analysis of feedback-coupled QD microlasers is extended towards coherent feedback from a short external cavity. By varying the cavity length, it is possible to examine the limits of the expected phase sensitivity in this regime. Additionally, optical pulse injection is used to investigate the turn-on dynamics of the lasers. Adding optical feedback, we find that the optical pulse resets the system to its solitary state only building the feedback-coupled state after one external cavity round-trip.

Chapter 6 presents a 90° excitation and detection scheme highlighting the benefits simultaneous lateral and axial optical access to the micropillar laser. First, this setup is used as a novel method of determining the linewidth enhancement factor α which is an important parameter for predicting the spectral and dynamical properties of semiconductor lasers. Here, the lateral access to the micropillar is used to obtain insight into the modification of the modal gain by feedback coupling. In a second experiment this scheme is utilized for simultaneous lateral injection locking and axial optical feedback. We can not only show that injection locking is possible in this lateral configuration but also that optical feedback is able to increase the locking range.

In chapter 7 the thesis closes with an outlook on the progress towards feedback-coupled nanophotonic quantum systems. Here first results on microlasers with a defined low number of QDs are depicted. These structures are very promising as they represent a further step towards the quantum limit of optical feedback. In this context, theory proposals evaluating single-photon feedback are discussed, which are based on fully quantum-mechanical simulations.

2 Theoretical background

This chapter introduces the theoretical background of the technology and experiments discussed in this dissertation. First, section 2.1 presents the electronic structure of semiconductor QDs. Afterwards, section 2.2 discusses optical microcavities in in the micropillar geometry and the basics of cQED. Subsequently, section 2.3 explains the statistical properties of light. Here, both correlation functions as well as the underlying photon-number distributions are discussed. Section 2.4 explains the peculiarities of high-β lasing, highlighting striking differences in comparison to macroscopic semiconductor lasers. Finally, section 2.5 introduces the concept of delayed optical feedback. A basic theory for classical semiconductor lasers is presented and modifications in the transition to high-β microlasers are highlighted.

2.1 Semiconductor quantum dots

Semiconductor QDs are high-quality crystalline clusters of hundreds to thousands of atoms in which the motion of electrons is quantized in all three directions [Fox06]. This quantization arises as the dimensions of a QD are comparable to the de Broglie wavelength of the charge carriers [Mic09], which causes their electronic structure to be discrete, resembling artificial atoms [Gér01]. In this work, we are interested in QDs based on the direct band gap ternary semiconductor InGaAs, which is embedded in a 3D matrix of GaAs. Comparing the strain-free band gap energy E_{gap} of the two materials ($E_{\mathrm{gap}}^{\mathrm{InAs}} \simeq 0.35\,\mathrm{eV} \ll E_{\mathrm{gap}}^{\mathrm{GaAs}} \simeq 1.42\,\mathrm{eV}$ at room temperature [Vur01]) explains the confinement of the charge carriers in such a structure. The QDs are epitaxially grown in the Stranski-Krastanow mode which is explained in more detail in section 3.1. It has to be noted that the formation of a QD is accompanied by a so called *wetting layer* which is a strained two-dimensional quantum well with a thickness of a few monolayers [Sęk06] forming at the GaAs/InGaAs interface. Moreover, it has to be noted that the following description of the electronic structure only

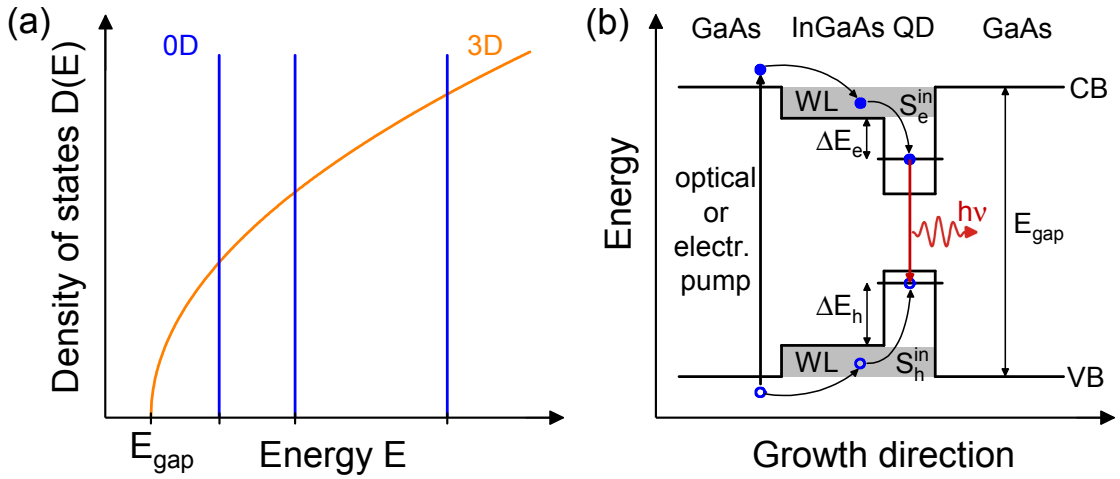

Figure 2.1: (a) Comparison of electronic density of states $D(E)$ of charged carriers in a bulk semiconductor (orange, 3D) and a QD (blue, 0D). (b) Electronic band structure of an InGaAs QD embedded in a GaAs matrix. By applying an optical or electrical pump an electron is created in the conduction band (CB) and a corresponding hole in the valence band (VB). By non-radiative phonon-assisted relaxation processes the electron and hole are scattered into the QD ground state via the wetting layer (WL, scattering rate $S_{\mathrm{e,h}}^{\mathrm{in}}$). The confined electron and hole can recombine radiatively (with a high quantum efficiency $>90\,\%$ at cryogenic temperatures) emitting a photon with an energy $h\nu$ (red).

comprises the relevant physics needed to describe lasers based on QDs as an active medium. More detailed information can be found in books dedicated to this topic (e.g. [Bim99, Mic09]).

Figure 2.1 (a) depicts the electronic density of states (DOS) $D(E)$ of a QD which is a quasi-zero-dimensional object in comparison to the DOS of a three-dimensional bulk semiconductor. The latter exhibits a continuous DOS with $D(E) \propto \sqrt{E}$. The quantization in all directions of motion in case of the QD leads to a discrete density of states with $D(E) \propto \delta(E - E_i)$ where δ denotes the Dirac delta-function. Moreover, E_i is the energy of the discrete levels in a QD potential well with quantum number i. It is underlined that the number of energy levels within a QD depends on the depth of the QD potential well and the quantization energy which are determined by the material composition, the local strain and size of the QDs, respectively. The following discussion will be restricted only to the ground state of the QD (for simplicity this work only investigates ground state lasing, while in reality also higher excitations such as bi-excitonic levels may contribute to lasing [Cha04]) which is

approximated by a simple two-level system.

Figure 2.1 (b) illustrates the simplified electronic structure of a QD (only showing the ground state). By electrical current injection, which constitutes off-resonant above band gap excitation, one creates free carriers in the vicinity of the QD so that electrons in the conduction band and holes in the valence band can scatter non-radiatively via phonon generation first into the wetting layer and subsequently into the QD. The resulting QD exciton recombines with high probability (quantum efficiency $>90\,\%$ [Joh08]) radiatively, i.e. by emission of a photon with an energy $h\nu$.

One has to note that the scattering rates for electrons and holes from the wetting layer into the QD $S_{\mathrm{e,h}}^{\mathrm{in}}$ are important figures of merit to accurately describe the dynamics of a laser based on QDs via semi-classical rate equations (see Appendix A.1). These rates can be calculated from a microscopic description of the Coulomb interaction between the carrier reservoir of the wetting layer and the QD [Lüd12]. In quantum optical models that work with microscopic descriptions of a QD (see Appendix A.2) the electron (hole) energetic distance of confined electron (hole) states $\Delta E_{\mathrm{e,h}}$ to the conduction (valence) band edge of the wetting layer is an important parameter. For $In_{0.3}Ga_{0.7}As$ QDs ΔE_{e} is found to be $\sim 10\,\mathrm{meV}$ while ΔE_{h} is larger (here $\sim 19\,\mathrm{meV}$) as the energy level of the ground state in a potential well is inversely proportional to the mass of a particle. It has to be considered that these values are highly dependent on the material composition of the QD.

2.2 Optical microcavities

Optical microcavities constitute an advantageous platform to confine light to small mode volumes on the order of the cubic wavelength of light $V \sim (\frac{\lambda}{n})^3$ [Vah03]. While there are several different realizations of these microcavities such as microdisks [McC92], microspheres [Col93] or photonic crystal cavities [Ell07], this thesis focuses on micropillar cavities which facilitate the formation of an external cavity normal to the sample surface and easy access the emission features of the QD gain medium under lateral detection. Moreover, micropillars can be contacted in a straightforward way which relaxes the experimental complexity in feedback experiments.

2.2.1 Micropillar cavities

Micropillar cavities are column-shaped devices which form a Fabry-Pérot cavity by two highly reflective distributed Bragg reflectors (DBRs) consisting of two alternating materials with different refractive index. The layer thickness d_{DBR} is chosen so the following equation is fulfilled [Sko98]:

$$d_{\mathrm{DBR}} = \frac{\lambda_{\mathrm{DBR}}}{4n}, \tag{2.1}$$

where λ_{DBR} is the central wavelength of the stop-band created by the DBR and n is the effective refractive index of the used material. The working principle of a DBR can be explained by the physics of partial light reflection at material interfaces with different refractive index. At the interface of a medium with refractive index n_1 (here GaAs) and a medium with smaller refractive index n_2 (here AlAs) incident light is partially reflected without phase change. In the case of reflection occurring at an interface with $n_2 > n_1$, one yields a phase shift of π [Hec17]. Therefore, using alternating layers that fulfill equation 2.1, one achieves constructive interference of the light partially reflected by layers of the DBR and destructive interference of light transmitted through them. The reflectivity R of such a structure at normal incidence is given by [Sal95]:

$$\sqrt{R} = \frac{1 - \frac{n_s}{n_0}\left(\frac{n_1}{n_2}\right)^{2m}}{1 + \frac{n_s}{n_0}\left(\frac{n_1}{n_2}\right)^{2m}}, \tag{2.2}$$

where m is the number of mirror pairs while n_0 and n_s describe the refractive index of the medium below and above the DBR (e.g. GaAs and air). Taking into account the refractive indices $n_{\mathrm{GaAs}} \simeq 3.5$ and $n_{\mathrm{AlAs}} \simeq 2.9$ [Ada85], one yields R close to unity when using more than 20 of such $\frac{\lambda}{4}$-thick mirror pairs.

While an ideal microcavity would be able to store light endlessly at δ-function-like resonance frequencies, one can describe deviations from this ideal condition by the quality (Q) factor [Vah03]. The Q-factor describes the ability of a resonator to store light and can be expressed by [Gér98]:

$$Q = \omega_{\mathrm{res}}\tau_{\mathrm{res}} = \frac{E_{\mathrm{res}}}{\Delta E} = \frac{\lambda_{\mathrm{res}}}{\Delta\lambda}, \tag{2.3}$$

where ω_{res} is the angular resonance frequency of the resonator and τ_{res} is the lifetime of a photon in the resonator. This can be rewritten in terms of the optical spectrum, namely the resonance energy (wavelength) E_{res} (λ_{res}) and the linewidth of the resonator mode ΔE ($\Delta\lambda_{\mathrm{res}}$). Here the Q-factor is not only limited by losses through the cavity mirrors with $R<1$. Additionally, in the small diameter regime $\lesssim 3\,\mu\mathrm{m}$ micropillar cavities suffer from scattering of light at the sidewalls [Rei11]. Moreover, optical absorption by the cavity material and the active medium has to be taken into account [Rei07, Kar09].

2.2.2 Cavity quantum electrodynamics

CQED deals with modifications of the spontaneous emission of two-level emitters due to their interaction with discrete optical modes of small mode-volume cavities [Yam00].

In the previous section we have discussed the case of a passive empty cavity. Utilizing a microresonator as the basis of a laser device is possible by adding an active medium. In this work we focus on an active medium consisting of semiconductor QDs which can be effectively treated as two-level emitters. Moreover, we consider the regime of *weak coupling* in which the emitter-cavity coupling rate g is smaller than the dissipative loss rates, which include mainly photon losses from the cavity mode γ_{c} [Fox06]. Here spontaneous emission of an emitter is not reversible and can be described by Fermi's golden rule of an electric dipole transition [Gér98]:

$$\gamma_{\mathrm{r}} = \frac{1}{\tau_{\mathrm{sp}}} = \frac{4\pi}{\hbar}\rho(\omega)\left\langle|\boldsymbol{d}\cdot\boldsymbol{\epsilon}(\boldsymbol{r})|^2\right\rangle, \tag{2.4}$$

where γ_{r} is the spontaneous emission rate, τ_{sp} is the spontaneous emission lifetime, $\rho(\omega)$ is the optical mode density at the emitters' angular frequency ω and $\langle|\boldsymbol{d}\cdot\boldsymbol{\epsilon}(\boldsymbol{r})|\rangle$ is the dipole matrix element (variables in bold print are vectors). The implications of this equation are highlighted by Fig. 2.2. Panel (a) sketches (for simplicity) one emitter in the center of a microcavity which is formed by two mirrors. The photonic mode density $\rho(\omega)$ is different when comparing the case of free-space spontaneous emission with $\rho(\omega)\propto\omega^2$ and a single-mode cavity (Lorentzian function) [Fox06], which is highlighted in panel (b). This implies that the spontaneous emission rate can be significantly increased by putting an emitter in (spatial and spectral) reso-

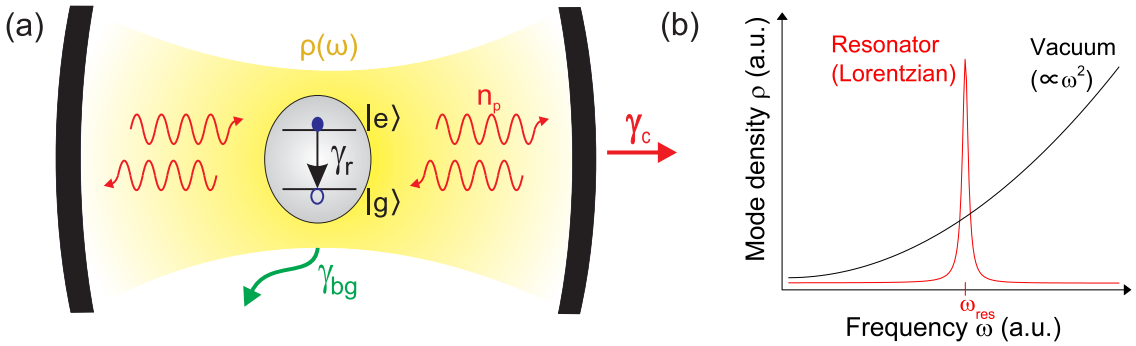

Figure 2.2: (a) Illustration of a two-level emitter with ground state $|g\rangle$ and excited state $|e\rangle$ in an optical cavity. Two mirrors (black) form a resonator with a photonic mode density $\rho(\omega)$ of the optical field (yellow). (b) Comparison of the photonic mode density $\rho(\omega)$ in free space and in a resonator. By spectrally matching the emitter with ω_{res} one yields an increased mode density.

nance with the optical mode of the microresonator and reduced otherwise. Consequently, the lifetime is reduced on resonance, while the opposite case of an increased lifetime can be found when the emitter is strongly "off-resonance" [Bay01].

The ratio of the lifetimes in free space and the one in the cavity is termed Purcell factor F_{P} [Pur46]. In comparison to the original formulation, we have to take into account that the emitter is located in a medium with refractive index n. Therefore, the upper limit of the Purcell factor of a spatially and spectrally resonant emitter is given by [Gér98]:

$$F_{\mathrm{P,\,max}} = \frac{3}{4\pi^2}\left(\frac{\lambda_{\mathrm{res}}}{n}\right)^3 \frac{Q}{V}. \tag{2.5}$$

In order to get a general expression for F_{P}, it has to be considered that an emitter can exhibit a finite detuning Δ from the cavity resonance. Moreover, the electric field at the place of the emitter $\boldsymbol{E}(\boldsymbol{r})$ does not necessarily coincide with the maximum of the electric field $\boldsymbol{E}_{\mathrm{max}}$ (in the center in case of a one λ thick cavity [Kav07]). Therefore, one yields the following modification compared to equation 2.5 [Gay03]:

$$F_{\mathrm{P}} = F_{\mathrm{P,\,max}} \cdot \frac{\gamma_{\mathrm{c}}^2}{4\Delta^2 + \gamma_{\mathrm{c}}^2} \cdot \frac{|\boldsymbol{E}(\boldsymbol{r})|^2}{|\boldsymbol{E}_{\mathrm{max}}|^2}. \tag{2.6}$$

Before discussing possible strategies to increase the Purcell factor, we introduce the spontaneous emission coupling factor β, which is given by the fraction of spontaneous emission (SE) coupled into the cavity mode to the total SE. While an ideal

cavity yields a β factor of one, we have to take into account that the direction of spontaneous emission is per se random causing emission into other modes γ_{bg} [Fox06]:

$$\beta = \frac{\text{SE rate into cavity mode}}{\text{total SE rate}} = \frac{\gamma_{\mathrm{r}}}{\gamma_{\mathrm{r}} + \gamma_{\mathrm{bg}}} \cong \frac{\overline{F_{\mathrm{P}}}}{\overline{F_{\mathrm{P}}} + 1}, \tag{2.7}$$

where $\overline{F_{\mathrm{P}}}$ denotes the averaged Purcell factor. The last approximation in equation 2.7 can be explained by γ_{bg} being comparable to the emission rate into free-space modes in the micropillar system [Gér99]. Reaching β-values close to unity is relevant when trying to achieve thresholdless lasing [Nod06] (i.e. lasing with linear input-output characteristics), which will be discussed in more detail in section 2.4. Therefore, we have to analyze equation 2.7 to find the appropriate parameters to maximize β. Looking at the first notation, suppression of leaky modes can be used to decrease γ_{bg}, which can be achieved e.g. by metallic sidewalls [Hay16].

In the following, we restrict this discussion to micropillar lasers. Here one needs to increase the Purcell factor to maximize β. It is underlined that for calculating the β-factor of a laser one has to consider all active emitters. Thus, an average Purcell factor $\overline{F_{\mathrm{P}}}$ has to be used to take into account the spectral and spatial distribution of the emitters. In order to achieve a higher $\overline{F_{\mathrm{P}}}$, one can increase the Q-factor by increasing the number of DBR mirrors. Another important parameter is the micropillar diameter. Taking into account equation 2.5, one has to decrease $V \propto d_c^2$, which is simply achieved by reducing the micropillar diameter. This approach is limited as a drop of the Q-factor occurs in the limit of small diameters [Rei11], which can be explained by side wall losses and expressed by the following equation [Riv99]:

$$\frac{1}{Q} = \frac{1}{Q_{\mathrm{planar}}} + \frac{1}{Q_{\mathrm{scattering}}}, \tag{2.8}$$

where Q_{planar} is the Q-factor of an infinitely expanded 2D planar cavity and $Q_{\mathrm{scattering}}$ is an edge scattering term that scales with the fundamental mode intensity at the micropillar edge and is inversely proportional to the microresonator diameter. Consequently, edge scattering can be reduced by increasing the micropillar diameter resulting in Q-factors close to Q_{planar}. As this would lead to increased mode volumes reducing the Purcell factor, one needs to find a trade-off between low scattering losses and small mode volumes. Here, it has to be highlighted that the scattering losses can also be reduced by tapered cavity designs such as the one presented

by Lermer et al. [Ler12]. In this approach the authors aim to match the fundamental Bloch mode with the Bragg mirror Bloch mode. Additionally, we have to take equation 2.6 into consideration. One can apply techniques to better match the emitter-cavity alignment such as the buried stressor approach, which allows the site-controlled growth of QDs with low spectral and spatial variance [Kag18, Kag19].

Moreover, it has to be considered that for $V \sim (\frac{\lambda}{n})^3$ the modes of the cavity are discrete and their frequency separation increases when the pillar diameter is reduced [Kav07]. Therefore, in order to reach high β-factors, the spectral linewidth of spontaneous emission should be smaller than the separation of higher order transverse modes. It can be shown that the circular structure of a micropillar cavity leads to transverse mode profiles that resemble the Laguerre-Gaussian mode family [Mic13]. In all following discussions we limit ourselves to the fundamental mode which exhibits a Gaussian intensity profile and a biorthogonal two-fold degeneracy [Sie86].

2.3 Photon statistics

In the regime of low light intensities where time series of, e.g., feedback-coupled microlasers cannot be recorded directly with a fast photo-diode due to responsivity constraints, an analysis of the temporal distribution of photons becomes relevant to characterize the underlying emission processes. Therefore, R. J. Glauber introduced correlation functions which give insight into photon statistic beyond the conventional theory of coherence [Gla63]. Especially, the second-order autocorrelation function provides a quantitative measure that allows for a distinction between non-classical, thermal and coherent emission processes which is possible due to a difference in the underlying photon-number distributions.

2.3.1 Coherence and correlation functions

The following theory is restricted to light with a Lorentzian frequency spectrum which is generally expected for both semiconductor lasers as well as spontaneous emission processes in the absence of inhomogeneous broadening [Oht13].

We introduce the first-order autocorrelation function $g^{(1)}$ in the representation of

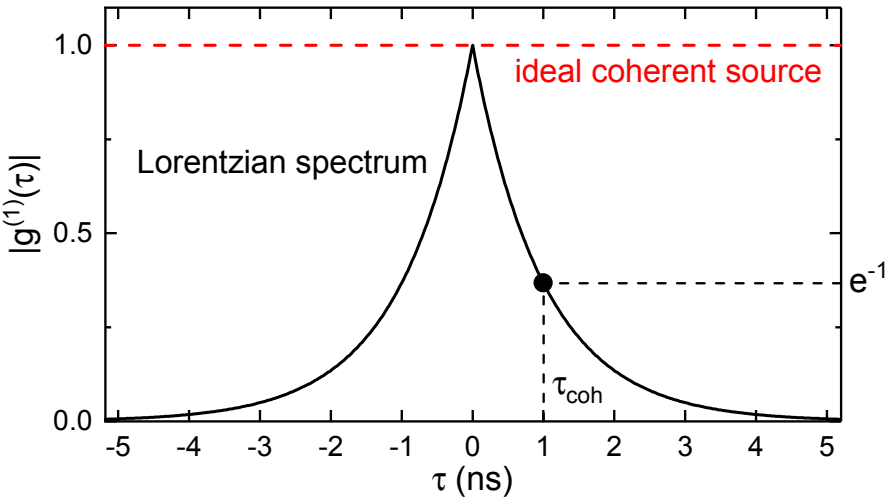

Figure 2.3: First-order autocorrelation function of light with a Lorentzian optical spectrum and an exemplary coherence time τ_{coh} of 1 ns. An ideal coherent source is depicted in comparison as a red dashed line.

the vectorial electric field $\boldsymbol{E}$ in second quantization [Lou00]:

$$g^{(1)}(\tau) = \frac{\langle \boldsymbol{E}^*(t)\boldsymbol{E}(t+\tau)\rangle}{\langle \boldsymbol{E}^*(t)\boldsymbol{E}(t)\rangle} = \frac{\left\langle \hat{a}^\dagger(t)\hat{a}(t+\tau)\right\rangle}{\langle \hat{a}^\dagger(t)\hat{a}(t)\rangle}, \tag{2.9}$$

where $\langle ...\rangle$ denotes the mean value and τ is the time delay between the correlated fields $\boldsymbol{E}(t)$ and $\boldsymbol{E}(t+\tau)$ at different times t. In second quantization this expression can be represented by the creation and annihilation operators of a photon $\hat{a}^\dagger$ and $\hat{a}$, respectively. The numerator is associated with the interference fringes that can be measured e.g. by a Michelson interferometer.

Applying the Wiener-Khintchine theorem [Khi34], one can relate the $g^{(1)}$-function of a Lorentzian spectrum through a Fourier transformation to an exponential decay of the form [Lou00]:

$$g^{(1)}(\tau) = e^{-i\omega_0\tau}e^{-|\tau|/\tau_{\mathrm{coh}}}, \tag{2.10}$$

where τ_{coh} is the coherence time which describes a time scale for the frequency stability of light. This quantity and its related coherence length l_{coh} can be calculated by [Lou00][Fox06]:

$$\tau_{\mathrm{coh}} = \frac{l_{\mathrm{coh}}}{c} = \int_{-\infty}^{\infty} \left|g^{(1)}(\tau)\right|^2 d\tau = \frac{1}{\pi\Delta\nu}. \tag{2.11}$$

Here $\Delta\nu$ denotes the linewidth of the Lorentzian function (FWHM). This clearly shows that also a precise measurement of the linewidth in the spectral domain by e.g. a Fabry-Pérot interferometer yields the same information about first-order coherence than the previously mentioned Michelson interferometer. Figure 2.3 presents the first-order autocorrelation function of an ideal coherent state that exhibits $\left|g^{(1)}(\tau)\right| = 1$ and that of a chaotic or partially coherent light state depicting an exponential decay with an exemplary coherence time $\tau_{\mathrm{coh}} = 1\,\mathrm{ns}$. It should be noted that reaching a fully coherent state is prevented by fluctuations of the light intensity that can be caused by a change in carrier density or spontaneous emission noise.

The second-order autocorrelation function is defined as follows [Lou00]:

$$g^{(2)}(\tau) = \frac{\langle \boldsymbol{E}^*(t)\boldsymbol{E}^*(t+\tau)\boldsymbol{E}(t+\tau)\boldsymbol{E}(t)\rangle^2}{\langle \boldsymbol{E}^*(t)\boldsymbol{E}(t)\rangle^2} = \frac{\left\langle \hat{a}^\dagger(t)\hat{a}^\dagger(t+\tau)\hat{a}(t+\tau)\hat{a}(t)\right\rangle}{\langle a^\dagger(t)a(t)\rangle^2}. \quad (2.12)$$

The term $\left\langle \hat{a}^\dagger\hat{a}\right\rangle$ corresponds to the average photon number $\langle n_{\mathrm{P}}\rangle$ of a light field, which represents an average intensity. Therefore, $g^{(2)}(\tau)$ is an intensity correlation, that in contrast to $g^{(1)}(\tau)$ does not contain phase information, which is a correlation of the electric field. Basically, $g^{(2)}(\tau)$ describes the normalized probability to measure a photon at the time $t \pm \tau$ if a photon is detected at time t. Here the value $\tau \to 0$ becomes of special interest as it is an indirect measure for the probability of multiple photons being emitted simultaneously. In this case equation 2.12 can be simplified to:

$$g^{(2)}(\tau = 0) = 1 + \frac{\langle \Delta n_{\mathrm{P}}\rangle^2 - \langle n_{\mathrm{P}}\rangle}{\langle n_{\mathrm{P}}\rangle^2} \quad (2.13)$$

with $\langle \Delta n_{\mathrm{P}}\rangle^2 = \langle n_{\mathrm{P}}^2\rangle - \langle n_{\mathrm{P}}\rangle^2$ denoting the variance of the photon number. This equation will be relevant in the following section as it can be used to classify the underlying photon-number distributions.

2.3.2 Thermal and coherent light

In this section we discuss the characterization of different light fields by the second-order autocorrelation function. In the description of laser physics, we can limit this analysis to spontaneous and stimulated emission which can be represented by thermal and coherent states, respectively. It has to be highlighted that these states can be described classically and therefore fulfill the Cauchy-Schwartz inequality [Tho04].

Consequently, one can show the following limits for the second-order correlation [Lou00]:

$$1 \leq g^{(2)}(\tau = 0) \leq \infty \tag{2.14}$$

$$g^{(2)}(\tau) \leq g^{(2)}(\tau = 0). \tag{2.15}$$

In contrast, non-classical light is characterized by $g^{(2)}(\tau = 0) < 1$ and can be described by Fock-states. These light states become relevant e.g. for single-photon sources and will not be further discussed in this chapter.

Coherent light

An ideal laser source emits a perfectly coherent light beam with a constant angular frequency ω_0, phase and intensity. Statistical fluctuations arise on short time-scales due to the discrete nature of photons originating from its Poissonian photon statistics [Fox06]:

$$P_{\text{coherent}} = e^{-\langle n_{\text{P}} \rangle} \frac{\langle n_{\text{P}} \rangle^{n_{\text{P}}}}{n_{\text{P}}!}. \tag{2.16}$$

For a Poissonian photon-number distribution the variance is identical to the mean photon number. This means that resulting intensity fluctuations of a laser (shot noise) are directly proportional to the emission intensity of a laser.

When inserting a light field with Poissonian distribution into equation 2.12, we simply obtain $g^{(2)}(\tau) = 1$. Basically, this implies that a coherent source exhibits photon emission events that are uncorrelated in time. Taking into account equation 2.14, this means that coherent light exhibits the minimum intensity noise possible for a classical light source. The photon-number distributions of a coherent state with $\langle n_{\text{P}} \rangle = 1$, 10 and 20 and the resulting second-order autocorrelation function are visualized in Fig. 2.4 (a) and (b), respectively. In panel (a) the increasing variance (left to right) is evident from the increasing width of the photon-number distribution.

Thermal light

Thermal and chaotic light are two examples of photon emission processes with super-Poissonian statistics [Fox06]. The former describes electromagnetic radiation from a hot body and is considered incoherent while the latter refers to a single mode of such a thermal emitter and exhibits partial coherence. In the following discussion of

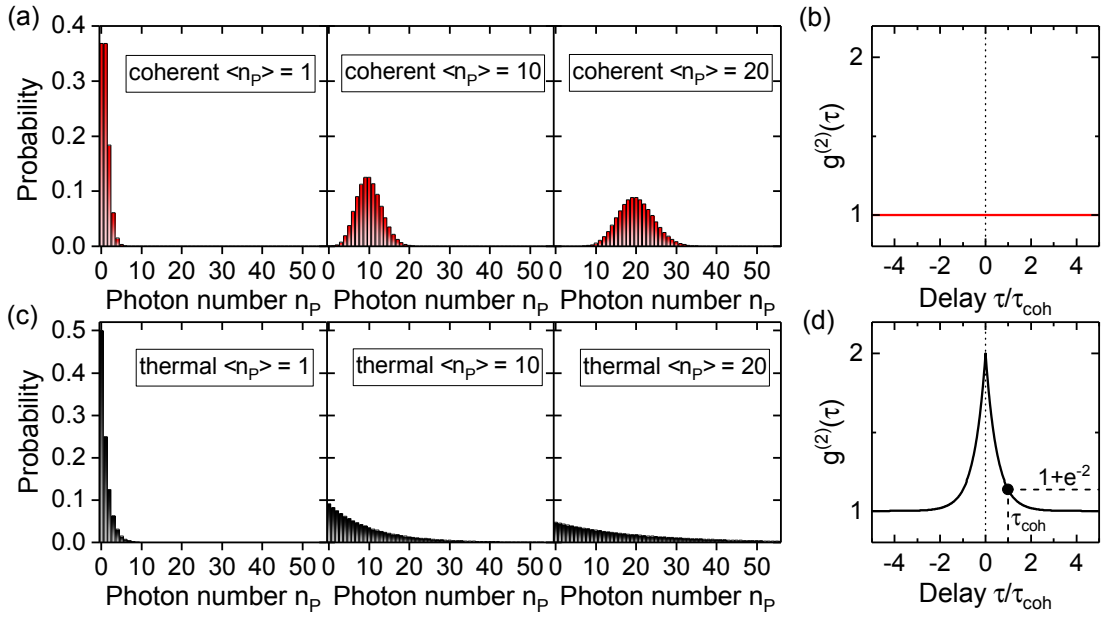

Figure 2.4: (a) Photon-number distribution of a coherent state for the average photon numbers $\langle n_\mathrm{P}\rangle = 1$, 10 and 20. Panel (b) depicts the corresponding second-order autocorrelation function. The lower panels (c) and (d) show the corresponding photon-number distribution and $g^{(2)}(\tau)$-function for a thermal state for an exemplary coherence time of 1 ns.

microcavities the contribution of only one mode is relevant and it can be shown that the photon-number probability of one mode of thermal light follows Bose-Einstein statistics that can be expressed by a geometric distribution [Fox06, Lou00]:

$$P_\mathrm{thermal} = \frac{\langle n_\mathrm{P}\rangle^{n_\mathrm{P}}}{(\langle n_\mathrm{P}\rangle + 1)^{n_\mathrm{P}+1}}, \tag{2.17}$$

which exhibits a variance of

$$\langle \Delta n_\mathrm{P}\rangle^2 = \langle n_\mathrm{P}\rangle^2 + \langle n_\mathrm{P}\rangle\,. \tag{2.18}$$

Therefore, intensity fluctuations, which are characterized by this variance, of thermal light are higher than those of coherent light. This becomes evident when considering equation 2.13. For thermal light we obtain $g^{(2)}(0) = 2$ which indicates that photons are emitted in bunches. Moreover, a relationship between first and second-order

correlation can be established by the Siegert relation [Lou00]:

$$g^{(2)}(\tau) = 1 + \left|g^{(1)}(\tau)\right|^2 = 1 + e^{-2|\tau|/\tau_{\mathrm{coh}}}. \tag{2.19}$$

Consequently, one is also able to extract the coherence time from $g^{(2)}(\tau)$ in case of single-mode thermal emission. The photon number distributions of a thermal state and the resulting second-order autocorrelation function are visualized in Fig. 2.4 (c) and (d), respectively.

Superposition of coherent and thermal light

Interestingly, in the case of bimodal lasers based on microcavities we can find both coherent and thermal light simultaneously. The latter becomes more relevant with increasing β-factor. Here we want to discuss the linear superposition of coherent and thermal light. This is a good approximation for the switching dynamics that we will investigate later in this thesis, where the emission into one mode abruptly changes from a thermal to a coherent state. We define the photon-number distribution of the superposition P_{sup} as follows:

$$P_{\mathrm{sup}} = r_{\mathrm{thermal}} \cdot P_{\mathrm{thermal}} + (1 - r_{\mathrm{thermal}}) \cdot P_{\mathrm{coherent}}, \tag{2.20}$$

where r_{thermal} denotes the ratio of the thermal distribution contributing to the total photon-number distribution. As can be easily seen from equation 2.13, if both P_{thermal} and P_{coherent} exhibit identical average photon numbers in this superposition (which is possible close to lasing threshold), one obtains $g^{(2)}(0) = 1 + r_{\mathrm{thermal}}$.

Above lasing threshold, micropillar lasers can exhibit switching dynamics. This means that statistical switching events occur between bistable configurations in which one mode is in a coherent state while the counterpart mode is in a thermal state and vice versa. Interestingly, the dynamics are triggered by spontaneous emission noise resulting in a simultaneous switching process of each mode into the opposite state. Here we find a different scenario that is depicted in Fig. 2.5. The superposition is characterized by thermal emission with a low mean photon number and a coherent state with a high one. Panel (a) visualizes the corresponding photon-number distributions, while (b) depicts the resulting value of $g^{(2)}(0)$ for a superposition of 5 thermal and 15 coherent photons on average. One clearly ob-

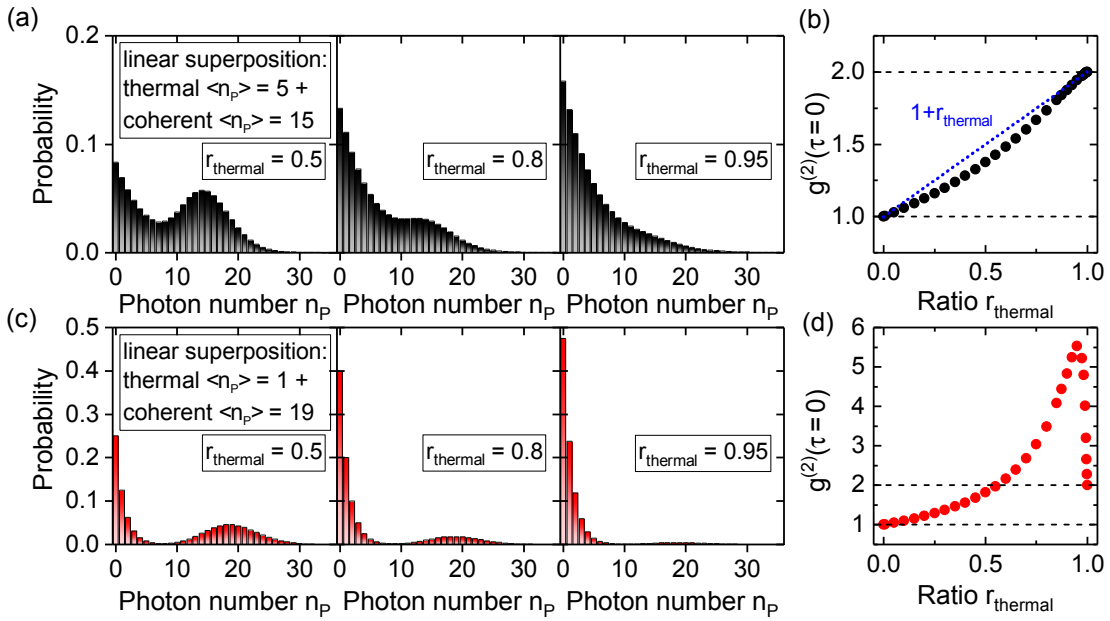

Figure 2.5: (a) Photon-number distributions of a superposition state with the average photon numbers $\langle n_\mathrm{P}\rangle = 5$ for thermal light and $\langle n_\mathrm{P}\rangle = 15$ for coherent light. The distributions are shown for a ratio of thermal emission $r_\mathrm{thermal} = 0.5$, 0.8 and 0.95. Panel (b) depicts the corresponding value of $g^{(2)}(0)$ for various values of r_thermal. As a comparison the case of P_thermal and P_coherent exhibiting identical $\langle n_\mathrm{P}\rangle$ is shown as a blue dotted line. The lower panels (c) and (d) illustrate the corresponding photon-number distributions and values of $g^{(2)}(0)$ for the average photon numbers $\langle n_\mathrm{P}\rangle = 1$ (thermal) and $\langle n_\mathrm{P}\rangle = 19$ (coherent), respectively. Dashed lines in panels (b) and (d) indicate the cases of coherent emission ($g^{(2)}(0) = 1$) and thermal emission ($g^{(2)}(0) = 2$).

serves a deviation from a linear increase (blue dotted line) of $g^{(2)}(0)$ from 1 to 2. This scenario becomes even more evident when choosing a superposition of 1 and 19 photons (see panel (c) and (d), respectively). In the range of $0.6 \leq r_\mathrm{thermal} < 1$ we find values of $g^{(2)}(0) > 2$, a situation which is termed *super-thermal bunching*. This photon bunching phenomenon can be understood as thermal emission that is accompanied by coherent multi-photon pulses and will be discussed in detail in chapter 4.

2.4 High-β lasing

Macroscopic semiconductor lasers with mode volumes $V \gg \lambda^3$ exhibit β-factors on the order of 10^{-6} to 10^{-4}, so that spontaneous emission is essentially a loss term.

Consequently, spontaneous emission into the lasing mode can effectively be disregarded. The small β-values can be explained by the isotropic radiation pattern of spontaneous emission, which causes predominant coupling of SE to continuum modes. Moreover, the broad spectral linewidth of SE leads to a preferential coupling of the emission to non-lasing modes [Yam91]. In this classical regime, the lasing threshold can simply be defined by the pump current at which the photon loss rate of the cavity κ is equal to the net gain by stimulated emission [Yam91]. This definition becomes less accurate and needs to be revisited when β approaches unity in case of nano- and microlasers.

As previously mentioned, significant research was conducted to reduce the size of semiconductor lasers. Apart of the great fundamental interest in high-β micro- and nanolasers, the main application-oriented goals since the beginning were a compact size of the devices as well as low power consumption [Ma19]. Additionally, miniaturized lasers have fewer optical modes available which leads to increased β-factors as well as higher modulation bandwidths. Besides micropillar lasers, which are the focus of this thesis, significant effort was put into producing high-β nanolasers since the early 1990s. Among others, microdisk lasers [McC92], photonic crystal lasers [Pai99] as well as nanowire and nanobeam lasers [Joh01, Jag18] can be highlighted in this context. In order to achieve β-factors close to unity, the concept of plasmonics is used for extreme light concentration and manipulation at the nanoscale [Sch10]. This can be realized e.g. by a coaxial nanolaser. Here a coaxial waveguide that supports plasmonic modes in the center of the cavity is surrounded by a metal-coated semiconductor ring [Kha12].

To highlight the difference in the input-output characteristics of semiconductor lasers between the low and high-β regime, we assume a simplistic rate equation model that includes the rate of spontaneous emission into the lasing mode. Taking the model presented in Ref. [Yam91, Bjö91], we can write the pump current I as a function of the photon number n_P:

$$I(n_\mathrm{P}) = \frac{eE_\mathrm{res}}{\beta Q\hbar}\left[\frac{n_\mathrm{P}}{n_\mathrm{P}+1}(1+\xi)\left(1+\beta n_\mathrm{P}+\frac{\tau_\mathrm{sp}}{\tau_\mathrm{nr}}\right)-\xi\beta n_\mathrm{P}\right] \tag{2.21}$$

$$\text{with}\quad \xi = \frac{\beta N_0 V Q\hbar}{E_\mathrm{res}\tau_\mathrm{sp}}. \tag{2.22}$$

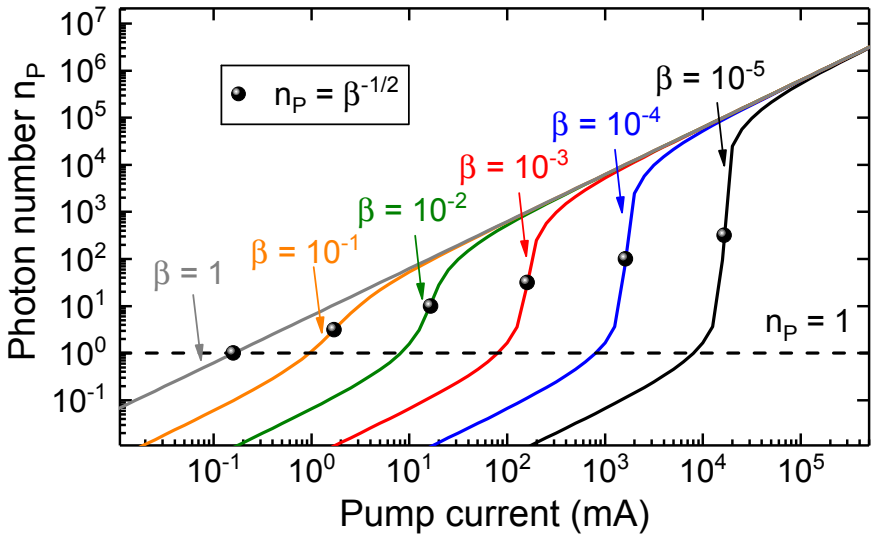

Figure 2.6: Input-output characteristics of semiconductor lasers with different β-factors. The intracavity photon number n_P is plotted as a function of the pump current I. Two commonly used definitions of the lasing threshold are shown, namely $n_P = 1$ ([Bjö94], indicated by a dashed line) and $n_P = \beta^{-1/2}$ ([Ric94, Moo18], indicated by bullets). Interestingly, they coincide in the limit $\beta \to 1$. One can observe a clear reduction of the lasing threshold with increasing β-factor. Parameters of this simulation taken from [Bjö91]: $\frac{Eres}{Q\hbar} = 10^{12}\,\mathrm{s}^{-1}$, $\tau_{sp} = 1\,\mathrm{ns}$, $N_0 = 10^{18}\mathrm{cm}^{-3}$, $V = 10^{-15}\,\mathrm{cm}^3$ and $\tau_{nr} \gg \tau_{sp}$.

Here e is the elementary charge and τ_{nr} denotes the lifetime of non-radiative emission processes. Additionally, the dimensionless parameter ξ is introduced which describes the photon number in the lasing mode when the free carrier density becomes equal to the one at transparency N_0.

Figure 2.6 depicts the resulting input-output characteristics for different β-factors in double-logarithmic scale. For low β-factors one can observe a typical "s-shape". At low injection the photon number increases linearly until the lasing threshold is reached. In this regime all photons in the cavity mode originate from spontaneous emission. At the threshold current I_{th} the photon number increases super-linearly and an onset of stimulated emission is found. A further increase of the pump current again leads to a linear increase of the photon number because of gain saturation. By increasing the β-factor the threshold current I_{th} is reduced and the regime of super-linear increase is washed out. For $\beta = 1$ the input-output curve becomes linear and is therefore identical to that of an LED. This limiting case is termed *thresholdless lasing*. It is important to note that a transition towards coherent emission still exists,

but it cannot be determined by the input-output characteristics. Consequently, the second-order autocorrelation function becomes an essential tool for distinguishing between a laser and a thermal emitter in the high-β regime.

One needs to find a new definition of the laser threshold that also holds in the high-β regime as SE, which is not taken into account in the classical definition, reduces the threshold when coupling into the lasing mode. Here Björk et al. proposed $n_{\mathrm{th}} = 1$ which is consistent with the super-linear increase of n_{P} [Bjö94]. This definition becomes problematic for values of $\beta < 1$. Even though there is a super-linear increase of n_{P}, we still find a coexistence of spontaneous and stimulated emission and $g^{(2)}(\tau) > 1$ above lasing threshold in this definition [Loh18]. For this reason, we choose the definition $n_{\mathrm{th}} = \beta^{-1/2}$ in the following [Ric94, Moo18]. This takes into account that emission above lasing threshold is coherent exhibiting $g^{(2)}(\tau) \simeq 1$, which is expected as the lasing threshold is in the inflection point of the s-shaped input-output characteristics as shown in Fig. 2.6. Additionally, it should be noted that in the limit of $\beta = 1$ the two threshold definitions become identical.

2.5 Optical feedback

Semiconductor lasers provide an interesting platform for investigating nonlinear dynamics when subject to delayed optical feedback. Here a multitude of phenomena from low frequency fluctuations [Tar95b] and coherence collapse [San94] to regular pulse packages [Hei01] have been found. The reason behind the sensitivity to external perturbations can be found in their intrinsic dynamical timescales. Single-mode semiconductor lasers are often classified as class B lasers [Tre85]. This means that their dynamics can be described by a two-dimensional rate equation model of the complex optical field in the cavity and the carrier density in the active medium as the polarization decays so fast that it can be adiabatically eliminated [Kel12]. Therefore, a semiconductor laser can be viewed as a driven damped nonlinear oscillator which is approaching a steady-state [Sci15]. This results in relaxation oscillations that will be discussed in more detail in section 5.4. Theoretically, optical feedback effects in semiconductors are often described by the Lang-Kobayashi (LK) rate equations

[Lan80]:

$$\frac{d}{dt}E(t)e^{i\omega t} = \left[i\omega_N(n) + \frac{1}{2}\left(G(n) - \kappa\right)\right] E(t)e^{i\omega}t + KE(t-\tau)e^{i\omega(t-\tau)} \tag{2.23}$$

$$\frac{d}{dt}n = -\frac{n}{\tau_{\mathrm{sp}}} - G(n)\left|E\right|^2 + \frac{J}{ed}, \tag{2.24}$$

where E is the electric field inside the cavity, ω is the oscillation frequency of the laser, ω_N is the resonance frequency of the laser, $G(n)$ is the gain, κ is the cavity loss rate, n is the carrier density, τ_{FB} is the round-trip time of the external cavity, K is the feedback coefficient describing the coupling to the cavity and P is the number injection rate per unit volume of the excited carriers.

These equations are able to describe most dominant effects that are observed in classical semiconductor lasers in the limit of low feedback strength and single-longitudinal mode emission [Tar95a]. Sensitivity of semiconductor lasers to optical perturbations from feedback (as well as injection locking) can also occur when their emission frequency is detuned from the gain maximum [Sci15]. This can be explained by the coupling of the refractive index and the gain, which results in the linewidth enhancement factor α that will be discussed in more detail in section 6.1. This sensitivity has significant influence on the stability of the modes that are constituted by the external cavity [Lüd11].

It is underlined that the feedback coefficient K (which is related to the reflectivity of the external cavity mirror) is relevant to determine the temporal dynamics of a laser. The instabilities of single-mode semiconductor lasers have been studied in detail and have led to a distinction of five feedback regimes ordered by ascending feedback strength [Tka86]:

- Regime I: Narrowing or broadening of the emission line is found.
- Regime II: External cavity modes gives rise to mode hopping among solitary and external modes. Furthermore, this regime depends on τ_{FB} and in the case of coherent feedback phase sensitivity is found.
- Regime III: Mode hopping is suppressed, and the laser operates at a single narrow line.
- Regime IV: Satellite modes appear and rise in intensity with increasing K. The

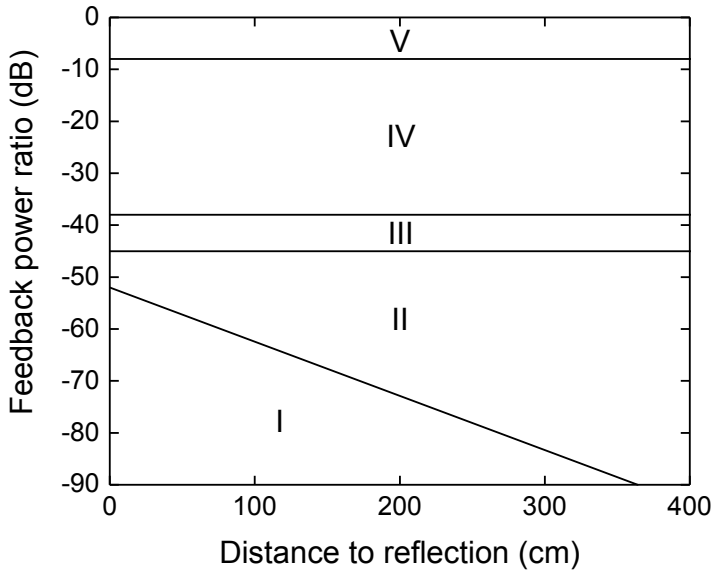

Figure 2.7: Visualization of the different feedback regimes (numbered I to V). The feedback power ratios are plotted as a function of the distance to the reflection. (Adaptation of [Tka86])

laser line broadens significantly which is equal to a reduction of the coherence time of the laser. Thus, this regime is termed *coherence collapse*.

- Regime V: Both the internal and external cavities act like one single cavity [Oht13]. Stable lasing emission with a narrow linewidth is found.

While these observations were originally made for a 1.5 µm distributed feedback laser and are visualized in Fig. 2.7, the dynamics of other single-mode semiconductor lasers exhibit similar results for the variations of K (as well as the external cavity length in case of regimes I and II) [Oht13].

When investigating microlasers, the previously discussed set of LK equations has to be adapted. Firstly, LK does not include any parameters of the emitter. In case of QDs the scattering of carriers from the wetting layer into the dot has to be taken into account to accurately describe the temporal dynamics [Red16]. Moreover, the optical modes are treated independently in the LK model. Gain competition in QD microlasers requires coupled rate equations that also include interaction between two modes. Finally, spontaneous emission in the LK model is only a loss channel for carriers ($-\frac{n}{\tau_s}$). With increasing β-factor spontaneous emission also has to be

taken into account for the equation of the electric field. The fully extended semi-classical rate equations for modeling QD micropillar lasers that was implemented by Christoph Redlich, Benjamin Lingnau and Kathy Lüdge can be found in A.1.

3 Experimental techniques

This chapter highlights the technology and experimental techniques applied in this work. Firstly, the sample fabrication and processing of an electrically contacted QD micropillar laser is sketched. Then micro-electroluminescence spectroscopy and correlation spectroscopy are explained in detail with their respective experimental configurations. Finally, a method for the direct measurement of the photon-number distribution with a transition-edge sensor (TES) is presented.

3.1 Sample fabrication

Figure 3.1 (a) depicts an artistic image of the investigated microlasers that resembles miniaturized VCSELs. In order to fabricate the column-shaped vertically emitting Fabry-Pérot laser with electrical contacts, several nanotechnological steps have to be performed. Fabrication of the samples starts by molecular beam epitaxy which ensures high quality layers with defined material composition and thickness [Cho75]. It has to be noted that the whole sample fabrication and processing was carried out at the Chair of Technische Physik at the University of Würzburg.

Firstly, a bottom DBR mirror is grown which consists of 27 alternating $\frac{\lambda}{4}$-thick layers of GaAs and AlAs. These semiconductor compounds are well suited for the realization of high quality heterostructures as they have similar lattice constants for lattice matched growth but different refractive indices. The lower DBR is followed by a one-λ thick intrinsic GaAs cavity which includes a single layer of laterally extended $In_{0.3}Ga_{0.7}As$ QDs with an area density of $5 \cdot 10^9/cm^2$ in its center. The QDs are formed in a self-organized manner in the shape of truncated lenses with a wetting layer in the used Stranski-Krastanow growth mode [Str38]. The self-organized formation of QDs can be explained by the lattice mismatch between the QD material (InGaAs) and the GaAs matrix. Two-dimensional layered growth is only energetically favored until a critical thickness of a few monolayers is reached.

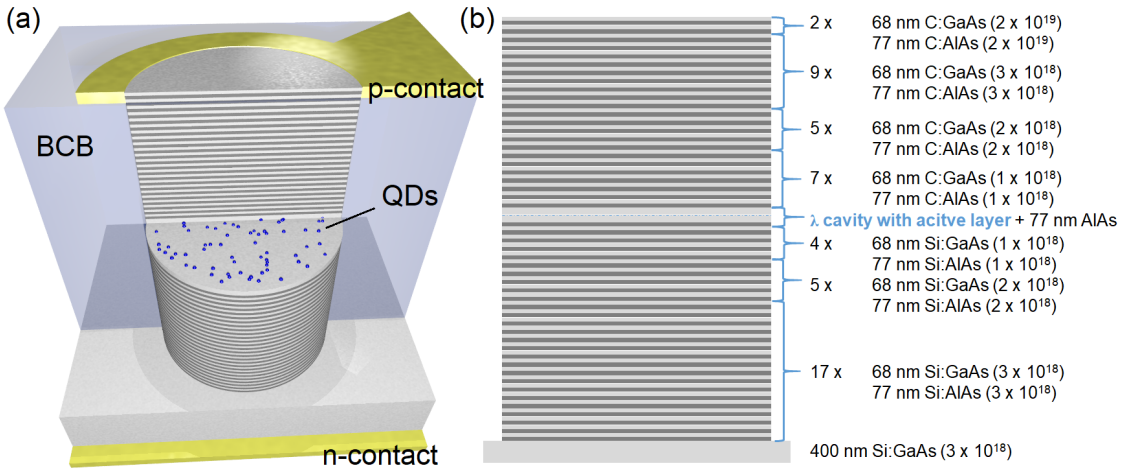

Figure 3.1: (a) Schematic image depicting the sample design of the investigated electrically contacted micropillar lasers. The one-λ thick intrinsic cavity is sandwiched between a lower and upper DBR with 27 and 23 mirror pairs, respectively. The active layer is constituted by a single layer of $Ga_{0.70}In_{0.30}As$ QDs. The top gold contact lies on the dielectric benzocyclobuthene (BCB). (b) Exact layer structure as described in [Löf08]. A δ-doping of $10^{12}\,cm^{-2}$ is added at each interface between GaAs and AlAs.

Subsequently, the formation of three-dimensional islands sets in releasing the built up strain to form the QDs. Finally, the top DBR with 23 alternating layers of GaAs and AlAs is grown. Applying equation 2.2 and the values of the refractive index $n_{GaAs} \simeq 3.5$ and $n_{AlAs} \simeq 2.9$ [Ada85], one can calculate the mirror reflectivities $R_{\text{bottom DBR}} = 99.98\,\%$ and $R_{\text{top DBR}} = 99.94\,\%$. This value is an upper limit as the equation does not include absorption in the DBR. In practice the used microcavity design leads to quality factors of about 20000 in doped structures, which will be determined more precisely from the linewidth at inversion (using equation 2.3) in the following chapters. Here transparency is chosen to correctly determine the Q-factor of the cold cavity by setting the pump current so that all QD transitions are saturated [Gay08]. Care has to be taken that the lasing threshold is not reached in this analysis as the linewidth of the fundamental mode is reduced by the increased coherence in the lasing regime [Sch58].

Figure 3.1 (b) depicts the layer structure of the device. Additionally, a δ-doping of $10^{12}\,cm^{-2}$ is added at each interface between GaAs and AlAs to reduce the electrical resistance of the DBRs [Löf08] (which is not shown in the figure). In order to realize electrically pumped devices, the semiconductor materials of the DBRs have to be doped. Here p-doping is achieved with Carbon impurities, while n-doping accom-

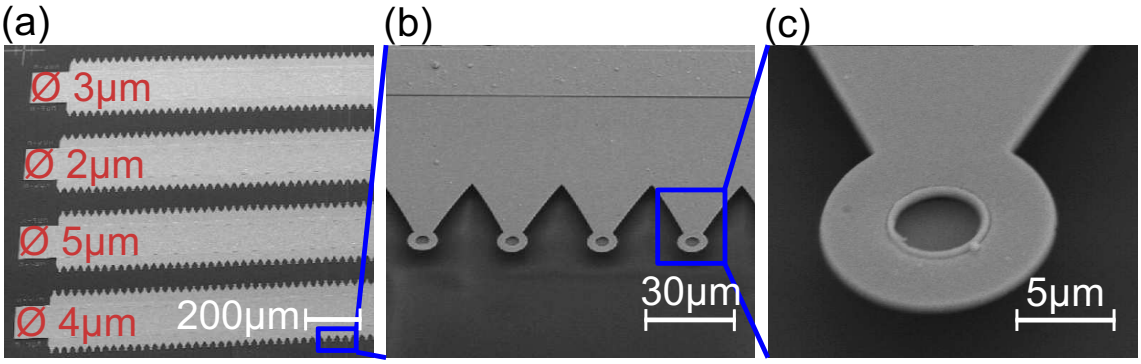

Figure 3.2: Scanning electron microscope image of the structure described in Fig. 3.1 (taken with an acceleration voltage of 25 kV). (a) Overview of one sample piece. The microlaser diameter is indicated in red. Precise cleaving between contact bars enables side access of the microlasers, some of which are marked by a blue box (zoom region of successive panels). (b) and (c) depict close up images of the lasers with their contact bar and ring contact for current injection as well as one microlaser of 4 µm diameter. (SEM images provided by Monika Emmerling from Universität Würzburg.)

plished by Silicon [Sch11]. The doping profile illustrated in Fig. 3.1 (b) is optimized so that free carrier absorption of the confined modes in the mirrors becomes minimal while current injection is still efficient [Böc08]. It is underlined that the sample design is identical for all microlasers investigated in this dissertation. Only in case of microlaser B (see chapter 4) the mirror thickness was altered to 66 nm AlAs and 79 nm GaAs and the λ-cavity has a thickness of 264 nm instead of 276 nm leading to a resonance wavelength of 850 nm.

The column-shaped pillar structures with diameters ranging from 2 to 5 µm are fabricated using high-resolution electron-beam lithography and plasma etching (electron cyclotron resonance reactive ion etching, ECR-RIE [Bac05]). Subsequently, the sample is planarized using benzocyclobuthene (BCB) and a ring-shaped gold contact is formed by a second electron beam lithography and metal deposition step. In order to pump multiple microlasers (here up to 120) simultaneously, these contacts converge in one common Au contact bar as illustrated in Fig. 3.2. This contact configuration has important practical reasons: The devices exhibit lasing at temperatures below $\sim$100 K and can therefore only be investigated in an cryostat with four electrical feed-throughs. As the yield of suitable devices is about 30 %, bonding of each micropillar and the investigation of only four micropillars for each cool-down cycle is impractical. One has to note that the microlasers have a distance of 30 µm and are emitting simultaneously. Thus, spatial filtering via a pinhole configuration

has to be applied in the detection path.

In order to obtain additionally lateral access to one row of microlasers, the sample is cleaved parallel to the gold bars in close proximity to the row of micropillars. Each sample piece includes four bars of microlasers which have a diameter of 2, 3, 4 and 5 µm, respectively. By permuting the diameter sequence, we enable the availability of each pillar diameter for lateral access.

3.2 Micro-electroluminescence and time-resolved spectroscopy

The experimental setup used to perform micro-electroluminescence (µEL) spectroscopy is depicted in Fig. 3.3. The sample is mounted in a Helium-flow cryostat (model: *Janis ST-500*). The temperature is precisely controlled with a heater element and stabilized usually at a temperature of $T = 32.00\,\mathrm{K}$ with 0.01 K precision. This temperature is chosen for optimal spectral overlap of the fundamental cavity mode with the gain maximum of the QDs, yielding the highest optical output powers while still preserving narrow linewidths. In general, lasing is found up to $\sim 100\,\mathrm{K}$ for microlaser devices with a gain medium based on InGaAs QDs [Rei08]. For thermal isolation the pressure in the sample chamber is reduced with a turbomolecular pump to $\sim 10^{-7}$ mbar. By mounting the cryostat on two orthogonal linear stages equipped with servo drive motors, one is able to select and collect the emission of one specific microlaser with an aspheric lens (numerical aperture $NA = 0.5$). Electrical pumping is realized by an *Agilent B2900* voltage source and measurement unit. Here, the microlaser bars are biased with a voltage (and not with current as typically done for individually contacted VCSELs). This approach is chosen to keep the current flow through a micropillar independent of the one through the others on the same bar.

In µEL the aspheric lens with NA = 0.5 (or an infinity corrected microscope objective with NA = 0.4 and magnification of 20) collimates the light collected from its focal spot with a nominal diameter of $\sim 1\,\mu\mathrm{m}$, which is the position where the microlaser under study has to be placed. For feedback experiments we prefer aspheric lenses with a transmission T close to 90 % over microscope objectives as the latter comprise multiple stacked lenses, which leads to lower transmission ($T \sim 75\,\%$), effectively decreasing the maximum feedback strength. By focusing the collimated emission with the achromatic lens (focal length $f = 20\,\mathrm{cm}$) on a pinhole with 50 µm diameter, one can ensure that only light from the focal point but not from neighbor-

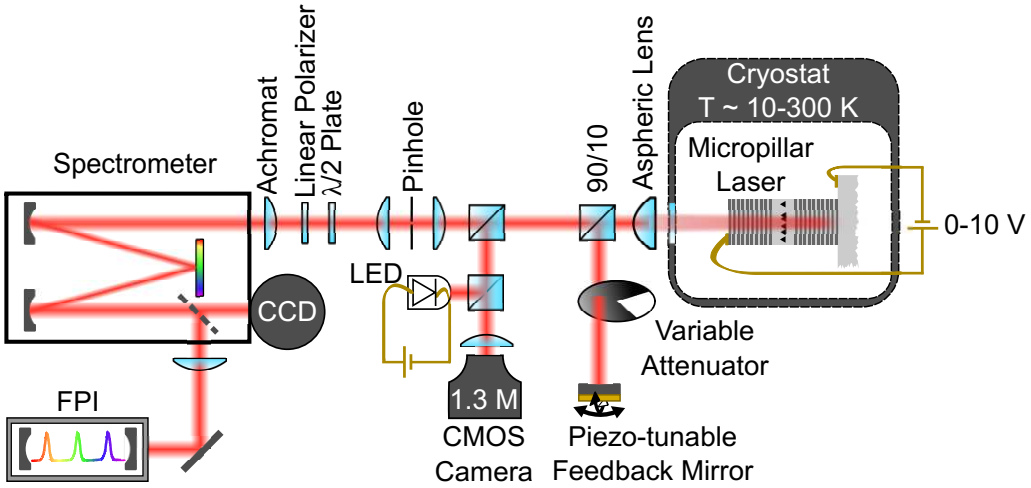

Figure 3.3: Illustration of the experimental setup. The QD-micropillar laser is mounted inside a He-flow cryostat and stabilized usually at a temperature of $T = 32.00 \pm 0.01$ K. The feedback cavity is constructed by a 90:10 beamsplitter cube and a piezo-tunable mirror. The spectral properties are measured with a charge-coupled device (CCD) camera after spatially filtering the emission of one microlaser with a pinhole and spectral decomposition with a monochromator. The selection of one polarization basis is achieved by the combination of a half-wave plate and a linear polarizer. High-resolution spectra are recorded with a Fabry-Pérot interferometer (FPI). By illuminating the sample with an LED, we can detect a microscopic image of the microlasers with a CMOS camera.

ing microlasers 30 µm away is detected by the spectrometer. Polarization resolved measurements are realized by a combination of a half-wave plate and a linear polarizer. The former is rotating the polarization basis of the microlaser in detection so that two orthogonal orientations are found in each of which only one mode can pass the linear polarizer. As grating monochromators exhibit a preferred polarization angle, we rotate the half-wave plate while keeping the linear polarizer in fixed orientation to analyze the polarization dependence of the microlaser emission. Finally, the microlaser emission is focused on the entrance slit (typically 30 µm slit-width) of a monochromator (*Princeton Instruments Acton SP-2750*) and collimated on a reflective grating (1500 grooves per mm) spectrally decomposing the emission. Subsequently, optical spectra are recorded with a Peltier-cooled charge-coupled device camera (CCD, *Princeton Instruments Pixis 400*, 1340 x 400 pixels, spectral resolution: 6.5 GHz) attached to the exit slit of the monochromator, while high-resolution spectra can be taken with a home-made scanning Fabry-Pérot interferometer (FPI, 7.5 GHz free spectral range, 100 MHz resolution), that is set up at the free space

exit port. This configuration allows for a continuous transition between the CCD and the FPI when measuring the linewidth of microlasers as the free spectral range of the FPI (which is fixed as a confocal design is used) is higher than the spectral resolution of the spectrometer.

The external feedback cavity is constituted by a 90:10 beamsplitter cube and a dielectric mirror mounted on a tilting piezo platform (*Physik Instrumente S-330.2SL*, closed loop tilt of 2 mrad). Moreover, one can precisely control the feedback strength with a neutral density filter wheel by two orders of magnitude. For visualization of the sample surface we implement a near-infrared LED in our optical path. Both the light reflected from the surface as well as emission from the laser are detected by a 1.3 Megapixel CMOS camera within a microscopic image. Moreover, this home-built microscope also allows tracking of the feedback spot on the sample. The alignment procedure of the external cavity is explained in more detail in section 4.1.

Figure 3.4 illustrates the modified setup that is used for temporally resolved measurements with a *Hamamatsu* universal streak camera. This device allows us to measure low intensity light events with high temporal resolution below 2 ps. As the streak camera is equipped with a compact grating spectrometer (*Princeton Instruments Acton SP-2150i*, 50 grooves per mm grating) the wavelength information is preserved. In the following, the working principle of the streak camera is sketched [Ham08]. The incident light hits a photocathode which converts the light into electrons. These are accelerated by electrodes towards a micro-channel plate and phosphor screen. The temporal resolution is achieved by additionally passing a pair of sweep electrodes which apply an electric field perpendicular to this direction.

In the so called *synchroscan mode* a sinusoidal oscillator is synchronized to the 80 MHz pulse repetition rate of a *Spectra-Physics Tsunami* titanium-sapphire laser (Ti:Sa) and the linear part of its voltage is applied to the sweep electrodes. This is realized by detecting part of the Ti:Sa emission with a photodiode with a response time of ~ 300 ps synchronized to streak camera. Therefore, we implement another 90:10 beamsplitter in the excitation path. Consequently, the recorded time-traces have a constant temporal offset with respect to the Ti:Sa pulse impinging on the microlaser which can be adjusted by a delay unit. By synchronizing the repeated sweep frequencies, one can overlay several ten thousands of such traces and extract the periodic temporal response of a microlaser to the Ti:Sa pulse giving insight in both the relaxation oscillation frequency and its damping. The practical imple-

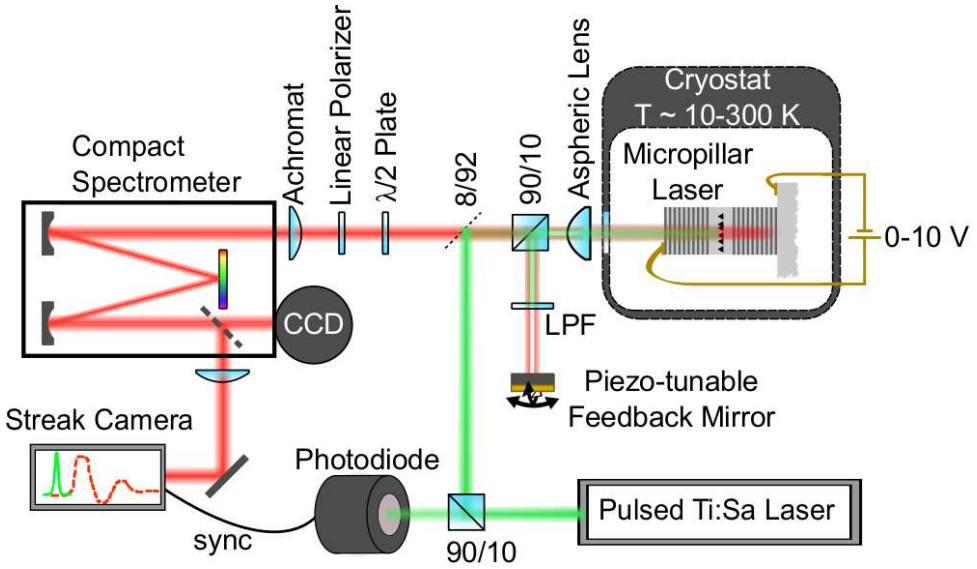

Figure 3.4: Experimental setup for streak camera measurements. A frequency-tunable titan-sapphire (Ti:Sa) laser is coupled onto the microlaser facet. A long pass filter (LPF) is inserted into the external cavity to suppress feedback of the Ti:Sa pulse. In order to get both spectral and temporal information of the microlaser emission a compact spectrometer is attached to the Streak camera, which is synchronized to the Ti:Sa pulses.

mentation will be described in more detail in section 5.4. Additionally, for feedback experiments we implement a long-pass filter (LPF) in the external cavity to suppress the round-trip of Ti:Sa pulses in the external cavity.

Moreover, the *single-sweep mode* can be used to retrieve a time-series of the output signal of a microlaser for non-periodic signals. Here we take only one single shot by applying a ramp voltage to the sweep electrodes. This way we are able to record single time-series with a length of up to 2 ms (for these long time series the spectral resolution is reduced as the streak camera has 508 time bins). By adding a Wollaston prism in front of the entrance slit of the spectrometer, we are able to spatially separate and simultaneously measure both orthogonally polarized modes of a microlaser, which will be described in more detail in section 4.2. In the single-sweep mode it is crucial to have sufficient light intensities to obtain time-series with a good signal-to-noise ratio as the quantum efficiency η_{streak} is low in the NIR regime. Therefore, these experiments are done with a microlaser with an emission wavelength of 850 nm where the streak camera exhibits $\eta_{\text{streak}} = 0.73\,\%$. As a comparison, for a wavelength of 900 nm one finds $\eta_{\text{streak}} = 0.055\,\%$ with η_{streak}

decreasing further for higher wavelengths [Ham18].

3.3 Correlation spectroscopy

Using μEL spectroscopy as introduced in the previous section one is not able to measure the statistical or dynamical properties of the investigated emission. This is evident as optical spectra need a finite integration time (usually $>1\,\mathrm{ms}$) to exhibit an acceptable signal to noise ratio. Thus, as already explained in section 2.3.1 correlation functions provide a powerful tool to get insight into the emission dynamics of microlasers at ultra-low light levels $\ll 1\,\mu\mathrm{W}$. The following section describes the experimental realization of the second-order autocorrelation function as well as the crosscorrelation of two distinct optical signals.

For correlation spectroscopy the emission that is spectrally decomposed by the grating in the spectrometer is focused on the exit slit of the monochromator, collimated by an achromatic lens and coupled to a multi-mode fiber with a core diameter of $50\,\mu\mathrm{m}$. Thus, the exit slit of the monochromator acts as a spectral filter. Here we use a 300 grooves per mm grating and an exit slit width of $150\,\mu\mathrm{m}$ which results in a spectral window of $\Delta\lambda = 0.65\,\mathrm{nm}$ ($\Delta E = 0.99\,\mu\mathrm{eV}$) around the central wavelength of the first order diffracted beam of the grating. It is crucial that this filtering may not be smaller than the linewidth of the investigated mode. Otherwise, the Poissonian emission of a laser is changed into chaotically fluctuating light [CN92] as phase fluctuations become intensity fluctuations in this regime which artificially changes the measured photon statistics. The spectrally selected emission is then detected by a fiber coupled single-photon counting module (SPCM) which is based on a Silicon avalanche photo diode (APD). In the experiment we use *IDQuantique id100* SPCMs with $40\,\mathrm{ps}$ temporal resolution and a quantum efficiency of $\sim 3\,\%$ at $900\,\mathrm{nm}$.

Figure 3.5 illustrates a comparison of the two experimental configurations for correlation measurements. Panel (a) highlights the classical Hanbury Brown and Twiss (HBT) setup [HB56] that is used to determine the second-order autocorrelation function of the emitted intensity. Here, the linearly polarized emission of one mode is coupled into a fiber beamsplitter with a 50:50 splitting ratio and one SPCM at the end of each fiber. To avoid crosstalk between SPCMs caused by afterpulsing of the APDs [Ulu00] each optical fiber after the beamsplitter has a length of $25\,\mathrm{m}$. Consequently, artifacts caused by this afterpulsing occur outside of the analyzed

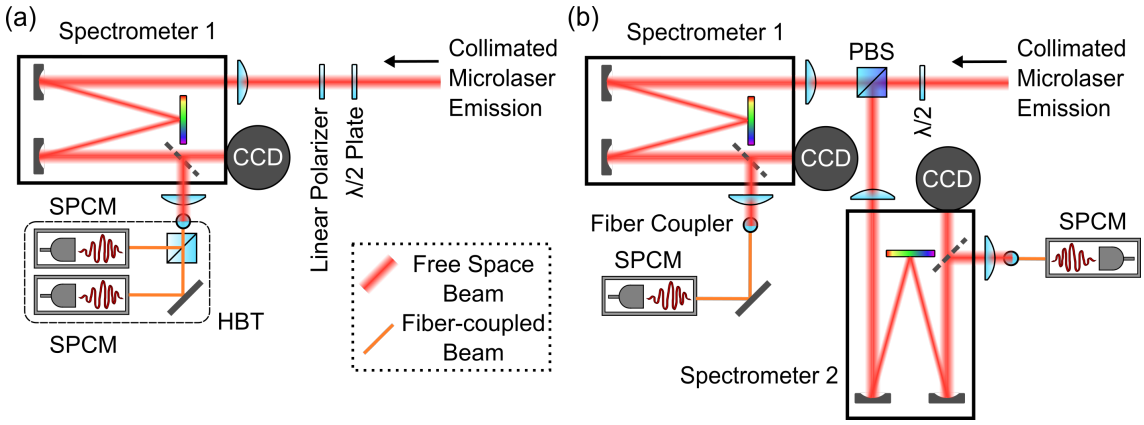

Figure 3.5: Comparison of the setup used for (a) autocorrelation and (b) crosscorrelation measurements. The former is the classical HBT configuration, while the latter require the two orthogonally polarized modes to be split to two separate spectrometers with attached single photon counting modules (SPCMs). The separation is achieved by replacing the linear polarizer with a polarizing beamsplitter (PBS).

time window at $\tau = \pm 245\,\text{ns}$. The electrical response (TTL signal) of the SPCMs is read out by a *qTools qTau* time-to-digital converter. This device has the advantage of having an internal delay unit so that no temporal delay of one signal is needed. Moreover, by time-tagging of the photon events and correlating them in a $10\,\mu\text{s}$ window the counting electronics directly yields the $g^{(2)}$-function. Thus, a renormalization as in histogramming over different time delays (see e.g. [Mic00, Yua02]) is not needed. It is underlined that the second-order autocorrelation cannot be retrieved by using only one single SPCM which is explained by their finite dead time of 45 ns being greater than the coherence time of up to a few ns of the investigated microlasers [Ste12].

Panel (b) depicts the setup used for crosscorrelation measurements which is based on the same concept as the HBT configuration. Here two orthogonally polarized signals are separated by a polarizing beamsplitter and directed to two remote spectrometers with one fiber-coupled SPCM behind each exit slit. By measuring the correlation of the two spectrally separable signals with the same counting electronics as above we get further insight on the interplay between the two modes of a microlaser competing for the common QD gain.

3.4 Direct measurement of the photon-number distribution

A transition-edge sensor (TES) provides the possibility of directly measuring the photon-number distribution (PND) of the investigated microlasers. With detection efficiencies close to unity in the near infrared regime [Lit08] it allows for a resolution down to single photons [Lit10, LL13]. Moreover, measuring the PND yields complementary information to the second-order autocorrelation function when analyzing for instance superposition states such as the ones described in Fig. 2.5.

The TES detector operates as a highly sensitive calorimeter. Figure 3.6 (a) depicts the electrical circuit of the device. Applying a voltage-bias, one is able to address an operation point in the phase transition region between superconducting and normal phase with finite ohmic resistance R_{N}, which is in the case of the used tungsten based system close to the critical temperature of $\sim 150\,\mathrm{mK}$. The resulting resistance curve is illustrated in panel (b). When a photon hits the detector, the induced temperature increase leads to a change of the current I_{TES} which is measured by an inductively coupled two-stage DC-superconducting quantum interference device (SQUID) [Dru07]. By measuring V_{out} the SQUID acts as a highly sensitive current sensor as I_{TES} is proportional to V_{out}. Lastly, panel (c) shows the SQUID voltage of a single photon detection event. After the absorption of a photon on the TES, the system is configured such that it relaxes back to its working point which is called negative electro-thermal feedback [Irw05]. Here a thermal recovery time of the detector and the coupled electronics after photon detection ($\sim 2\,\mu\mathrm{s}$) has to be taken into account. Therefore, the TES is not used in CW detection mode. Instead the microlaser is operated in CW mode and an electro-optical modulator (EOM) is placed in the detection path (fiber coupled after passing the spectrometer and spectral selection of the investigated mode) generating square-shaped transmission windows of 15 ns duration at a repetition rate of 1 kHz. Thus, data recording of the TES output signal has to be synchronized to the EOM pulse sequence. This also enables the possibility of identifying zero-photon events in the photon distribution.

The gating time-window is adjusted so that the average measured photon numbers are significantly larger than one and, simultaneously, we are able to distinguish between different dynamical regimes. This is the case as the geometric and Poissonian distribution become very similar for $n_{\mathrm{P}} \leq 1$ (see Fig. 2.4). It should be noted that the transient rise and fall times are very short (300 ps) compared to the duration

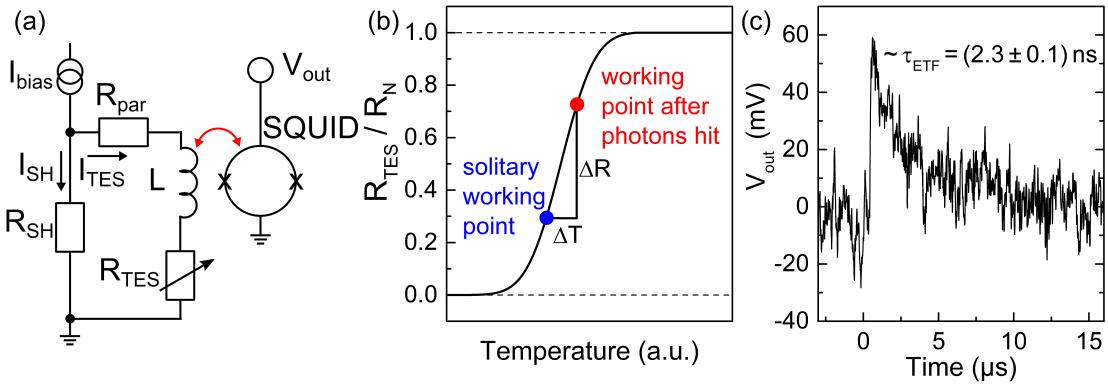

Figure 3.6: (a) Electrical circuit of the TES. The inductance L inductively couples to a SQUID which constitutes a low-noise read-out of the change in current of the TES resulting in a voltage output V_{out}. (b) Illustration of the transition from the superconducting phase to normal phase with finite ohmic resistance R_{N}. (c) Typical signal for the readout of a single photon exhibiting the effect of electro-thermal feedback with a time constant $\tau_{\text{ETF}} = (2.3 \pm 0.1)\,\text{ns}$. ((a) and (b) are adaptations of [DE14])

of the overall optical pulse (15 ns). Therefore, the deviation from an ideal optical square gate can be considered small. Moreover, in case of Poissonian distributions, we do not expect their statistical character to be affected by the gating. For instance, let us assume we take the response function of our amplitude-modulator and separate it into two quasi-square gates of arbitrary temporal length and transmission that add up to the used 15 ns window having an average transmission of the transmission used in the experiment. As the Poissonian distribution P is reproductive, we can conclude that the sum of stochastically independent Poissonian distributed variables X_1 and X_2 with parameters λ_1 and λ_2 is again a Poissonian distribution with parameters $\lambda_1 + \lambda_2$, i.e. $P(\lambda_1) + P(\lambda_2) \propto P(\lambda_1 + \lambda_2)$, as explained by Raikov's theorem [Rai37].

For practical use, the TES is operated very user-friendly with single-mode fiber-coupling [Mil11] and cryogenic-free in a non-commercial compact stand-alone mK-refrigerator design in plug and play fashion[Sch18b]. This is accomplished by integrating a two-stage pulse tube cooling (PCT) system in a vacuum dewar. Figure 3.7 (a) shows the TES system without its vacuum shield. Both PCT stages allow for precooling to a temperature of 2.8 K, while an adiabatic demagnetization process, which is protected by a superconducting magnetic shield, offers cooling of the TES and SQUID detection system to 100 mK [Sch18b].

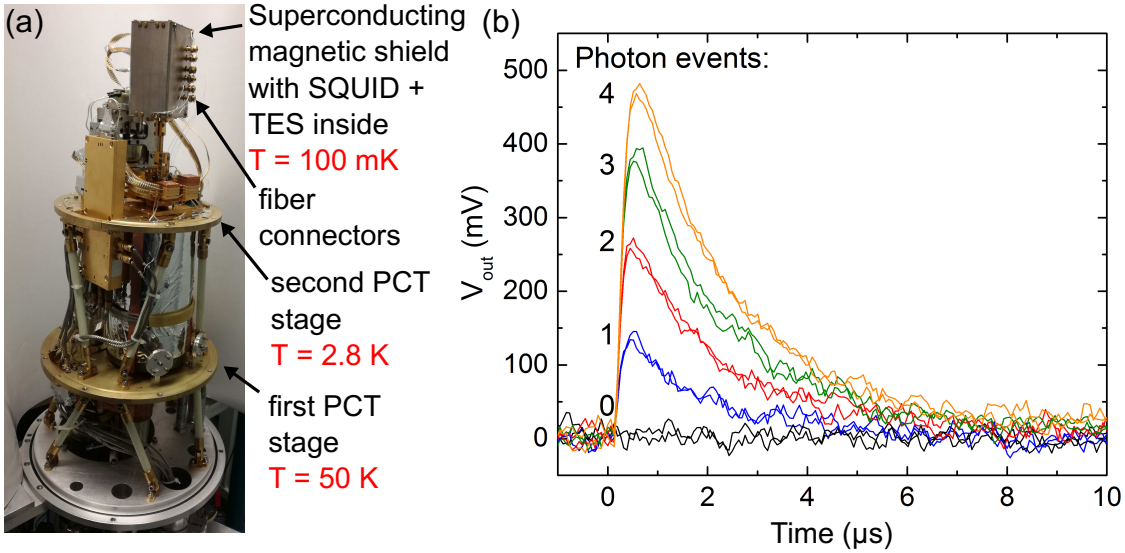

Figure 3.7: (a) Photograph of the TES system. During operation it is covered by a vacuum shield. (b) Exemplary time traces of the SQUID voltage V_{out} for zero to four photon events per detection pulse. With increasing number of photon events the separation of the signals and time-integrals decreases.

Finally, Fig. 3.7 (b) depicts an overlay of several SQUID voltage signals that are typically recorded in the following measurements when microlaser emission is detected by the TES. One can clearly distinguish the number of photons during the chosen gating time in this example from zero to four events. In the later experiments one is able to distinguish between photon events up to a number of 11 per pulse which is mainly limited by the microlaser output power. In general, these TES sensors can detect up to several tens of photons within one gating window [Hum15]. However, in this regime the energy resolution gets too small keep high photon number events apart. Still, by integration over the whole pulse area we are able to evaluate the PND for photon numbers up to 11 in form of histograms as previously presented in Figs. 2.4 and 2.5.

4 Controlling photon statistics in microlasers via time-delayed optical feedback

This chapter presents a detailed study of bimodal QD micropillar lasers when subject to time-delayed feedback. Firstly, the input-output characteristics of two different bimodal microlasers are analyzed. One laser shows a strong change in the output power and the intensity ratio of the two modes and will be labeled microlaser A. Unlike classical semiconductor lasers with rather low-Q resonators, where a threshold reduction is expected when applying optical feedback [Lan80], we find no significant change in the threshold, but a reduction of excitation strength needed to reach certain dynamical regimes in high-β microlasers. The other laser (labeled microlaser B) is robust to the feedback-coupling and only exhibits a minimal change in the input-output characteristics compared to its solitary state. Theoretical modeling of input-output curves for both lasers using semi-classical rate equations provides insight into the parameters necessary to alter the dynamics of the microlasers. The two scenarios give rise to different modifications of the photon statistics in terms of the second-order autocorrelation function and the optical spectrum. Using the TES detector system, one can directly measure the photon-number distribution to evaluate the implications of feedback on the stability of both modes. Figure 4.1 shows an overview of all the experimental techniques used in this chapter and gives a roadmap of the sections 4.1 to 4.3. Lastly, section 4.4 presents investigations under variation of the feedback strength which facilitate tailoring of the underlying dynamics and the modification of their timescale.

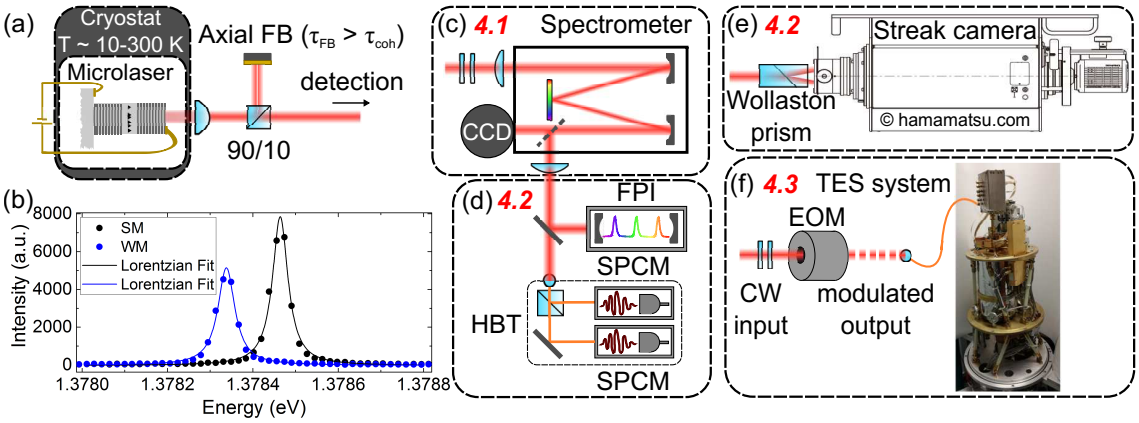

Figure 4.1: Overview of the experimental techniques presented in this chapter: (a) Basic configuration of incoherent feedback. (b) Exemplary spectra of the bimodal microlaser emission. The spectra are fitted with a Lorentzian. (c) Spectrometer with attached CCD used for basic sample characterization in section 4.1. (d) FPI and HBT configuration for high-resolution spectra and second-order autocorrelation measurements in 4.2. (e) Streak camera setup for single-sweep measurements in 4.2. (f) TES system allowing for the visualization of the full photon-number distribution in 4.3.

4.1 Input-output characteristics

Measuring the input-output characteristics is a fundamental tool to determine the optical properties of a laser. In conventional semiconductor lasers with $>$ mW light output powers it is often sufficient to conduct this study with a photodiode to extract key parameters like the excitation current dependence of the optical output, laser threshold current and external differential quantum efficiency. In the following a grating spectrometer is used to determine the input-output characteristics as we are also interested in the optical spectrum. The latter allows access to important information such as emission wavelength and linewidth as well as a differentiation between single and multi-mode emission. Beyond that, we answer the question whether the input-output characteristics is sufficient to decide if the dynamics of a microlaser is affected by optical FB.

The two investigated microlasers show lasing with the gain of hundreds of QDs (out of which about 100-300 effectively contribute to lasing due to sufficient spectral and spatial overlap with the laser mode) resulting in a few tens to hundreds of photons in the cavity with sub-µW output power [Kre17, Rei08]. Their moderately small diameters (A: 4.0 µm and B: 3.8 µm) and the optimized spectral matching of

the QD ensemble emission (at $T \sim 32\,\mathrm{K}$) facilitates lasing on the fundamental Gaussian mode. Higher order transverse modes, which can strongly alter the dynamics of a laser [CH91], are strongly suppressed and will be neglected in the following as the side mode suppression ratio for those modes is up to 30 dB above threshold. The fundamental mode of the bimodal microlaser oscillates in two different states of polarization as the azimuthal order of this mode is zero [Mic13]. Slight deviations from the central symmetry that are inevitable during the fabrication process lead to a lifted mode energy degeneracy [Rei07]. Interestingly, the two modes compete for the common gain medium above lasing threshold leading to complex switching dynamics which have been previously observed both in VCSELs [Vir12] and QD micropillar lasers [Ley13]. Below threshold, both modes are only fed by spontaneous emission and can be treated independently. The mode with higher intensity that wins the gain competition at threshold is labeled *strong mode* (SM), while the other one is called *weak mode* (WM). It should be noted that the modal gain is limited by gain clamping (see section 6.1.3) which typically leads to the scenario where one mode is lasing while the competing mode is not.

Figure 4.2 depicts the input-output curves of the two investigated micropillar lasers. A Lorentzian fit is used to determine the pump current dependence of linewidth, spectral position and area of the optical spectra. The latter is then compared to a direct measurement of the optical output power with a powermeter after a pinhole to ensure only light from the investigated microlaser is detected. Here additional optical losses from the aspheric lens ($\sim 10\,\%$), mirrors ($\sim 2\,\%$) and feedback cavity beamsplitter ($\sim 90\,\%$) have been taken into account. This enables a rescaling of the measured intensity of the CCD into optical output power. Disregarding the external loss channels, numerical modeling can directly access the intracavity photon number. At threshold we find a value of ~ 7 which is consistent with the expected value of $\sim \beta^{-1/2}$ [Ric94, Moo18]. The simulations which were carried out by Christoph Redlich (research group of Prof. Dr. Kathy Lüdge, TU Berlin) quantitatively reproduce the input-output characteristics of both lasers. It should be noted that this thesis only discusses the results of the numerical modeling and its implications on understanding the dynamics of the microlasers, and we refer to the appendix A.1 for details on the numeric model and the used parameters.

In brief, the simulations are carried out with a stochastic delay differential equation system (SDDE) for the bimodal complex electric fields $E_{\mathrm{s,w}}$ (SM and WM re-

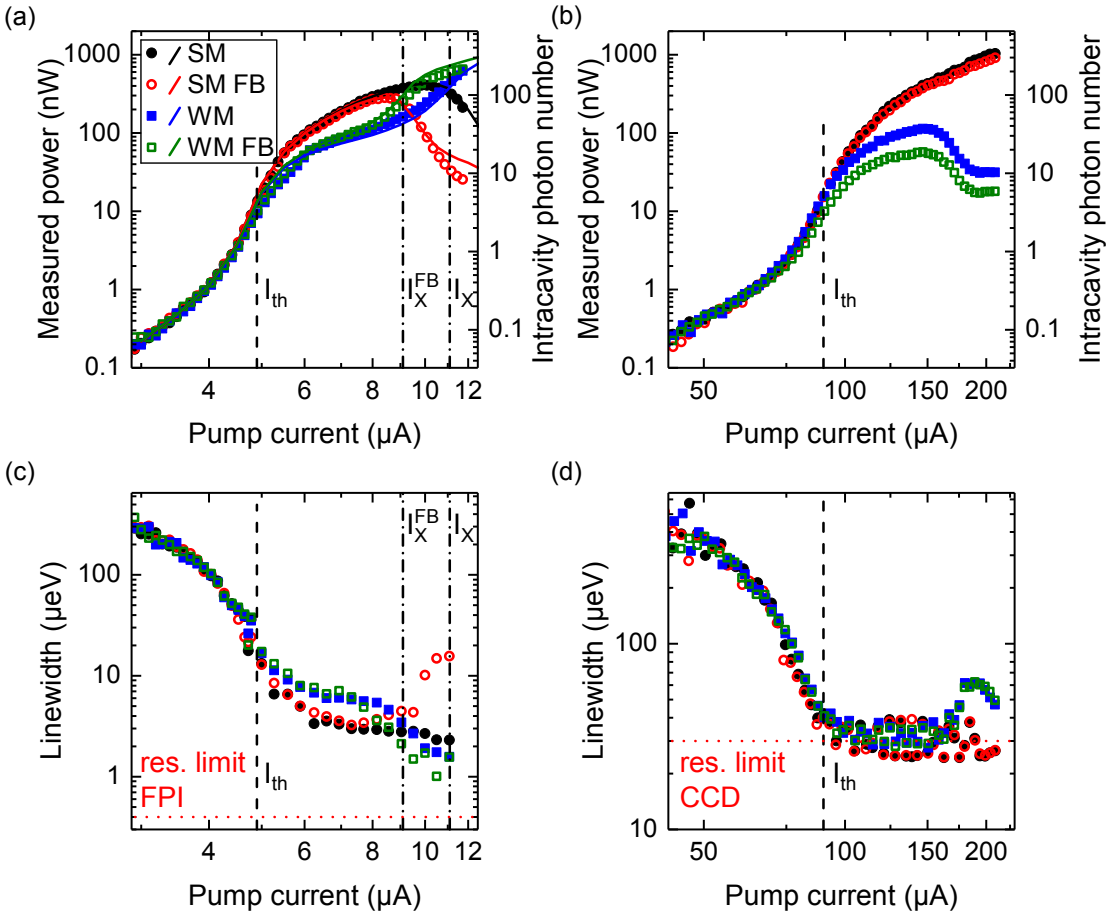

Figure 4.2: Input-output characteristics of bimodal micropillar lasers A (a) and B (b) with and without feedback (FB). Experimentally measured data points are depicted by symbols whereas numerical simulations are indicated by solid lines. The lasing threshold current (I_{th}) is marked by a dashed line. Additionally, laser A shows a crossing in intensity of SM and WM. Correspondingly, those crossing points without and with FB (I_{X} and $I_{\mathrm{X}}^{\mathrm{FB}}$ respectively) are indicated by dashed-dotted lines. Panels (c) and (d) show the linewidth of laser A and B as well as the resolution limit (red dotted line) of the used recording devices.

spectively), the occupation probability ρ of the active QDs and the reservoir carrier density n_r. Additionally, optical feedback is included in the differential equations by adding the term $-K_\mathrm{j}E_\mathrm{j}(t-\tau_\mathrm{FB})$ in the equation of the electric field [Lüd09, Red16]:

$$\frac{d}{dt}E_\mathrm{j}(t) = \tfrac{1}{2}\tfrac{h\nu_0}{\epsilon_0\epsilon_\mathrm{bg}}\tfrac{2Z^\mathrm{QD}}{V}g_\mathrm{j}\,(1+i\alpha)\,[2\rho(t)-1]E_\mathrm{j}(t) - \kappa_\mathrm{j}\,(E_\mathrm{j}(t) - K_\mathrm{j}E_\mathrm{j}(t-\tau_\mathrm{FB})) + \sqrt{\tfrac{h\nu_0}{\epsilon_0\epsilon_\mathrm{bg}}\tfrac{2Z^\mathrm{QD}}{V}\beta\tfrac{\rho}{\tau_\mathrm{sp}}}\xi(t) \tag{4.1}$$

$$\frac{d}{dt}\rho(t) = -\sum_{\mathrm{j}\in\{\mathrm{sw}\}} g_\mathrm{j}[2\rho(t)-1]|E_\mathrm{j}(t)|^2 - \frac{\rho(t)}{\tau_\mathrm{sp}} + S^\mathrm{in}n_\mathrm{r}(t)[1-\rho(t)] \tag{4.2}$$

$$\frac{d}{dt}n_r(t) = \tfrac{\eta}{e_0 A}(I-I_p) - S^\mathrm{in}n_\mathrm{r}(t)\tfrac{2}{A}\tfrac{Z^\mathrm{QD}}{}[1-\rho(t)] - S^\mathrm{in}\tfrac{2}{A}\tfrac{Z^\mathrm{inac}}{}\frac{\rho^\mathrm{inac}}{\tau_\mathrm{sp}} - \frac{n_\mathrm{r}(t)}{\tau_\mathrm{r}} \tag{4.3}$$

$$\text{with } g_\mathrm{j} = \tfrac{|\mu_\mathrm{j}|^2 T_2}{2\hbar^2}\left(1+\varepsilon_\mathrm{js}\tilde{\epsilon}|E_\mathrm{s}(t)|^2 + \varepsilon_\mathrm{jw}\tilde{\epsilon}|E_\mathrm{w}(t)|^2\right)^{-1}. \tag{4.4}$$

In the following we first discuss the experimental observations, and subsequently the parameters that can be extracted from the model (see Table 4.1).

In both lasers the SM depicts a shallow s-shape in their transition to lasing in double logarithmic scale which is typical for a high-β laser. The WM, on the other hand, exhibits a smaller increase in output power at threshold in both cases compared to the SM. The main difference is that in microlaser A the WM shows an increase of intensity for higher excitation current which is accompanied by a simultaneous decrease of the SM, while in microlaser B the WM saturates and eventually decreases in intensity for higher pump powers.

We first focus on the behavior of microlaser A which is depicted in figure 4.2 (a) and (c). The increase of the WM intensity leads to a crossing of the mode output powers at the pump current $I_\mathrm{X} = 11.2\,\mu\mathrm{A}$. To explain this behavior, we first evaluate the spectral shift of both modes with increasing pump power as depicted in 4.3 (a). For pump currents below I_th, the modes shift to higher energies as increasing the carrier density leads to a decrease in refractive index via the plasma effect [Ben90]. When increasing the pump current beyond I_th the modes shift to lower energies as sample heating leads to an expansion of the resonator. As these effects affect the SM and WM equally, the detuning stays constant for all injection currents. Overall the spectral shift is $\sim 50\,\mu\mathrm{eV}$, which does not significantly change the spectral overlap of the gain and the fundamental mode. Consequently, this shift cannot explain the

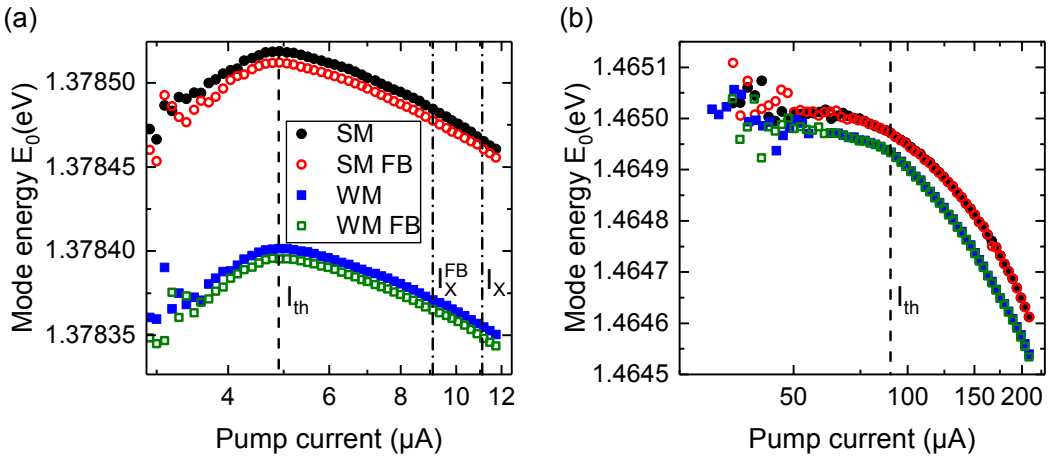

Figure 4.3: Fundamental mode energy of bimodal micropillar lasers A (a) and B (b) with and without feedback (FB). The lasing threshold current (I_{th}) is marked by a dashed line. For laser A the intensity crossing points without and with FB (I_{X} and $I_{\mathrm{X}}^{\mathrm{FB}}$ respectively) are indicated by dashed-dotted lines.

intensity crossing and one has to analyze the coupling between the two modes in more detail which will be done with the help of the aforementioned rate equation model.

Interestingly, a crossing behavior can also be found when investigating the linewidth of the laser. Here a smooth transition of the linewidth reduction at lasing threshold is found. Noteworthy, the data points below threshold are all recorded with the CCD while the ones above are recorded with the FPI for higher spectral resolution. The linewidth reduction of the SM is most pronounced around threshold where we also find the steepest increase in output power when investigating the input-output characteristics. When increasing the pump power further, one can find also a crossing in linewidth of SM and WM which occurs at slightly lower currents than the intensity crossing. Thus, both the power and linewidth indicate that the WM dominates the lasing for sufficiently high pump current.

When examining the characteristics of microlaser B (see figure 4.2 (b) and (d)), we find a different scenario. Here the WM first saturates and then decreases for higher pump current so that the SM and WM do not cross in intensity. As the threshold current in microlaser B $I_{\mathrm{th}} = 90\,\mu\mathrm{A}$ is significantly higher than in case of laser A ($I_{\mathrm{th}} = 4.9\,\mu\mathrm{A}$), we only find a heat-induced red-shift of the mode emission (see Fig. 4.3 (b)). Consequently, this mode shift exhibits a value of $\sim 400\,\mu\mathrm{eV}$ which is higher compared to laser A ($\sim 50\,\mu\mathrm{eV}$). Moreover, the linewidth of the WM

increases when the output power decreases. It has to be noted that the linewidth of microlaser B is fully measured by the spectrometer due to experimental limitations in this case. Thus, the resolution limit of 30 µeV is reached by both modes and lower linewidth cannot be fully spectrally resolved. Therefore, these spectra are fitted with a Voigt function which is a convolution of the Lorentzian emission spectrum and the Gaussian spectral response of the grating spectrometer. This is a good approximation in the narrow linewidth regime as the incident laser beam exhibits a Gaussian cross-section in the spatial domain. Here, the Gaussian part of the Voigt exhibits a constant linewidth of 30 µeV which corresponds to the resolution limit of the grating spectrometer.

When applying optical feedback with an external cavity with a chosen round-trip time $\tau_{\mathrm{FB}} = 5.9\,\mathrm{ns}$, the two lasers show very different behavior. This external cavity length which is greater than the coherence time of the lasers $\lesssim 1\,\mathrm{ns}$ in the used pump regime allows for the investigation of incoherent feedback coupling. We estimate the feedback ratio value by considering the loss channels of the external cavity, namely the 90/10 beamsplitter, the aspheric lens (transmission $\sim 90\,\%$), the external cavity mirror (reflectance $\sim 96\,\%$) and the top DBR mirrors. In total this results in about 60 % of the light being coupled back to the upper microlaser facet. In a previous publication [Sch16] the reflectivity of the upper DBR mirror (with a similar Q-factor) and possible absorption in the DBR mirrors was determined to result in 10 to 20 % of resonantly injected light to be coupled to the active medium. Taking into account all aforementioned loss channels, we estimate about 6 to 12 % of the light being effectively coupled into the active medium of the microlaser. Noteworthy, this result is consistent with the value of 10 % determined by the numerical simulations.

Moreover, for a better assessment of the experimental constrains it is important to examine the alignment accuracy needed to adjust the feedback spot on the micropillar. As discussed in section 3, the external cavity mirror is mounted on a piezo platform with scanning capability of 2 mrad. Taking into account the working distance of the aspheric lens ($w_{\mathrm{asph}} = 1\,\mathrm{cm}$), we can calculate the associated displacement d on the sample:

$$d = 2 * w_{\mathrm{asph}} * \theta, \tag{4.5}$$

where θ is the tilt angle of the external cavity mirror in the limit of small values of θ (which is always given). The maximum displacement of 40 µm is sufficient when

considering that the pillar diameters investigated in this thesis are $\leq 5\,\mu m$.

For the analysis of how the feedback strength is affected by the displacement of the feedback spot we choose micropillar A at the pump current I_X. Here optical feedback leads to a significant decrease of the optical output intensity. Thus, the feedback spot is optimized on the minimal value of the measured output power. Figure 4.4 (a) displays a 20 x 20 map scan of the feedback spot with 0.5 µm step size. Low intensity is color-coded in dark red and can be found only close to the origin which represents the upper facet of the micropillar. A detailed evaluation of the intensity as a function of d is displayed in panel (b). In order to not overload the graph while having reasonable statistics, it shows the intensity values along 4 cuts of Fig. 4.4 (a) which are the horizontal, vertical and both diagonal axes through the origin. We consider that no feedback effect is present if the intensity does not drop below 54 % of its solitary value (in the absence of feedback) as this is the minimal intensity value where the feedback spot is fully off the micropillar. This way one can distinguish between a regime of no feedback effects (shaded in yellow) and one that is affected by feedback (shaded in red). Interestingly, one only finds feedback effects in the range of $\pm\,1.5\,\mu m$ from the center of the upper facet of the micropillar which sets stringent requirements on the mechanical stability of the spectroscopy setup. This feedback range is 1 µm smaller than the micropillar diameter of 4 µm. It has to be noted that the latter is identical to the diameter of the feedback spot. The reason for this behavior can be found in the electric field distribution of a micropillar cavity. The antinode of the electric field is located in the center of the cavity for the Gaussian fundamental mode (HE_{11}). Previous studies have shown that this fundamental mode can only be effectively excited with a Gaussian beam (with a size identical to the micropillar) in the center of the micopillar facet [Cti10]. Excitation with an off-center beam leads to enhanced coupling to other pillar modes which are not lasing. Moreover, QDs that are spatially further away from the center of the cavity are less likely to couple to the lasing mode. The given QD density $5 \cdot 10^{-9}\mathrm{cm}^{-2}$ and the pillar diameter 4 µm yields a total of 650 QDs in the active layer of the microlaser (see table 4.1). Assuming that only QDs within a radius of 1.5 µm contribute to the lasing mode (as those are the only ones affected by feedback), one ends up with 366 QDs (when assuming random growth position of the dots). This value is higher than the one used in the numerical simulations ($Z^{QD} = 250$) which can be attributed to the inhomogeneous spectral properties

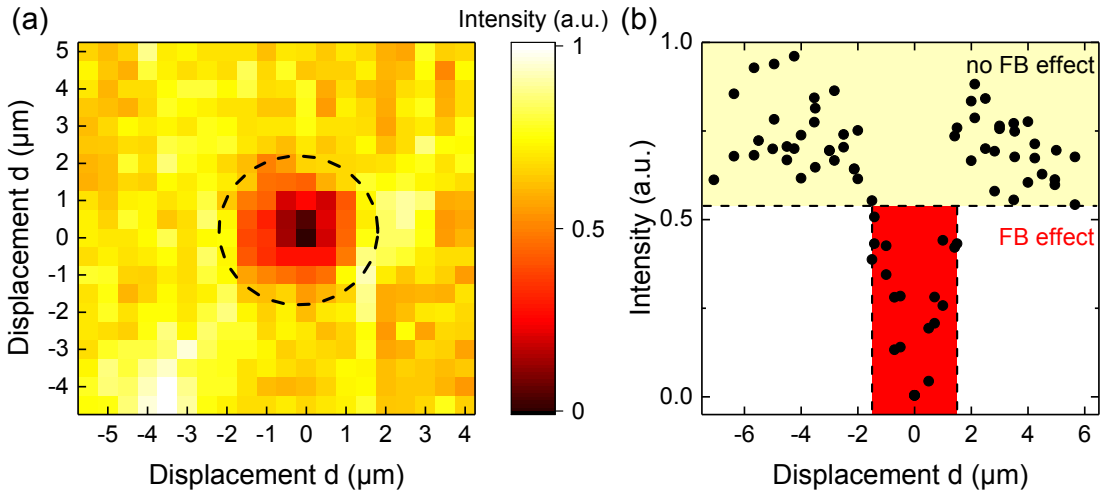

Figure 4.4: (a) 2D intensity map scan of the feedback spot over the micropillar which is placed in the origin. The position of the micropillar is marked by a black dashed circle. (b) Evaluation of the intensity shown in panel (a) along the horizontal, vertical and both diagonal axes.

of the QDs and their non-ideal spectral overlap with the laser mode. Here, the increased measured intensity for displacements $> 2\,\mu$m originates from light being reflected towards the detection path from the gold contact of the microlaser. Thus, when aligning on a positive feedback effect (with regard to intensity), it is crucial to check that the feedback spot on the CMOS camera precisely coincides with the microlaser and not with the gold contact.

In general, it is found that the feedback strength decreases significantly already when moving with the piezo one step (0.5 µm) from the center of the micropillar. Consequently, this alignment procedure is always applied to all feedback experiments shown in this dissertation as the required reproducibility of the feedback strength is not guaranteed by simply aligning the external cavity mirror by hand. Mechanical stability of this alignment is given for about one hour (in an air-conditioned laboratory with close to constant environmental conditions and temperature stability of about 1 K). Therefore, the alignment procedure is also applied between experiments to compensate possible sample drift to a movement of the cryostat. It has to be highlighted that the optical table has vibration damping but the Helium transfer line can be the cause of mechanical strain as it is in contact with the Helium dewar which is in contact with the floor. Noteworthy, for the following chapters the feedback maps have been expanded to 25x25 with 0.4 µm step size. Further reduction

of the step size leads to multiple pixels of close to equal intensity making it difficult to assign the origin of the micropillar.

To improve both coupling to the lasing mode as well as feedback coupling, it might be beneficial that all QDs are located close to the center of the cavity. Therefore, micropillars with site-controlled QDs grown with a buried stressor approach as active medium are excellent candidates for further investigating the regime of low photon numbers. This unique growth technique is very powerful as it simultaneously allows for controlling the number and position of the QDs [Kag18][Kag19]. With these devices lasing has been demonstrated with only ~ 10 QDs in the cavity. Consequently, micropillar lasers based on the buried stressor QD growth concept provide an ideal platform to explore feedback effects in the regime of single emitters. After this explanation of the alignment procedure of the feedback spot, we return to the discussion of the input-output characteristics in the presence of feedback. In the following, we use the maximally available feedback ratio.

In the presence of feedback, laser A depicts a shift of the intensity crossing point to a lower pump current $I_{\mathrm{X}}^{\mathrm{FB}} = 9.1\,\mu\mathrm{A}$. On the other hand, laser B seems to be mainly unaffected by the feedback and only exhibits a decrease in the output power of both modes. In order to evaluate the different behavior to feedback, we compare the results of the numerical simulations which are given in Table 4.1. The two lasers differ in their photon emission energy. This can be explained by the fact that the two lasers were processed on different wafer material. Here, the main parameter influencing the emission energy of a QD is its size as the material composition is identical. Consequently, this also affects the mode volume, mode area, number of (in)active QDs and the QD lifetime. Laser B exhibits a lower number of active QDs, i.e. QDs that are emitting into the lasing mode, as well as higher parasitic currents, which results in a much higher threshold current of 90 µA than laser A with 4.9 µA. Even though all these parameters are very relevant for matching both numerical and experimental results, they mainly influence the scaling and the general shape of the input-output characteristics via the β-factor. The spectral detuning of SM and WM which is used as a parameter in other models [Ley13] is not included explicitly in the present numerical model. From polarization resolved measurement we can extract a mode splitting of $\Delta_{\mathrm{A}} = 106\,\mu\mathrm{eV}$ for laser A and $\Delta_{\mathrm{B}} = 33\,\mu\mathrm{eV}$ as depicted in Fig. 4.5, which is much smaller than the inhomogeneous broadening of $\sim 30\,\mathrm{meV}$ expected for these InGaAs QDs. One can directly access Δ by putting a combination

Given parameter			
Parameter	Symbol	Laser A	Laser B
Photon energy	$E_0 = h\nu_0$	1.38 eV	1.46 eV
Carrier lifetime reservoir	τ_r	1 ns	1 ns
Effective Scattering rate	S^in	$7{\cdot}10^{-15} m^2 ps^{-1}$	$1{\cdot}10^{-16} m^2 ps^{-1}$
Mode volume	V	4.0 µm^3	6.3 µm^3
Number of (in)active QDs	$Z^{\mathrm{QD\ (inac)}}$	250 (400)	110 (200)
Refractive index of background medium (GaAs)	n_bg	3.34	3.34
	$\tilde{\epsilon}$	$\epsilon_0 n_\mathrm{bg} c_0$	$\epsilon_0 n_\mathrm{bg} c_0$
QD lifetime	τ_sp	230 ps	150 ps
Effective dephasing time	T_2	330 fs	330 fs
Mode area	A	3.1µm^2	3.1µm^2

Fitted parameter			
Parameter	Symbol	Laser A	Laser B
Spontaneous emission factor	β	$1.8 \cdot 10^{-2}$	$5.6 \cdot 10^{-3}$
Optical cavity losses strong (weak) mode	κ_s (κ_w)	52.0 (54.7) ns^{-1}	39.0 (41.0) ns^{-1}
Dipole transition moment strong (weak) mode	μ_s (μ_w)	2.50 (2.42) nm $\cdot\, e_0$	3.70 (3.75) nm $\cdot\, e_0$
Auto-compression factors	ϵ_ss	$29 \cdot 10^{-10} \frac{m^2}{AV}$	$70 \cdot 10^{-10} \frac{m^2}{AV}$
-	ϵ_ww	$24 \cdot 10^{-10} \frac{m^2}{AV}$	$50 \cdot 10^{-10} \frac{m^2}{AV}$
Cross-compression factors	ϵ_ws	$31 \cdot 10^{-10} \frac{m^2}{AV}$	$150 \cdot 10^{-10} \frac{m^2}{AV}$
-	ϵ_sw	$42 \cdot 10^{-10} \frac{m^2}{AV}$	$160 \cdot 10^{-10} \frac{m^2}{AV}$
Parasitic currents	I_P	2.7 µA	42.5 µA
Pump efficiency	η	$9.4 \cdot 10^{-2}$	$1.28 \cdot 10^{-3}$
Linewidth enhancement factor	α	1	1

Table 4.1: Table of parameters used for the numerical simulations. The top part of the table depicts the given parameters that are based on device parameters, while the bottom part shows the fitted parameters that are adjusted to reproduce the experimental results.

of a rotatable a half-wave plate and a linear polarizer in fixed orientation into the detection beam path. The mode splitting can then be extracted from the amplitude of a sinusoidal fit of the fundamental mode energy.

In the used model the modes are directly coupled via gain competition which is in contrast to the indirect coupling used in the spin-flip model (SFM) [SM95, Vir12]. This approach can be justified with the assumption that both modes are a superposition of elliptically polarized modes, that are coupled to two transitions with opposite spin. In our model one can deduce the term that is equal to the used

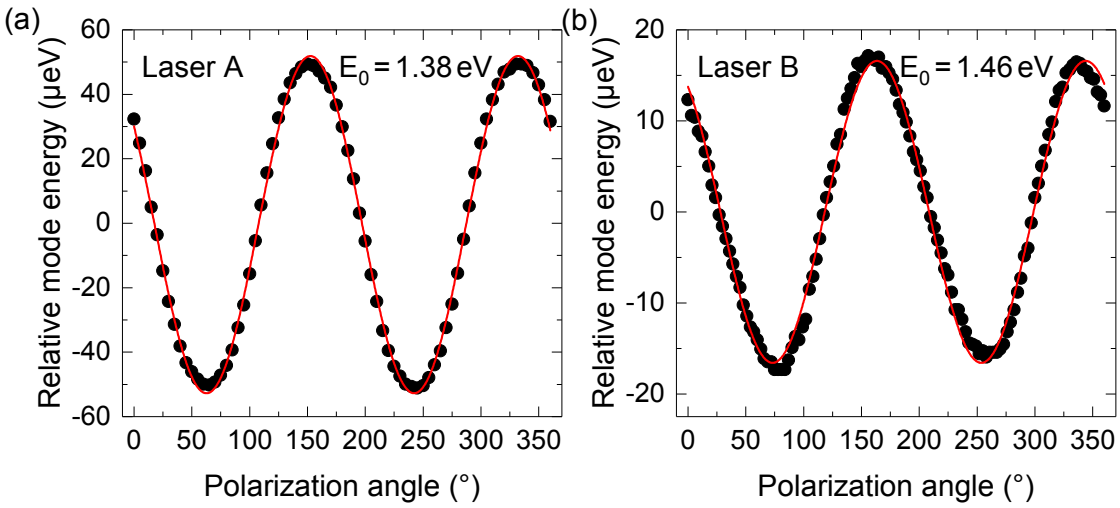

Figure 4.5: Polarization series of the micropillar lasers (a) A and (b) B. Black dots depict experimental data while a sinusoidal fit of the data is shown as a red line. The mode energy is given relative to the photon energy E_0 of each microlaser.

gain compression taking into account that both modes compete for the common QD gain medium. If both modes emitted photons at the same time the light would be elliptically polarized, which would lead to different emission rates of the two transitions. Therefore, the SFM would be suitable for the description of VCSEL devices showing complex elliptic polarization dynamics. Nevertheless, in the limit of having only linear polarized light output, as in the case for the investigated devices, the SFM can be reduced to a model similar to the one that we use. The asymmetric mode transitions, as described for instance by Leymann et al. [Ley17], are very difficult to calculate from first principles and would need to be added to the model phenomenologically, as not all required device parameters or its exact geometry are known. In the model used here, we therefore minimize the number of free parameters by including only the phenomenological gain compression terms to keep a low number of fitting parameters while still qualitatively and quantitatively reproducing the experimental findings. The available gain for the competing mode is reduced which is quantified by the positive cross-compression factor. Taking into account that the mode splitting in laser A (106 μeV) is much larger than the one of laser B (33 μeV), one can understand the difference in the gain and cross-gain compression factors: An increase of the mode splitting leads to a decrease of these factors as the gain coupling of the modes is reduced. Thus, the high compression factors in laser

B lead to a strong suppression of the WM with increased pump. Optical feedback does not change this scenario as the switching dynamics are dominated by the SM. In laser A the lower compression factors allow the WM to eventually take over as the dominant lasing mode, which can be understood as follows. At threshold first the mode with better gain-to-loss ratio (see κ_s) undergoes the lasing transition. On the other hand, in the limit of high excitation the intermode kinetics determine the mode which acquires the higher intra-cavity photon number and exhibits coherent emission [Ley17]. Here, feedback strongly influences the switching dynamics as both modes compete for the gain while barely suppressing each other. Taking into account that both modes are coupled back into the microlaser simultaneously in the presence of unpolarized feedback, this leads to a shift of the intensity crossing point to lower currents. This shift will be explained in the following sections as it can be understood by the bimodal dynamics that are analyzed by correlation measurements.

Additionally, one has to note that here a phenomenological linewidth enhancement factor $\alpha = 1$ is used as no experimental data were present at that time for QD microlasers. In section 6.1 this important parameter will be experimentally determined for the first time for QD microlasers and discussed in detail.

To conclude, the input-output characteristics of bimodal micropillar lasers already gives valuable information on the sensitivity of a mircolaser to time-delayed optical feedback. Low mode splittings that result in high cross-compression factors favor lasing of one mode and suppression of the other mode. In this case, the pillar is more robust to feedback coupling.

4.2 Correlation and spectral properties

In order to investigate the influence of feedback on the dynamics of the system, one has to take into account the correlation functions and spectral properties of the microlasers. At sufficiently high light powers ($\sim 1\,\mathrm{mW}$) photodiodes can achieve multiple GHz bandwidth operation at a signal-to-noise ratio, where one can directly record the temporal dynamics of a laser [Ros17]. In classical semiconductor lasers, for instance in a single-mode Fabry-Pérot laser diode, one can observe complex dynamical phenomena such as low-frequency fluctuations, coherence collapse or stable emission on a single external cavity mode [Hei01]. These dynamics can be described

with the aforementioned LK equations 2.23 and 2.24. The microlasers investigated in this thesis on the other hand typically operate with sub-μW output powers. Thus, the second-order autocorrelation function $g^{(2)}(\tau)$ is used as a powerful tool for investigating the dynamics of microlasers [Alb11]. Here, the emission of one mode showing dynamical effects such as pulsing emission is directly indicated by a deviation from a perfect laser source which has a Poissonian behavior with constant $g^{(2)}(\tau) = 1$. In a previous publication by Albert et al. [Alb11] the multiphoton pulses of the non-lasing mode were simulated as random spiking patterns leading to a pronounced bunching at zero delay. The authors based these calculations on simple LK equations without specifically including parameters of the QD emitters and the gain competition of the bimodal emission. We again use the more advanced model introduced in the previous section (see also Appendix A.1) to describe the dynamics of the micropillar lasers. This way we aim to obtain a deeper understanding of the switching dynamics and the relevant timescales in the presence of feedback. We analyze the behavior of the autocorrelation function with respect to the pump current for both microlasers A and B in separate subsections.

Microlaser A

In the input-output characteristics of microlaser A we find crossing in the intensity of the SM and WM for high injection currents. In this section we analyze the implications of this behavior with regard to the bimodal emission dynamics with a measurement of $g^{(2)}(\tau)$. Additionally, the crosscorrelation of the intensity of the SM and WM unambiguously shows that the two modes are anticorrelated which provides a proof for the indications of switching dynamics.

Figure 4.6 shows $g^{(2)}(\tau)$ for both SM and WM in absence and presence of optical feedback. The important figures of merit $g^{(2)}(\tau = 0)$ and the correlation time τ_{corr} are extracted and depicted in Fig. 4.7. The latter quantifies the decay constant of $g^{(2)}(\tau)$ and is defined by:

$$g^{(2)}(\tau) = 1 + (g^{(2)}(0) - 1)e^{-2|\tau|/\tau_{\mathrm{corr}}}, \tag{4.6}$$

in analogy to the Siegert relation (see equation 2.19). For the SM one expects a smooth transition from thermal to coherent emission above lasing threshold. When using pump currents close to threshold this thermal bunching, which is characterized

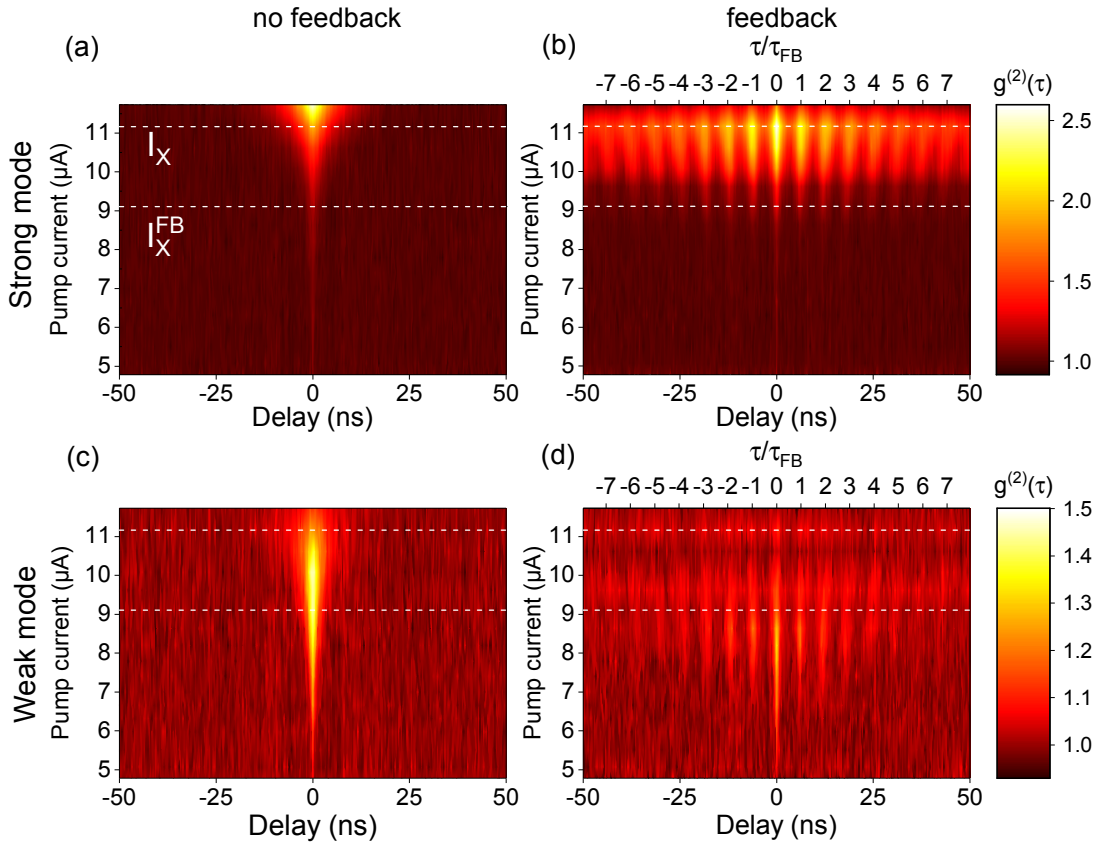

Figure 4.6: Experimental measurements of $g^{(2)}(\tau)$ for various pump currents depicted as a heatmap. Light colors refer to areas of high photon bunching. The intensity crossing points I_X and I_X^FB are highlighted by white dashed lines. For experiments in the presence of feedback (panels (b) and (d)) an upper x-axis shows the delay τ in multiples of the external cavity round-trip time τ_FB indicating the feedback-induced revival peaks.

by $g^{(2)}(0)=2$, cannot be resolved as the temporal resolution of the SPCMs (57 ps in HBT configuration) is higher than the coherence times of about 10 ps. The WM does not experience a full transition to lasing associated with $g^{(2)}(0)=1$. This behavior can be attributed to switching dynamics between the SM and WM which is displayed by $g^{(2)}(\tau)>1$ [Ley13]. Even though the bunching itself is no unambiguous proof for switching dynamics, further measurements and numerical simulations will give evidence to this assumption. At the intensity crossing point I_X, $g^{(2)}(\tau=0)$ exhibits the behavior already expected from the input-output characteristics: The SM becomes super-thermal $g^{(2)}(\tau=0)>2$ while the WM approaches lasing $g^{(2)}(\tau)\to 1$ implying a change of the role of both modes. The super-thermal bunching of the SM can be un-

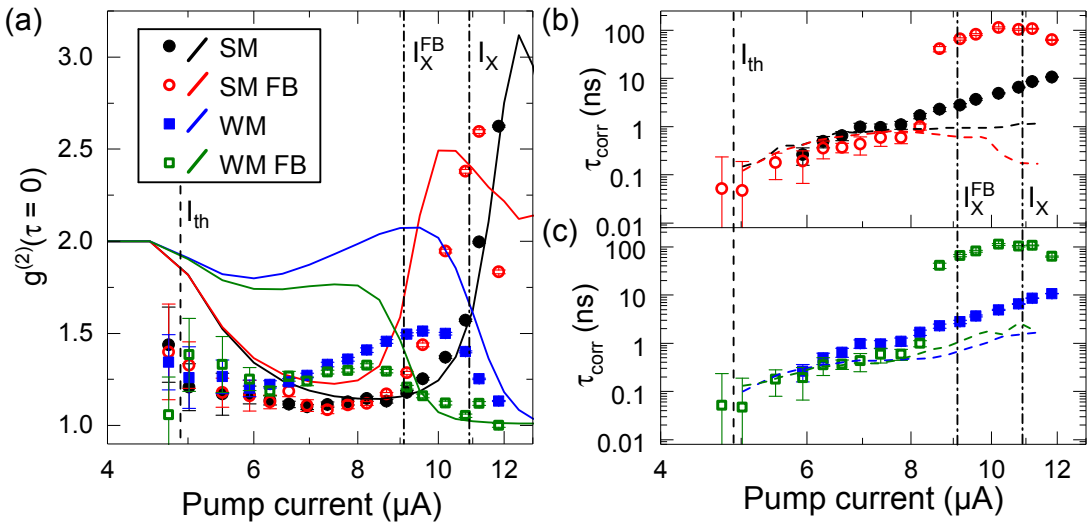

Figure 4.7: Experimentally measured and simulated pump dependence of the second-order autocorrelation function $g^{(2)}(\tau)$ (a) and correlation times τ_{corr} (b,c). Panels (b) and (c) additionally depict the coherence times τ_{coh} calculated from the measured FPI spectra (colored dashed lines). Analogous to figure 4.2 the threshold and intensity crossing currents are indicated by dashed and dash-dotted lines.

derstood in light of the simulation presented in Fig. 2.5 (d): When the SM becomes mainly a thermal emitter, at certain times it is still switching to a coherent state with higher average intracavity photon number. Figures 4.7 (b) and (c) compare the correlation time τ_{corr} with the coherence time τ_{coh} which can be extracted from the linewidth of the measured single-mode optical spectra using equation 2.11. The correlation time monotonously increases from $\sim 100\,\mathrm{ps}$ to $10\,\mathrm{ns}$ and starts deviating significantly from the coherence time, which is $\lesssim 1\,\mathrm{ns}$ for pump currents $I > 8.2\,\mu\mathrm{A}$. Therefore, we assume that the correlation time is equal to the switching timescale of the system. Please note that this assumption is consistent with the crosscorrelation and single-shot streak camera measurements presented later in this section. The increase of this timescale can be explained with a simple Kramers hopping problem [Wil99]. The two modes form a double-well potential with a potential barrier in between. The barrier scales with the pump current, while jumps between the wells are initiated by spontaneous emission. Therefore, increased pump power leads to an increase of the dwell time in each mode.

Applying optical feedback, one can observe significant changes in $g^{(2)}(\tau)$. Analogous to the input-output characteristics, where feedback shifts the intensity crossing

point I_X to lower pump currents, one can observe a shift of the dynamical regimes to lower pump currents in $g^{(2)}(\tau)$. In Fig. 4.7 (a) we observe that the SM shows super-thermal bunching at lower excitation currents than in the case without feedback. The full autocorrelation function as seen in Fig. 4.6 also reveals revival peaks with a temporal separation equal to the cavity round-trip time $\tau_{FB} = 5.9\,\text{ns}$. The revival peaks are more pronounced with increased switching induced bunching at high injection currents. Moreover, one can observe an interaction of the revival peaks with the correlation time: For injection currents $I < 8.2\,\mu\text{A}$ feedback suppresses the noise-induced switching dynamics as in this regime the switching timescale is still lower than or close to the coherence time (see Fig. 4.7 (b) and (c)). For high pump currents $I > 8.2\,\mu\text{A}$ where the switching timescale is larger than τ_{coh} both modes experience a significant increase of τ_{corr} of about two orders of magnitude. This again can be related to a much longer dwell time of the respective mode in the switching process.

For a better understanding of the relationship between the different timescales involved in the experiment (τ_{coh}, τ_{corr} and τ_{FB}), it is advantageous to compare the autocorrelation measurement with the corresponding high resolution optical spectrum of the micropillar emission. Figure 4.8 shows a juxtaposition of both measurements at the intensity crossing points I_X^{FB} (upper panel) and I_X (lower panel). Figures 4.8 (a) and (c) depict high resolution spectra for the SM and WM, respectively. We identify a modulation of the intensity in the optical spectrum when feedback is applied. This is caused by the interaction between the solitary laser mode and the external cavity modes (ECMs). Those ECMs have a characteristic frequency spacing $\Delta f_{ECM} = 169\,\text{MHz}$ which corresponds to the inverse of $\tau_{FB} = 5.9\,\text{ns}$. Thus, the ECMs in the optical spectrum are the counterpart of the revival peaks in the autocorrelation function (see 4.8 (b) and (d)) in the frequency domain. All ECMs are resolution limited in the FPI and thus have a FWHM $< 100\,\text{MHz}$. Especially in the WM where one ECM is favored, this leads to a stabilization of lasing in this mode, thus reducing $g^{(2)}(0)$ (see Fig. 4.8 (d)). The coherence time of both modes is barely affected by feedback.

When increasing the pump current to I_X, this scenario changes drastically (see Fig. 4.8 (e)-(h)). The SM undergoes a linewidth collapse when feedback is applied and ECMs are no longer visible. Here the line becomes strongly asymmetric and broadens to the multi-GHz range. In the autocorrelation function this is accompanied by

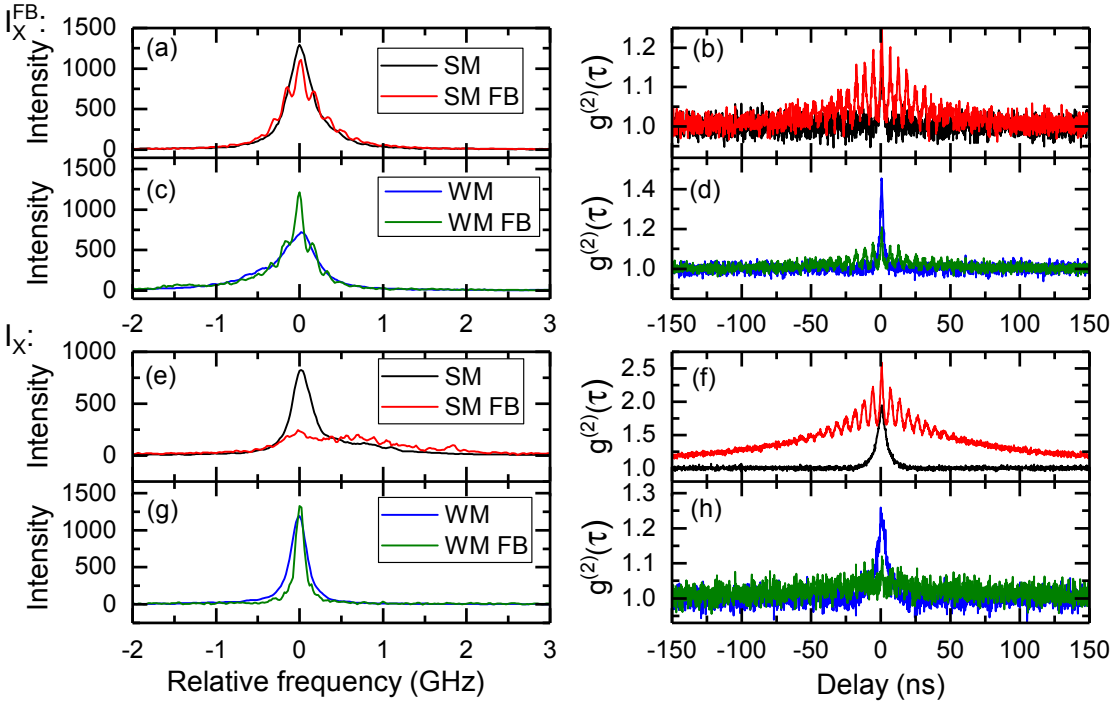

Figure 4.8: High resolution optical spectra (left panels) measured with the FPI (100 MHz frequency resolution) and corresponding $g^{(2)}(\tau)$ (right panels) for both absence and presence of feedback. For panels (a)-(d) a pump current equal to I_X^{FB} was used and while panels (e)-(h) depict a pump of I_X.

super-thermal bunching with $g^{(2)}(0) = 2.6$ and an increase of $\tau_{corr} > 100$ ns. Simultaneously, the WM depicts emission of only one ECM. This reduction in linewidth is accompanied by an increase of the coherence time from 1.45 ns to 2.75 ns (see Fig. 4.8 (g) and 4.7 (c), respectively). Consequently, $g^{(2)}(\tau)$ approaches unity as can be seen in Fig. 4.8 (h). Thus, the WM becomes the dominant lasing mode (see Fig. 4.1 (a)). The slow switching timescale of terms of τ_{corr} that is evident for pumping at I_X can be explained by a mixing of the involved timescales in the dynamics: The strong divergence of SM and WM coherence times, $\tau_{coh,SM} = 177$ ps and $\tau_{coh,WM} = 2.75$ ns respectively, results in longer switching timescales.

Up to this point several indirect measurements exhibiting indications of switching dynamics have been presented. Therefore, we specifically investigate the intensity correlations between the SM and WM of the microlaser as a next step. Experimentally this can be achieved by measuring the cross-correlation $g^{(2)}_{SM\text{-}WM}(\tau)$ as shown in figure 4.9 (a). For the pump current value below threshold ($I = 4.6\,\mu$A) no temporal correlation between SM and WM intensity is observed, as evidenced by the

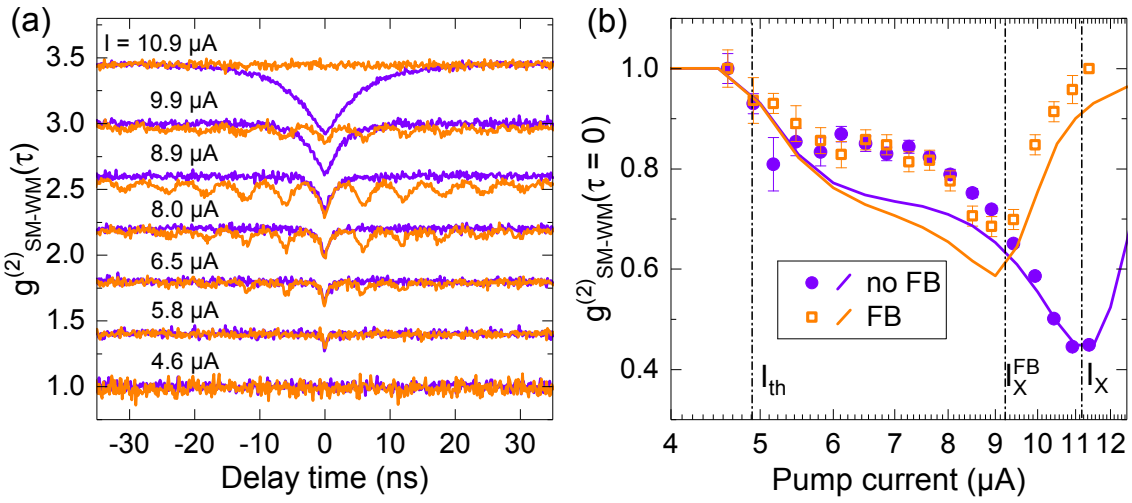

Figure 4.9: Crosscorrelation of the SM and WM intensities $g^{(2)}_{\text{SM-WM}}(\tau)$. Panel (a) compares the measured correlations for different pump currents without feedback (orange) and with feedback (purple). Panel (b) shows measured and simulated data for $g^{(2)}_{\text{SM-WM}}$ at zero delay as a function of the pump current. Numerical simulations are plotted in solid lines while and experimental data are depicted as symbols.

constant $g^{(2)}_{\text{SM-WM}}(\tau) = 1$. Increasing the current above lasing threshold results in $g^{(2)}_{\text{SM-WM}}(\tau = 0) < 1$ which is proving that both modes show anti-correlated dynamics due to gain competition. This important feature, which is also separately displayed in 4.9 (b), becomes minimal at the intensity crossing point I_{X}. Applying optical feedback again leads to a shift of this minimum to I_{X}^{FB} which is consistent with the earlier observed reduction of the pump current needed to access this dynamical regime of mode switching. When the pump current is increased further, feedback stabilizes WM lasing ($g^{(2)}_{\text{WM}}(\tau) \to 1$, see Fig. 4.7 (a)). The switching events become very rare resulting in $g^{(2)}_{\text{SM-WM}}(\tau) \to 1$ and a suppression of the anti-correlated dynamics. This behavior is attributed to the fact that the switching rate reaches a maximum at the intensity crossing points. Numerical simulations, which are depicted as solid lines in Fig. 4.7 (b), provide good qualitative agreement with the experimental data. This indicates that the fitted auto- and cross-compression factors are able to describe not only the input-output characteristics but also the bimodal dynamics of the microlaser. Moreover, the simulations show that for higher pump currents (which were not available in the experiment to prevent heat damage to the sample) one also finds a reduction of the switching event in the absence of feedback. This is another dynamical feature that is shifted to lower pump currents in the presence of feed-

back. Slightly higher experimental values of the crosscorrelation function compared to numerics are caused by the polarizing beamsplitter which exhibits a finite splitting ratio of the two linearly polarized modes. Thus, the non-perfect polarization suppression of the counterpart mode leads to an artificial increase of $g^{(2)}_{\text{SM-WM}}(\tau = 0)$. Moreover, revival peaks are conserved in this cross-correlation measurement. This means that the switching events are actually pinned to the external cavity roundtrip time proving the previously discussed mixing of timescales. In other words, the switching events on the slower timescale $\tau_{\text{corr}} \sim 100\,\text{ns}$ are superimposed by the ones on the fast timescale $\tau_{\text{FB}} = 5.9\,\text{ns}$. When one mode is stabilized by optical feedback, the fast feedback-induced switching is suppressed.

Microlaser B

In the input-output characteristics of microlaser B we find a strong difference in the intensity of the SM and WM for high injection currents. Therefore, one has to analyze the implications of this behavior with regard to the switching dynamics. In this case, we find much slower dynamics with $\tau_{\text{corr}} \gtrsim 1\,\text{ns}$ so that we are able to directly record single-shot time traces with the streak camera in addition to the correlation measurements. This way we can unambiguously show that τ_{corr} is a measure of the switching timescale.

The behavior of the second-order autocorrelation function of laser B is very different from laser A as already expected from respective input-output curves. For laser B we limit the discussion of the autocorrelation measurements to the important signatures of switching dynamics which are $g^{(2)}(\tau = 0)$ and τ_{corr} as shown in Fig. 4.10.

For the pump currents below 130 µA one observes similar values of $g^{(2)}(0)$ for both modes in Fig. 4.10 (a). This can be explained by the fact that neither of the two modes is dominant in the switching process. At the pump current of 135 µA and above we detect a strong deviation of $g^{(2)}(\tau = 0)$ for SM and WM. Here the WM exhibits super-thermal bunching while the SM shows $g^{(2)}(0) \sim 1$. The switching events get less frequent for increasing current beyond 175 µA as the relative amount of spontaneous emission noise that triggers the switching process decreases compared to the difference in intensity of both modes [Red16] (see Fig. 4.2 (b)). In bifurcation theory this can be understood by an increasing distance of the stable solutions of the

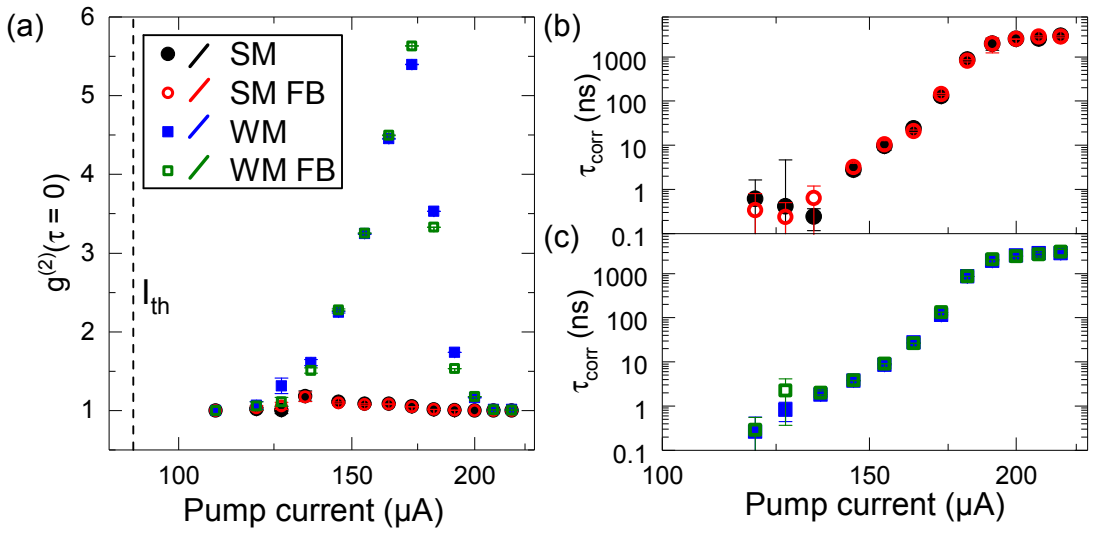

Figure 4.10: Experimentally measured pump dependence of the second-order autocorrelation function (a) and correlation times (b,c).

two modes with increasing current and a close to constant noise strength causing the switching events to occur less frequently [Red16]. Thus, the SM is mainly in a lasing state with only short interruption of WM pulses which leads to a high variance and consequently a prominent bunching of the latter one. For a pump current of 173 μA the WM bunching reaches a maximum of $g^{(2)}(0) = 5.4$ which is significantly higher than the maximum of $g^{(2)}(0) = 2.6$ in the case of laser A. This can be explained by the fact that the difference in intensities of both modes is bigger for laser B if compared to laser A which is in full agreement with the simulations presented in Fig. 2.5 (b) and (d). For higher pump currents the WM is then stabilized by feedback in its thermal state which is also evident from the increased linewidth (see Fig.4.2 (d)). Both modes strongly diverge in intensity which can be explained by an increase of the distance of the two stable solutions in phase space. Therefore, spontaneous emission is not strong enough trigger a switching process [Red16]. Accordingly, one expects a perfectly thermal state with $g^{(2)}(0) = 2$ for the WM. Again we are unable to resolve this feature because of lacking temporal resolution of the SPCMs. Numerical simulations show that the regime of switching and its suppression for high pump are strongly dependent on the β-factor [Red16]. Increasing β shifts the border between theses regimes to higher currents as expected from the increased noise contribution in high-β microlasers that can trigger switching events even for a larger intensity difference of both modes.

The correlation times exhibit a similar scenario as in microlaser A. Both modes show a monotonous increase of τ_{corr}. The increased difference of the linewidth and thus also the coherence time of SM and WM leads to higher correlation times of up to 3 µs. As already expected from the input-output characteristics in Fig. 4.2 (b), the second-order autocorrelation function is barely affected by optical feedback. While we observe a slight increase of $g^{(2)}(0)$ for $I = 173\,\mu$A and a decrease for $I = 182\,\mu$A and $I = 191\,\mu$A of ~ 0.2, a shift of dynamical regimes or a change of timescales is not present for microlaser B.

For microlaser A we were able to directly investigate the anti-correlated dynamics by a crosscorrelation measurement between the SM and WM intensity. As the correlation time and thus the dwell time of the system is with up to 3 µs more than one order of magnitude longer than in the case of laser A, we are able to directly access this switching in a time-resolved measurement. To do so, we apply time-resolved spectroscopy with the setup described in section 3.2. This includes a Wollaston prism in front of a streak camera, which enables us to record the time trace of both SM and WM simultaneously. The following measurement was a collaborative effort between the author of this work and Sören Kreinberg, Elisabeth Schlottmann and Janik Wolters (see also [Red16]). Moreover, this measurement is only possible with microlaser B with emission at 850 nm as the cathode in the used universal streak camera is not optimized for NIR and its quantum efficiency drops exponentially for wavelengths 900 nm [Ham18], as being the case for microlaser A. Additionally, we can only perform this measurement without feedback as additional losses (of the beam splitter forming a feedback cavity) lead to an insufficient signal-to-noise ratio (SNR) where one cannot distinguish between dark counts of the streak camera and detected photons.

Figure 4.11 (a) depicts a polarization resolved 2 ms long single-shot time trace of microlaser B at a pump current of 173 µA which leads to the maximum bunching (see Fig. 4.10 (a)). We would like to note that this measurement was only performed at this pump current as decreasing the carrier injection leads to too fast dynamics which we were not able to resolve while increasing the current leads to a decrease of WM intensity resulting in a too low SNR of the mode. The time trace is color-coded with increasing intensity from blue to red. By integrating a small spectral area around both SM and WM (see red boxes), one can visualize the intensity time trace of both modes as shown in 4.11 (b). When defining a switching event as a pulse of photons

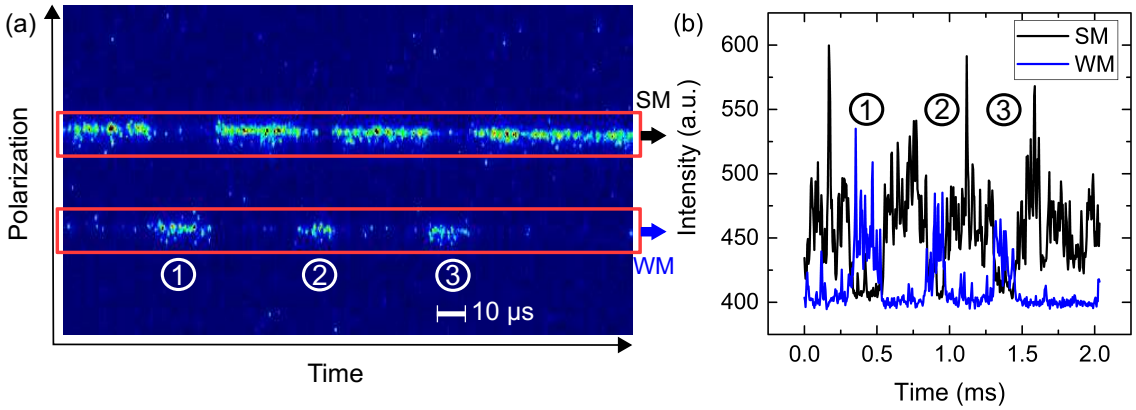

Figure 4.11: (a) Exemplary streak camera measurement trace. Increasing intensity is color-coded from blue to red. (b) Integrated intensity of the area marked in red boxes. Black line corresponds to the SM intensity and the blue line to the WM, respectively. The related integration areas are marked by arrows of the same color. The three long turn-on phases of about 10-30 µs of the WM are marked with numbers 1, 2 and 3.

of the WM that is stronger in intensity as the SM [Red16], we can see several of those events in Fig. 4.11 (a). Most evident are the three long turn-on phases of the WM with a duration of about 10-30 µs (marked with numbers 1, 2 and 3). Especially at the beginning of the trace, one can also observe shorter switching events which are close to the resolution limit of 1 µs for the chosen time range of 2 ms. As already expected from the cross-correlation measurements of microlaser A, we observe a clear anti-correlation in the switching process, i.e. switching causes an increase of intensity in one mode while the counterpart mode decreases simultaneously. It should be noted that this is an exemplary time-trace that includes several switching events. As expected from the high value of $g^{(2)}(0) = 5.4$ in Fig. 4.10 (a), switching events are very rare and most recorded traces show either no or only very few switching events. These events are mostly short as expected from the sub-µs correlation time that was extracted from the autocorrelation measurements (see Fig. 4.10 (b) and (c)).

4.3 Photon-number distribution

After thoroughly analyzing the switching dynamics by correlation measurements as well as by time-resolved streak camera studies, we next discuss the photon-number

distribution. As the main interest of this chapter is to identify and understand the change of photon statistics in the presence of optical feedback, we restrict this analysis to microlaser A. A detailed study of the photon-number distribution of different micropillar lasers, which show different switching behavior without feedback can be found in [Sch18a].

The starting point of this analysis is a numerical simulation done again by Christoph Redlich, TU Berlin. When recording the input-output characteristics with a CCD, one needs a finite integration time to obtain a sufficiently high SNR. Thus, switching dynamics and instabilities are not evident from this measurement. By calculating a multitude of numerical time series, one also obtains the input-output characteristics but with the additional information of the photon-number distribution of each mode. Therefore, we gain insight beyond the simple measurements of the individual modes output powers as the time-series highlight the temporal stability of each mode. As the numerical simulations include a stochastic noise term one can plot the statistical distribution of the intensity of both SM and WM for various pump conditions by calculating a multitude of different noise implementations.

Figure 4.12 presents the result of 50000 noise realizations with increasing pump current in steps of 0.5 µA. These noise realizations are the different results of time-series with identical parameters as the stochastic noise term (that simulates the β-factor) leads to an ensemble of solutions. The scale of the depicted heat map displays the probability of the microlaser emitting a distinct intracavity photon number. Firstly, we discuss the scenario where no feedback is present as shown in panels (a) and (b). Above the lasing threshold of $I_{\mathrm{th}} = 4.9\,\mu\mathrm{A}$ one first observes a turn-on of the SM. Accordingly, the WM emits preferably at low intracavity photon numbers resulting in stable emission of the SM. Further increasing the pump current to the range of ~ 8-$11\,\mu\mathrm{A}$ the microlaser enters a regime of bimodal emission. Here both modes display considerable probabilities for both low and high photon numbers. This result is in agreement with previous autocorrelation measurements which exhibit $g^{(2)}(0) > 1$ for both modes indicating a mixture of thermal and coherent emission. When further increasing the pump current, one observes that the SM mainly emits at low photon numbers while the WM is stabilized at high photon numbers. Accordingly, $g^{(2)}(0) > 2$ can be observed for the SM as multiphoton pulses lead to a high variance in the photon-number distribution during turn-on of the mode. At the same time the stabilization of the WM as the dominant lasing mode

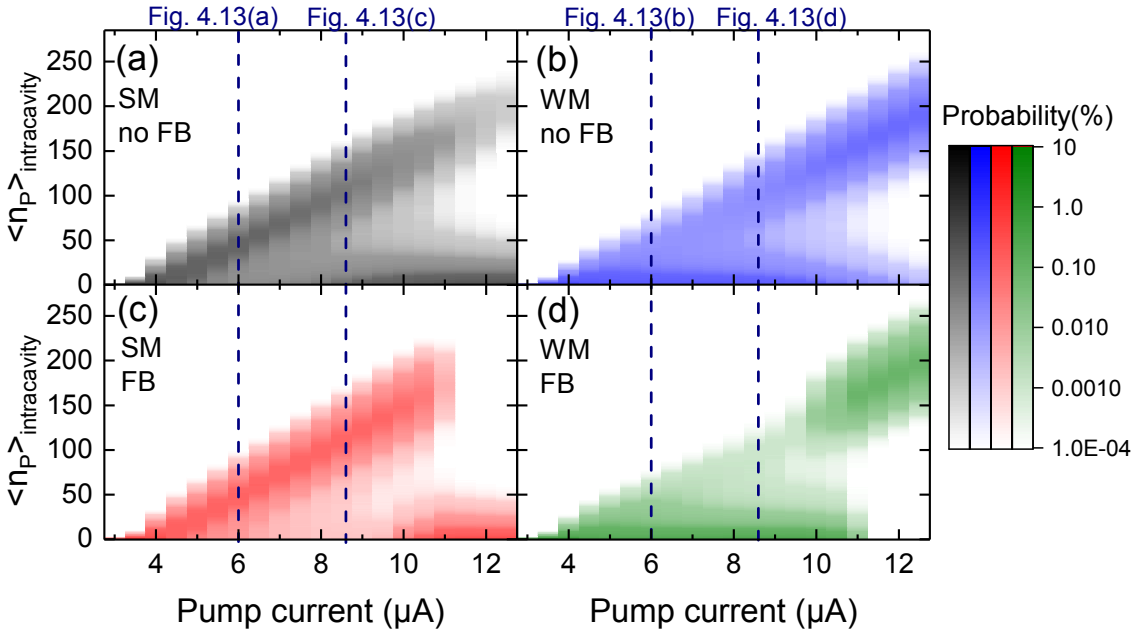

Figure 4.12: Numerical input-output characteristics of 50000 different noise realizations. Panel (a) and (b) depict the SM and WM, respectively, while (c) and (d) show the same scenario in the presence of feedback. Blue vertical lines indicate the pump conditions where the experimental TES measurements are taken to determine the photon-number distribution (see Fig. 4.13).

causes $g^{(2)}(\tau) \to 1$.

Figure 4.12 (c) and (d) depict the behavior of the numerical input-output characteristics in the presence of feedback. Here, the intermediate bimodal region shrinks significantly leading to an abrupt change of roles at the intensity crossing point. One can observe a clear stabilization of both modes beyond the crossing point which leads to lower values of $g^{(2)}(0)$ compared to the scenario without feedback. Accordingly, one can deduce that optical feedback reduces the stochastic switching between both modes of the microlaser. This is also evident in view of Fig. 4.9 which highlights that the less frequent switching only occurs at multiples of the external cavity delay time. From theory such a behavior can be explained in the context of stochastic systems. There, it is known that time-delayed feedback stabilizes oscillations and switching events when coupling back the fluctuations as an external force. Moreover, this also leads to an increased dwell time in one mode when increasing either feedback strength or delay [Sch05].

Taking vertical slices through Fig. 4.12 (marked by blue dashed lines) effectively

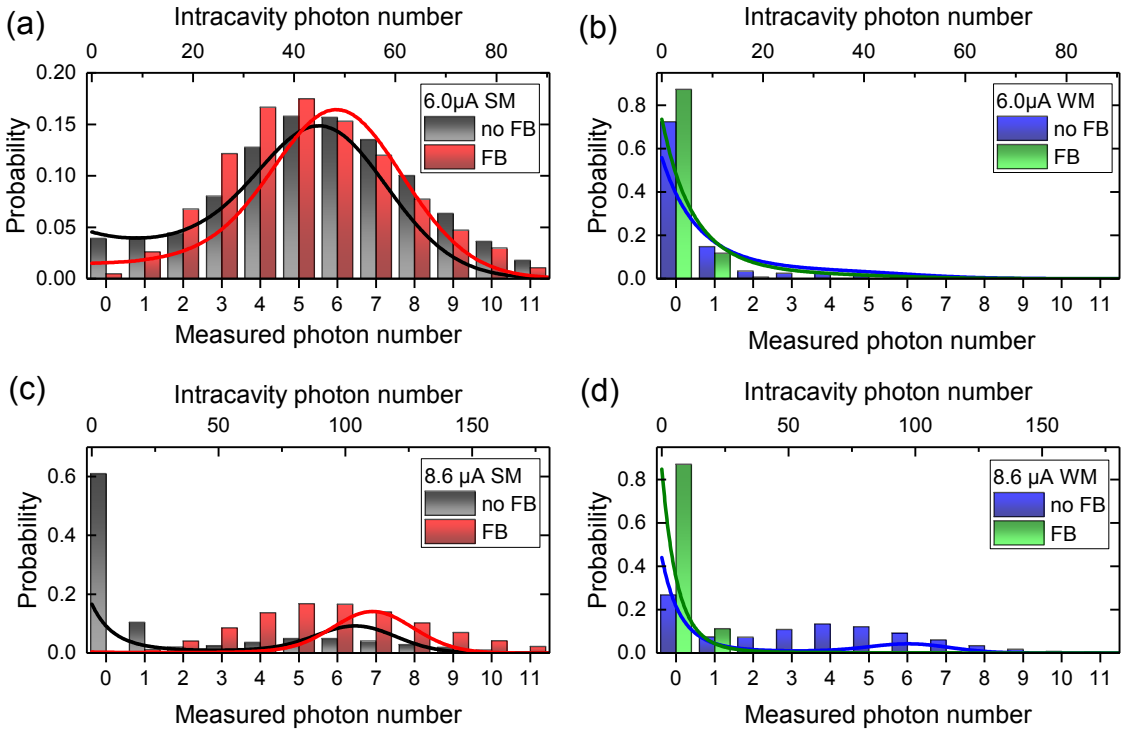

Figure 4.13: Bar histograms of the photon-number distribution measured with the TES. Solid lines refer to the vertical slices of the numerical simulations of Fig. 4.12. The experimental data is using the bottom x-axis while the simulations refer to the top axis.

represents the photon-number distribution (PND) for the chosen pump condition. Accessing the PND is experimentally very demanding but can be achieved using TES detectors. Figure 4.13 displays a juxtaposition of the experimentally measured PND and the numerical simulations for the chosen pump conditions at the marked dashed lines. The experimental TES data is depicted by bar histograms which refer to the bottom x-axis, while the solid lines are the vertical slices through the numerical data of Fig. 4.12. Using a gate of 15 ns in detection one expects on average 10^4 photons during this time window. The detected average photon number is about three orders of magnitude lower as we have to take into account the attenuation losses of the detection path as well as the efficiency of the TES detector. It has to be noted that the latter is determined to be larger than 87 % in the spectral region between 850 and 950 nm [Sch18b]. It has been shown that the important figure of merit $g^{(2)}(0)$ is not altered by attenuation [Sch18a], and thus the underlying photon statistics can still be retrieved from this measurement.

The two selected pump conditions represent two different dynamical scenarios representative of the microlaser dynamics. Figure 4.13 (a) displays the PND of the SM for $I = 6.0\,\mu\text{A}$. Here one finds Poissonian statistics which are overlayed by a significant number of events at $n_\text{P} = 0$. These events are attributed to the portion of the PND that originates from a thermal distribution as previously explained by switching dynamics. Adding optical feedback leads to a suppression of the thermal contribution which effectively increases the coherence time of the SM. Analogously, the WM, which is displayed in panel (b), mainly exhibits thermal behavior with a slight deviation for photon numbers with $n_\text{P} > 3$ being too high for Bose-Einstein statistics. This observation is explained by switching events introducing Poissonian contributions with a higher mean photon number. Again, the switching events are suppressed by optical feedback which is accompanied by a reduction of the high photon number events resulting in a more thermal character of emission.

When increasing the pump current to $I = 8.6\,\mu\text{A}$, as depicted in panels (c) and (d), the suppression of switching events becomes more evident. This bias condition is dominated by switching dynamics so that we find a superposition of thermal and Poissonian statistics. Nevertheless, feedback is still leading to a significant change of the bimodal switching towards stabilization of the SM as the dominating laser mode as well as the WM acting as a thermal emitter. Therefore, we conclude that optical feedback can stabilize the intrinsic switching dynamics of the microlaser and thus can serve as a powerful tool in tailoring the photon statistics of nanophotonic devices.

4.4 Influence of feedback strength

Another key parameter in lasers with delayed feedback is the strength of the fed back intensity. It has to be noted that the alignment of the feedback spot on the micropillar laser facet has significant impact on the feedback strength as explained in section 4.1. Therefore, the aforementioned alignment procedure has to be carried out before each experiment to ensure identical experimental conditions. In our QD micropillar laser, changing the feedback strength with a motorized filter wheel is another control parameter for directly tailoring the switching dynamics. The measurements presented sections 4.1 to 4.3 assumed feedback with the maximally possible coupling strength which is in the following referred to as 100 %. This

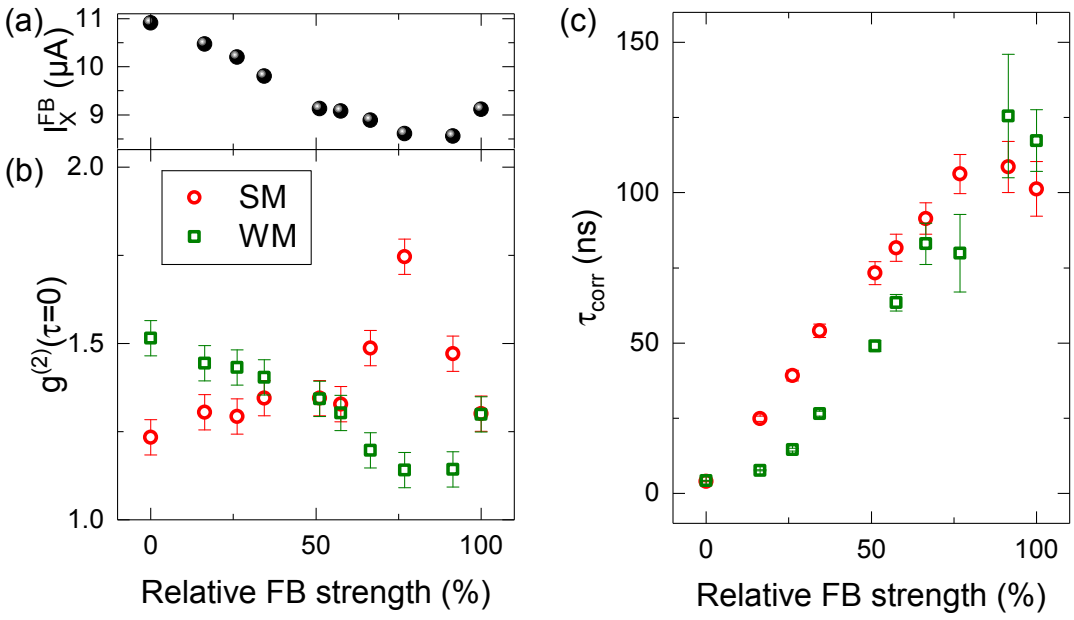

Figure 4.14: (a) Dependence of the intensity crossing point I_X^{FB} on the relative feedback strength. (b) Second-order autocorrelation function at zero delay for the strong and weak mode as a function of the relative feedback strength. (c) Correlation time as a function of feedback strength. Timescales of the decaying revival peaks can be tailored by adjusting the feedback strength.

analysis is again only carried out for microlaser A as microlaser B does not exhibit significant sensitivity to feedback.

Figure 4.14 (a) shows the intensity crossing point I_X^{FB} as a function of the relative feedback strength. Surprisingly, attenuating the feedback strength from the maximum value does not result in a monotonous increase of I_X^{FB}. Instead, we find a minimum at about 91 % relative feedback strength. Consequently, also $g^{(2)}(0)$, which is depicted in panel (b) does not exhibit a monotonous behavior when varying the relative feedback strength. At maximal feedback strength (compare Fig. 4.7) both modes exhibit the same $g^{(2)}(0)$ value while in the limit of zero feedback strength (no feedback) the WM exhibits a larger value than the SM. Increasing the feedback strength from zero, $g^{(2)}(0)$ of the WM first decreases slightly up to a feedback strength of about 50 % where a crossing of $g^{(2)}(0)$ of the two modes occurs. For higher feedback strength $g^{(2)}(0)$ decreases further and finally increases. The SM exhibits an opposite trend, proving again the anti-correlated nature of both modes' dynamics. Particularly, for a feedback strength of 77 % the SM is strongly destabilized resulting in a high $g^{(2)}(0) = 1.75$ while the WM is stabilized yielding

$g^{(2)}(0) = 1.14$. Further increasing the feedback strength towards its maximum again leads to a stabilization of both modes (see Fig. 4.12). It has to be noted that the chosen pump current I_X^{FB} leads to bistable behavior, i.e. the PND is a superposition of a thermal and a Poissonian distribution, both in absence and presence of feedback. Figure 4.14 (c) displays the associated correlation time as a function of feedback strength. The figure shows a monotonous increase and saturation at high feedback strengths. This behavior can be explained by the fact that the increase of the effective pump current $I_{eff} = I + I_X - I_X^{FB}$ saturates as well. Here the term $I_X - I_X^{FB}$ denotes the pump current shift of the regime of switching dynamics.

Overall, varying the feedback strength not only offers a tuning knob to control the stability of both modes and the correlation time. Varying in addition the pump current, it is possible to address a variety of dynamical scenarios ranging from slow to fast dynamics while simultaneously controlling the stable or bistable modal behavior.

4.5 Summary of chapter 4

In this chapter we conducted an extensive and comprehensive study on the effects of incoherent delayed optical feedback on the optical properties of high-β QD microlasers. Gain competition between two orthogonally polarized modes leads to bistable switching dynamics that has also great impact on the input-output characteristics. Different dynamical regimes such as bistability of modes and coherence collapse as well as a change of the dominant lasing mode are observed. Comparing two microlasers, we find different scenarios in the presence of optical feedback. For a laser that exhibits one dominating mode, gain competition is barely affected by optical feedback, while bimodal lasers with intrinsically significant gain competition show a strong change in both optical and dynamical characteristics. In the latter case the pump current needed to address respective features is significantly reduced by optical feedback. Moreover, a direct measurement of the photon-number distribution enabled a stability analysis that proves that feedback can fully destroy the bistability of the two modes by stabilizing one mode depending on the pump strength. Even though its switching dynamics can be stabilized, the mode with lower output intensity depicts highly unstable dynamics that are evident from strong feedback signatures in both optical spectra and the $g^{(2)}(\tau)$-function. Noteworthy, the pinning of switching events to the external cavity round-trip time found in the crosscorre-

lation measurements opens up possibilities for applications. For instance, complex anti-correlated dynamics could potentially be used for all-optical flip-flop memories [Jeo06].

Furthermore, the obtained insights on the sensitivity to optical feedback can be useful for choosing micropillar lasers with interesting dynamics in continuative experiments under optical injection and mutual coupling. For instance, in order to achieve isochronal synchronization of mutually coupled microlasers high sensitivity to feedback and optical injection is crucial [Kle06].

In order to tailor the input-output characteristics as well as dynamical regimes, we have so far discussed the pump current and the feedback strength as tuning knobs. The external cavity round-trip time has been kept at a constant value which is larger than the coherence time of the microlaser. In the following chapter we discuss the interplay between these two timescales and investigate the regime of short cavities.

5 Coherent optical feedback and turn-on dynamics

This chapter addresses the analysis of QD microlasers subject to feedback in the regime of coherent feedback. Therefore, the external cavity length is chosen to be on the same order as the coherence length of the microlaser which is usually a few 10s of centimeters. We do not only study the coherent feedback effects on the spectral characteristics and correlation dynamics of the microlaser but also map the limits of the phase sensitivity expected in this regime. By pulsed optical injection, we determine the relaxation oscillation frequency and the turn-on delay of QD microlasers, which are fundamental dynamical timescales in lasers. These quantities characterize the laser response to small perturbations from its lasing fixed point, and consequently, are vital for the evaluation of the stability properties of a laser [Lin15]. Finally, the effects of feedback on the relaxation oscillation frequency and its damping are studied. Figure 5.1 shows an overview of all the experimental techniques used in this chapter and gives a roadmap of the sections 5.1 to 5.4.

5.1 Input-output and spectral characteristics

First, we investigate the input-output characteristics of the micropillar used for this experiment. This microlaser was fabricated from the same wafer material as microlaser A (see chapter 4). Consequently, this microlaser (which we termed microlaser C in the following) also emits at a fundamental mode energy $E = 1.38\,\mathrm{eV}$ and exhibits a similar quality factor $Q \sim 21000$, which was extracted from the measured linewidth at transparency. Figure 5.2 (a) depicts the input-output characteristics of microlaser C which resembles the one of microlaser B. The SM dominates the gain competition at the lasing threshold ($I \simeq 16\,\mu\mathrm{A}$) while the WM intensity only increases sublinearly around threshold before it decreases for high pump currents

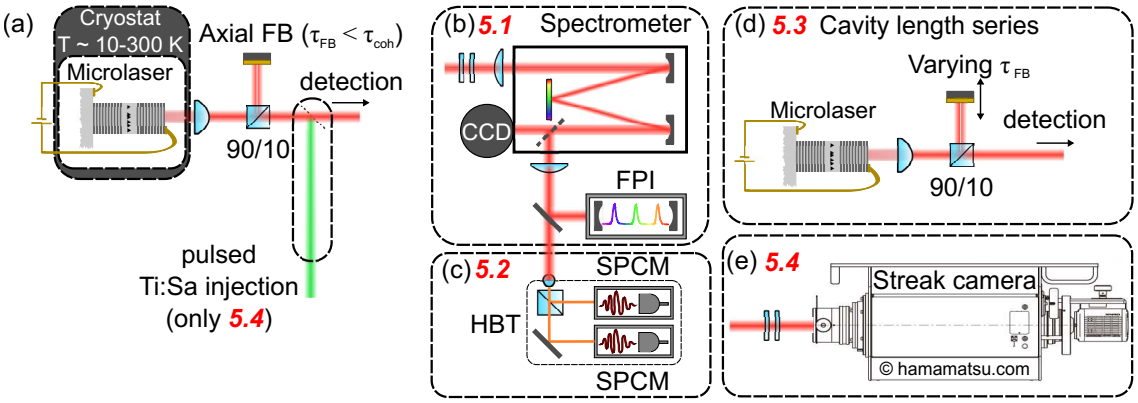

Figure 5.1: Overview of the experimental techniques presented in this chapter: (a) Basic configuration of coherent feedback. (b) Spectrometer with attached CCD used for basic sample characterization in section 5.1. The FPI is used for high-resolution spectra. (c) HBT configuration for second-order autocorrelation measurements in 5.2. (d) Cavity length series with varying τ_{FB} in 5.3. (e) Streak camera setup for synchroscan measurements in 5.4. Here Ti:Sa injection has to be added to the basic configuration.

($I > 20\,\mu\mathrm{A}$). Fitting this data with the semi-classical rate equation model (see A.1) yields a spontaneous emission factor of $\beta = 4 \cdot 10^{-3}$. The full set of fitting parameters can be found in [Kre19] as the investigated micropillar is identical to pillar 2 in the mentioned publication. It has to be noted that the gain compression factors, which were identified to play an important role when analyzing the sensitivity to optical feedback, need to be taken into account here as well. The auto-compression factor of the SM (WM) is 10 (12) $\cdot 10^{-10} \frac{m^2}{AV}$, whereas the cross-compression factor SM $\rightarrow$ WM (WM $\rightarrow$ SM) exhibits a value of 16 (18) $\cdot 10^{-10} \frac{m^2}{AV}$. Even though the values of these parameters are closer to the scenario found in microlaser A, we cannot observe an intensity crossing in microlaser C. This is attributed to the fact that cross-compression factors in microlaser C only differ by 13 % while microlaser A exhibits a difference of 35 %. In the regime of high pump currents the cross-compression factors that describe the intermode kinetics determine the dominant lasing mode [Ley17]. Therefore, only the difference in the cross-compression factors of microlaser A can overcome the higher cavity loss rate of the WM compared to the SM ($\kappa_{\mathrm{WM}} > \kappa_{\mathrm{SM}}$) enabling a crossing in intensity. However, the low values of the cross-compression factors, which are caused by a high mode splitting between strong and weak mode of 73 µeV (compared to 106 µeV for laser A and 33 µeV for laser B), suggest that microlaser C could be sensitive to feedback coupling.

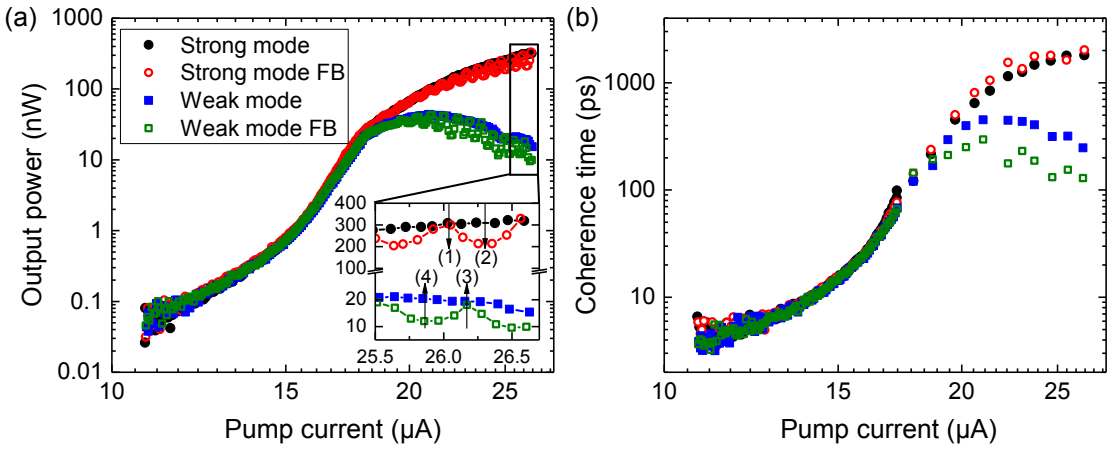

Figure 5.2: (a) Input-output characteristics of microlaser C with a diameter of 5 μm. The inset highlights the output power modulation caused by the short cavity feedback. Arrows indicate four pump conditions labeled (1) to (4) which will be investigated in more detail later. (b) Coherence time of the microlaser extracted from Lorentzian fits of the optical spectrum.

Figure 5.2 (b) displays the coherence time τ_{coh}, which is calculated from the spectral linewidth (see equation 2.11), as a function of the pump current. The coherence time increases from tens of ps below threshold to several ns in the lasing regime, with a pump current dependence that resembles the input-output curve. Consequently, τ_{coh} becomes an important figure of merit when trying to apply coherent feedback. For the experimental results shown in Fig. 5.2 $\tau_{\mathrm{FB}} = 0.97\,\mathrm{ns}$ was chosen, which is below the maximum coherence time of the laser but well above the coherence time close to threshold. This way one can experimentally determine the limit of coherent feedback effects.

Adding coherent feedback from this short cavity leads to a modulation of the emission intensity due to interferences between the internal and external cavity modes. This effect is highlighted in the inset of Fig. 5.2 (a) and can be explained by the phase-coherent interaction between the solitary laser mode and the ECMs. It is in contrast to previous chapter, where we found incoherent coupling to the ECMs. Moreover, the separation $\Delta\nu_{\mathrm{ECM}}$ of the ECMs, which are distributed as an equidistant comb of modes, is the inverse of the external cavity round-trip time, and one obtains $\Delta\nu_{\mathrm{ECM}} = 1.03\,\mathrm{GHz}$. Taking into account that the spectral linewidth above threshold is well below this value (few 100s of MHz), the fundamental mode can only interact with 1 or 2 ECMs.

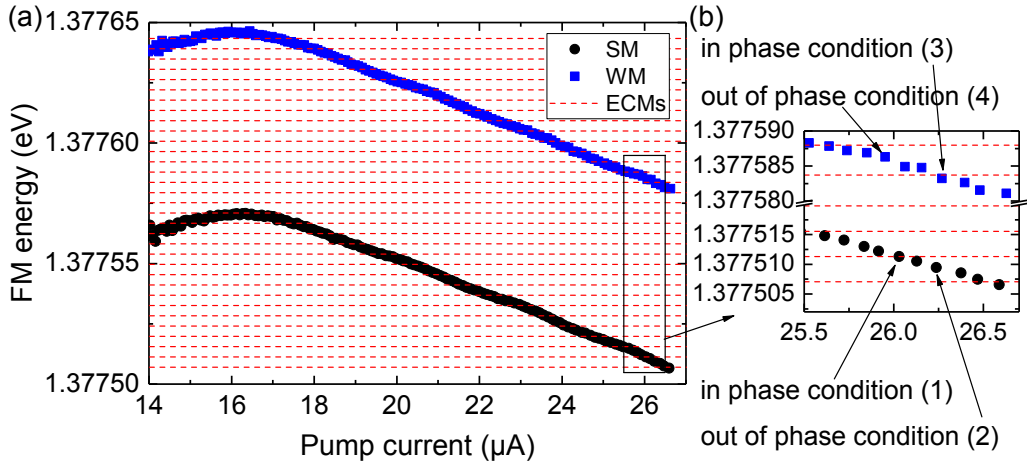

Figure 5.3: (a) Pump-dependence of the fundamental mode energy. The spectral position of the ECMs is marked by red dashed lines. (b) Zoom-in of the pump current region that is displayed in the inset of Fig. 5.2 (a) visualizing the marked in and out of phase conditions.

The reason for the intensity modulation observed in Fig. 5.2 (a) is highlighted in Fig. 5.3. When increasing the pump current, the modes shift to higher energies via the plasma effect as increasing carrier density leads to a decrease in refractive index [Ben90]. For higher pump currents both modes finally shift to lower energies as sample heating leads to an expansion of the resonator. This mode shift causes both SM and WM to cross several ECMs. Here each crossing is related to one period of the intensity modulation in the input-output curve (see Fig. 5.2 (a)). When the SM or WM coincides spectrally with an ECM we refer to the *in phase* condition, whereas the situation in which the SM or WM is spectrally in between two ECMs is defined as the *out of phase* condition (see Fig. 5.3 (b)).

The intensity modulation is observed above threshold for $I \gtrsim 19\,\mu\text{A}$ when both modes start diverging in intensity. Here the coherence time of both modes is $\tau_{\text{coh}} = 0.32\,\text{ns}$ which is smaller than $\tau_{\text{FB}} = 0.97\,\text{ns}$. The WM only moderately increases in coherence time to $\tau_{\text{coh}} = 0.45\,\text{ns}$ and eventually decreases for the highest pump currents (see Fig. 5.2 (b)). The SM, on the other hand, significantly increases in coherence time to $\tau_{\text{coh}} = 1.90\,\text{ns}$ which is greater than the external cavity round-trip time. This means that one has to study the limits of coherent effects in more detail, which is done by a cavity length series in section 5.3. In Fig. 5.2 (a) we observe a current modulation if the condition $\tau_{\text{FB}} \lesssim 3\tau_{\text{coh}}$ is fulfilled which means that the coherence time is not a strict limitation to observe coherent feedback effects.

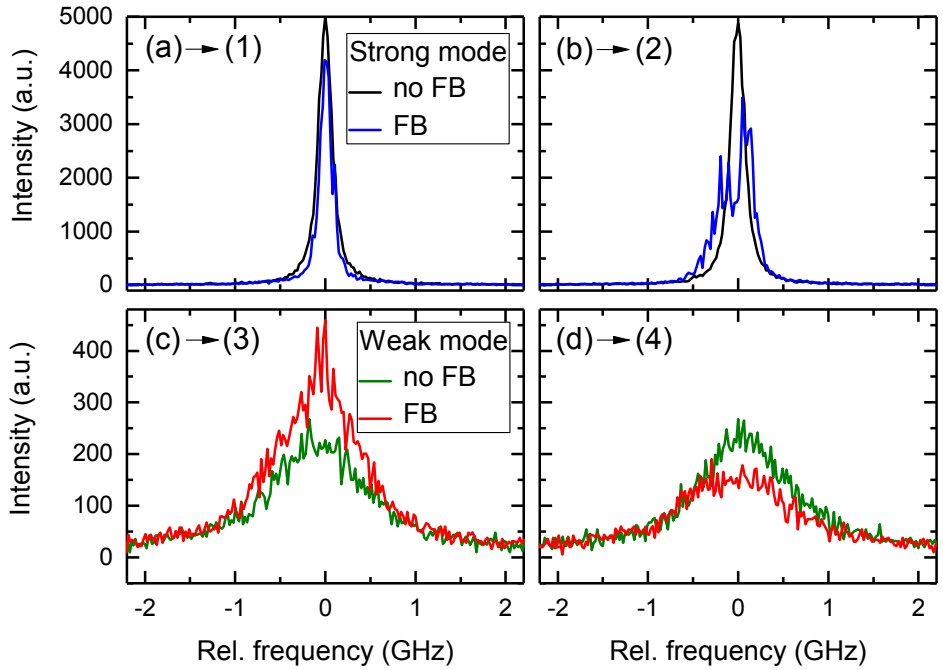

Figure 5.4: FPI spectra of the SM being (a) in phase and (b) out of phase with the ECMs of the external cavity. Accordingly, (c) and (d) depict respective cases of the WM. Panels (a)-(d) correspond to the previously mentioned scenarios (1)-(4).

Figure 5.4 displays high resolution FPI spectra taken for the two modes in *in phase* and *out of phase* condition. For comparison the solitary spectra where feedback is absent are depicted as well. When the fundamental modes are in phase with an ECM (see panels (a) and (c)) one observes a reduction in linewidth and consequently an increase in coherence time. τ_{coh} increases from 1.9 ns to 2.7 ns for the SM, while the WM shows an increase from 0.25 ns to 0.32 ns. In case of the SM this increased coherence time is equivalent to a linewidth of 116 MHz which is very close to the resolution limit of the FPI of 100 MHz. Thus, the increase in coherence might be underestimated as smaller linewidths cannot be resolved with the used FPI. For the out of phase conditions (panels (b) and (d)) we find broadened spectra that can be explained by destructive phase-interference between the fundamental mode and the ECMs [Lan80]. If the lasing mode is spectrally in between two ECMs this causes a phase instability. The detuning of the ECMs from the solitary frequency clarifies the lowered averaged intensity in the input-output characteristics recorded on the CCD.

5.2 Phase dependence of correlation dynamics

After discussing the enhancement and decrease of the coherence time depending on the feedback phase, we need to analyze its impact on the switching dynamics of the delay-coupled system. Therefore, the second-order autocorrelation function is again used as a tool to determine the stability of both modes. The SM of microlaser C exhibits $g^{(2)}(\tau) \simeq 1$ for all pump currents $I > 20\,\mu\text{A}$ which is similar to the behavior observed in microlaser B (compare Fig. 4.10). As already explained in the previous chapter, the strong divergence in intensity of SM and WM prevents competing mode dynamics that would cause bunching in both modes as well as revival peaks. Consequently, for microlaser C only WM bunching can be used as a monitor of mode stability. The WM is mainly a thermal emitter with short switching periods that result in lasing. Thus, measuring $g^{(2)}(\tau)$ of this mode gives insight into the stability with respect to switching events by analyzing the value at $\tau = 0$. Similarly, it reveals the switching timescales by analyzing its temporal decay.

Figure 5.5 depicts $g^{(2)}(\tau)$ for four different pump currents in the range from 25.9 to 26.2 µA as highlighted by the insets showing the same pump region as Fig. 5.2 (a). The solitary WM exhibits $g^{(2)}(0) = 1.53 \pm 0.02$ over the whole pump regime. Taking into account that the correlation time $\tau_{\text{corr}} = (0.95 \pm 0.05)\,\text{ns}$ is significantly greater than the coherence time $\tau_{\text{coh}} = (0.26 \pm 0.01)\,\text{ns}$, this bunching is not attributed to thermal emission, but switching dynamics as explained in previous chapter.

The external cavity length for this experiment is adjusted so that SM and WM have different feedback-phase conditions for a fixed pump condition. This means that their phase relation is neither in phase ($\Delta\theta_{\text{SM-WM}} = 0$) nor anti-phase ($\Delta\theta_{\text{SM-WM}} = \pi$). Figure 5.5 (a) displays a scenario where the WM is out of phase while the SM is not in phase. In contrast, in panel (b) both modes are out of phase. In both cases an increase in $g^{(2)}(\tau = 0)$ is found which is related to a faster switching of the WM to the lasing state. At the same time the correlation times increase from $\tau_{\text{corr}} = (1.08 \pm 0.05)\,\text{ns}$ to $\tau_{\text{corr}} = (1.23 \pm 0.05)\,\text{ns}$ which indicates longer dwell times of the WM in the lasing state. Panels (c) and (d) focus on the cases where either the SM or WM is in phase. Accordingly, their counterpart mode is out of phase as previously explained by choice of the external cavity length. In both scenarios we find a significant decrease in bunching. This is explained by the fact that if one mode is stabilized by constructive interference with one ECM, which is

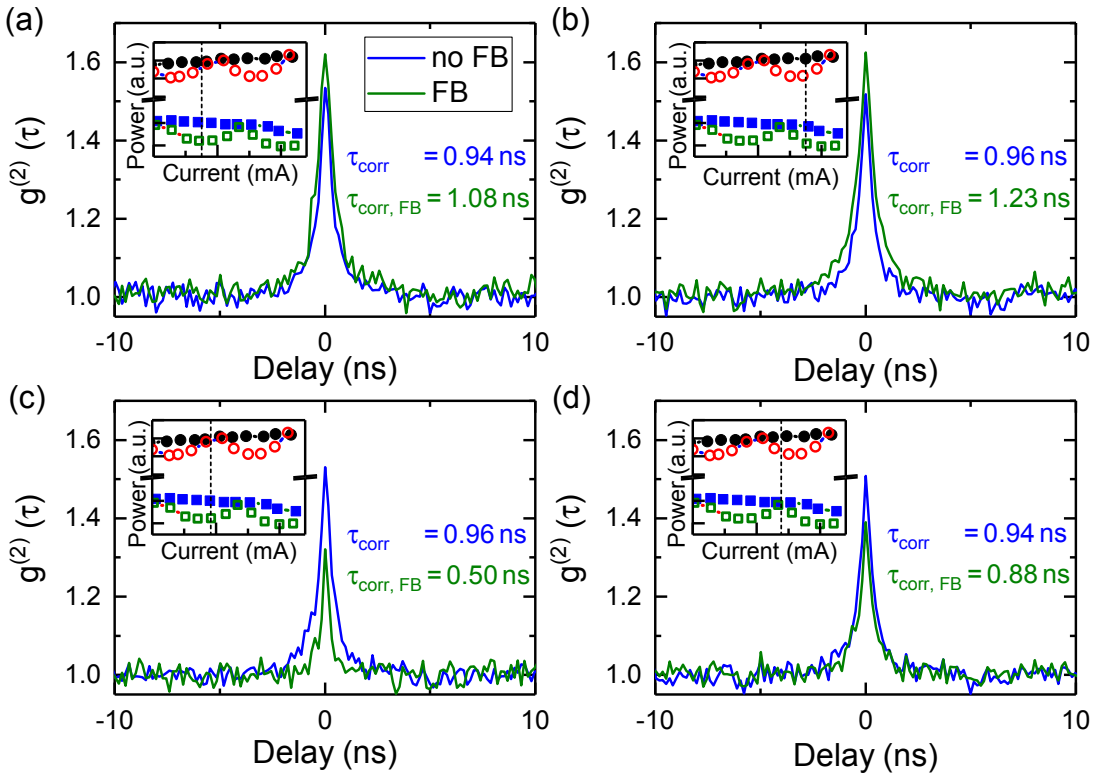

Figure 5.5: Measurements of the second-order autocorrelation function for various phase conditions of WM. Insets depict the region of interest along the input-output curve. A dashed line is indicating the used pump condition from which we deduce the feedback phase of both modes. (a) WM is out of phase while SM is not in phase. (b) Both modes are not in phase. (c) Strong mode is in phase while WM is not. (d) WM is in phase while SM is not.

already evident from the linewidth narrowing recorded by the FPI, this leads to a suppression of the switching dynamics. Here a decrease of the correlation times to $\tau_{\mathrm{corr}} = (0.50 \pm 0.05)\,\mathrm{ns}$ and $\tau_{\mathrm{corr}} = (0.88 \pm 0.05)\,\mathrm{ns}$ is detected. The stronger decrease for the SM being in phase with an ECM is also consistent with the FPI spectra and gives a hint that the full linewidth reduction was indeed masked by the spectral resolution of the FPI.

From these results one can conclude that not only the optical spectra but also the switching dynamics are highly sensitive to the feedback phase in the regime of coherent feedback. Furthermore, the chosen arbitrary phase relations of the feedback phase highlight that the phase of both modes has to be examined when trying to enhance or suppress the dynamics. An increase in $g^{(2)}(\tau = 0)$ and τ_{corr} arises only

when none of the solitary modes is in phase with an ECM (Figs. 5.5 (a) and (b)), whereas a decrease of those parameters originates from at least one mode being in phase with an ECM. This explanation can also be applied to the incoherent feedback regime. There the ECMs lie so densely that we can assume $\Delta\theta_{\text{SM-WM}} \to 0$. Consequently, both modes can be stabilized in their role as a thermal emitter or laser, respectively, as we discussed in detail for microlaser A. This behavior is not universal for incoherent feedback though, as we found pump current conditions that favored one mode, while the counterpart mode was destabilized, which we attribute to cross-gain compression. In the following, we focus on the limits of the phase sensitivity and investigate the transition from coherent to incoherent feedback in detail.

5.3 Limits of phase sensitivity

The main characteristic of the short cavity or coherent feedback regime is given by the optical spectrum and dynamics being sensitive to the optical feedback phase, which contrasts with the phase insensitive long cavity or incoherent feedback regime. Before investigating the boundaries between those regimes, we firstly examine how optical spectra are modified by feedback in both scenarios. It has to be noted that for this comparison the feedback phase ϕ was not tuned by slightly varying the pump current as in the previous experiments but instead by placing the feedback mirror on a piezo stage. This way one is able to change the external cavity length with a precision of about 20 nm which translates to a feedback phase variation of 8°.

Figure 5.6 displays the comparison of high-resolution optical FPI spectra for (a) the short cavity regime ($\tau_{\text{FB}} = 0.83$ ns) and (b) the long cavity regime ($\tau_{\text{FB}} = 4.67$ ns). As a reference the solitary condition in absence of feedback is shown in both cases as well. In the short cavity regime we again find a narrowing of the linewidth from 256 MHz to 141 MHz and an increase in intensity by 10 % when the mode is in phase with an ECM . As a guide to the eye these spectral positions of the ECMs are depicted for both the in and out of phase scenario. For the short cavity with $\tau_{\text{FB}} = 0.83$ ns we expect a mode separation of the ECMs $\Delta\nu_{\text{ECM}} = 1.2$ GHz. It has to be noted that in Fig. 5.6 only relative frequencies are shown. In the experiments presented in sections 5.1 and 5.2 the emission line shifts in frequency for different pump currents while the ECMs are at constant spectral positions (see Fig. 5.3).

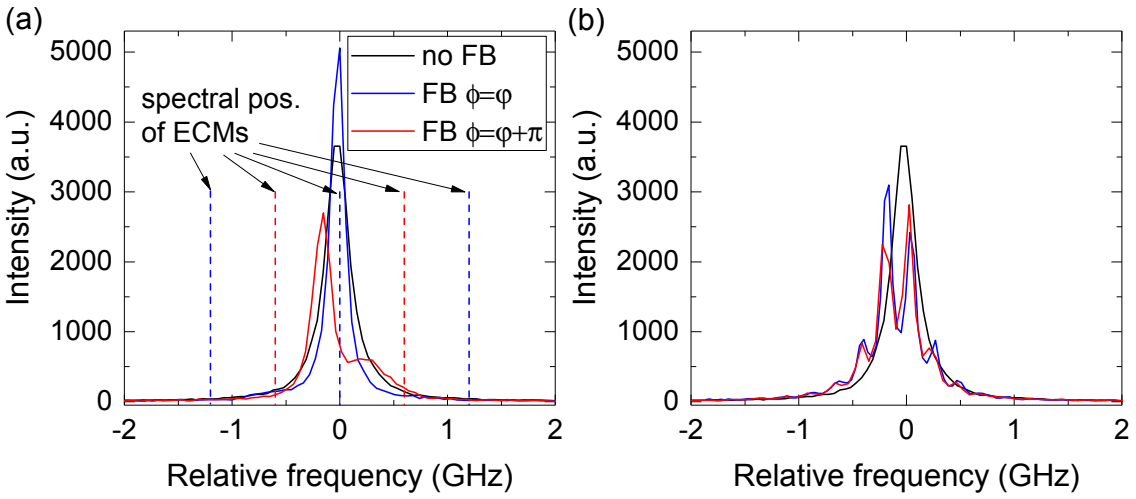

Figure 5.6: FPI spectra of the SM at a pump current of $I = 23\,\mu A$ both in presence and absence of optical feedback. Panel (a) depicts a short cavity with $\tau_{FB} = 0.83\,ns$ while (b) displays a long cavity with $\tau_{FB} = 4.67\,ns$. The feedback phase ϕ is controlled precisely by a piezo stage tuning the cavity length. In panel (a) the spectral position of the ECMs are marked for the in phase and out of phase conditions by blue and red dashed lines, respectively.

When changing the external cavity length, instead the ECMs shift in frequency. In the in-phase condition the fundamental mode only interacts with one ECM. In contrast, in the out of phase condition the laser mode is located directly in between two ECMs. This results in a reduced output power as well as an instability causing the mode to oscillate with two frequency components (see Fig. 5.6 (a)). Interestingly, the two emission frequencies in this out of phase condition do not coincide with the ECMs and thus cannot be used to determine τ_{FB}.

In the long cavity regime on the other hand, the SM interacts with up to 6 ECMs for the chosen cavity length (see Fig. 5.6 (b)). Here it is delicate to define an in phase or out of phase condition as changing the feedback phase does neither influence the output power of the laser nor its spectral linewidth. Nevertheless, we can still observe a shifting envelope as we change the external cavity length (or e.g. the temperature of the microlaser). Consequently, we detect the convolution of the solitary laser line with the comb of modes created by the external cavity. In this case the peaks of the modulated mode intensity coincide with the ECMs (that are not shown here to not make the figure too crowded). Therefore, the spectral distance of those peaks is $\Delta\nu_{ECM} = 0.21\,GHz$, which is the inverse of τ_{FB}. In the long cavity

regime the feedback phase switches the intensity of each ECM contribution while keeping the sum of the intensities constant.

Besides the change in linewidth, the above spectral analysis suggests that the visibility of the output power amplitude modulation (AM) is a good figure of merit to distinguish between the two regimes. In order to determine the limit of the phase sensitivity, we analyze the AM as a function of the external cavity round-trip time. For this experiment we examine AMs by precisely varying the pump current as previously done in sections 5.1 and 5.2. This approach is fast and easily reproducible (always accounting for possible hysteresis). Meanwhile, the piezo stage that is used to tune the external cavity length, is driven with an open-loop piezo which would require the use of an additional laser as a reference source. Furthermore, pump current tuning is available in microlasers as well as in possible future applications such as integrated photonics. In the latter case varying the pump current is naturally accessible while adjusting the external cavity length on chip is technologically demanding.

For the analysis of the experimental data one has to ensure a proper sampling rate along the input-output curve. In order to resolve the AM, the sampling rate has to be enhanced when increasing the external cavity round-trip time which is explained by the decrease of $\Delta\nu_{\mathrm{ECM}}$. This issue is highlighted in Fig. 5.7 for an external cavity round-trip time $\tau_{\mathrm{FB}} = 3.1\,\mathrm{ns}$. To determine the critical sampling rate, we apply the Nyquist-Shannon sampling theorem [Sha48] stating the sampling frequency f_{s} has to be at least twice the maximum frequency f_{max} of the investigated signal. For the investigated external cavity length we obtain a critical sampling rate of 20 steps per µA. Consequently, panel (a), which depicts a current sweep with 10 steps per µA, shows aliasing and the modulation is masked. When increasing the sampling rate to the value (which is also used in the following experiment) of 50 steps per µA, the sinusoidal AM is recovered.

Figure 5.8 (a) displays the normalized AM as a function of the external cavity round-trip time. This curve exhibits an exponential decay which resembles the fringe contrast amplitude of a Michelson interferometer, which is a commonly used tool to determine the coherence time of a laser. In analogy to the mentioned fringe contrast, the AM does not immediately drop to zero when the threshold $\tau_{\mathrm{FB}} > \tau_{\mathrm{coh}}$ is reached. Instead, one finds an exponential decay for both SM and WM. Interestingly, the decay constant of both modes is similar even though their coherence time differ

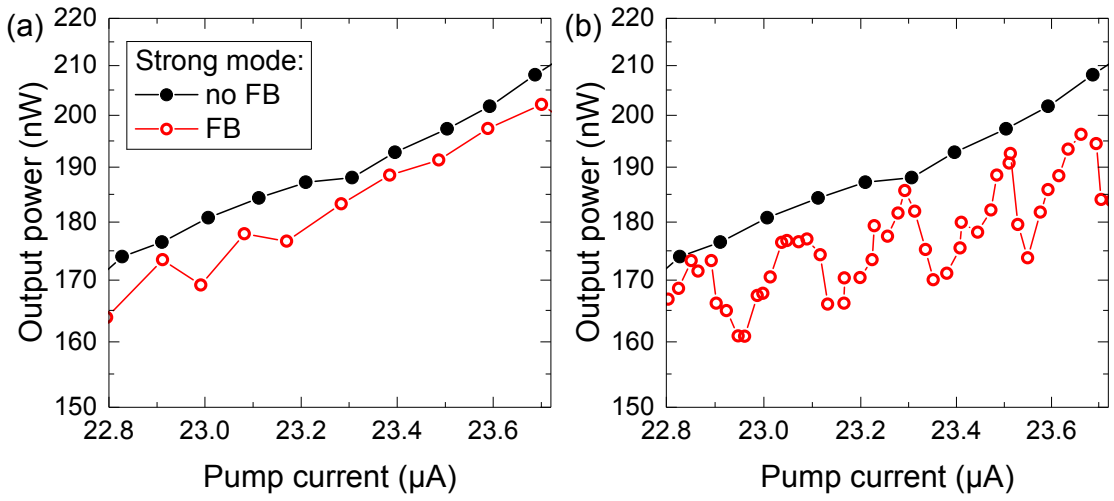

Figure 5.7: Zoom of the SM input-output characteristic at $\tau_{\mathrm{FB}} = 3.1\,\mathrm{ns}$. (a) Aliasing of the output modulation is evident when the sampling rate is smaller 20 steps per μA (here 10 steps per μA). (b) Proper sampling of the modulation at a rate of 50 steps per μA.

significantly ($\tau_{\mathrm{coh,\,WM}} = 0.54\,\mathrm{ns} < \tau_{\mathrm{coh,\,SM}} = 1.90\,\mathrm{ns}$). We attribute this observation to mode switching. When the WM switches to the lasing state its coherence time becomes similar to the one of the SM. The averaged measurement of the optical spectrum still detects a significantly lower coherence time as the WM resides most of the time in the thermal state. Yet, the coherent interaction of the multiphoton pulses with the ECMs is still present leading to an amplitude modulation throughout the whole input-output curve above threshold as already identified in Fig. 5.2 (a). Moreover, it has to be considered that a strong modification of the mode with highest coherence (SM) drives the amplitude of its counterpart due to gain clamping.

Another interesting figure of merit when describing the transition from the short to long cavity regime is the phase difference of the SM and WM amplitude modulation $\Delta\theta_{\mathrm{SM\text{-}WM}} = \phi_{\mathrm{SM}} - \phi_{\mathrm{WM}}$, where ϕ_{SM} and ϕ_{WM} denote the absolute feedback phase of the SM and WM, respectively. Figure 5.8 (b) depicts this quantity when modifying the external cavity length. In section 5.2 we used a condition where $\Delta\theta_{\mathrm{SM\text{-}WM}}$ is neither 0 nor π which was beneficial when trying to independently stabilize the SM or WM. In order to understand the evolution of $\Delta\theta_{\mathrm{SM\text{-}WM}}$ with increasing external cavity length, we developed the following empirical equation:

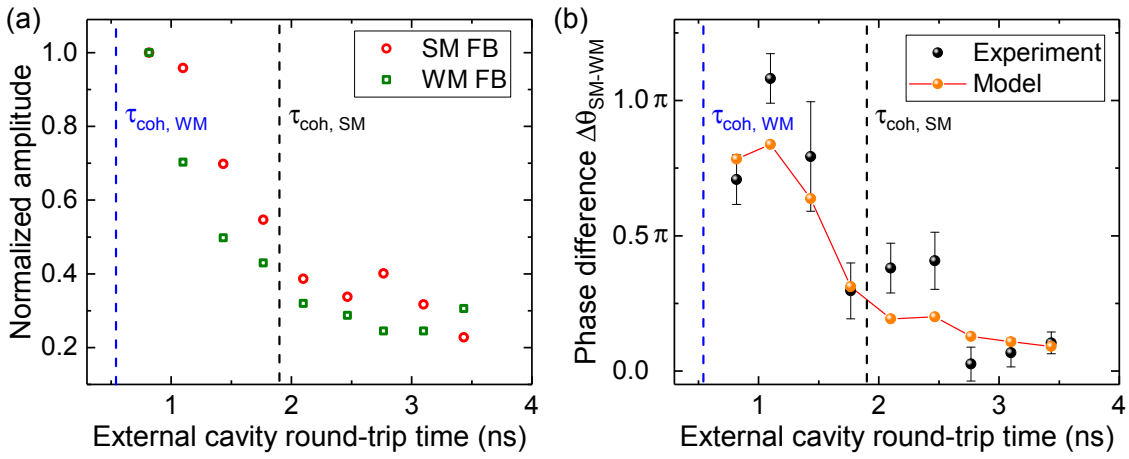

Figure 5.8: External cavity length series. (a) Amplitude modulation of both SM and WM as a function of the cavity round-trip time. (b) Phase difference of the amplitude modulation of both modes depicted as black bullets. An empirical model is displayed in orange. The coherence times of both modes are indicated by dashed black and blue lines, respectively.

$$\Delta\theta_{\text{SM-WM}} = mod\left[2\pi * \frac{1}{n}\sum_{\text{j}=1}^{n} mod\left[\Delta\nu_{\text{S-W}}(I_{\text{j}}),\Delta\nu_{\text{ECM}}\right],2\pi\right] \cdot \frac{1}{N}, \tag{5.1}$$

where $\Delta\nu_{\text{S-W}}(I_{\text{j}})$ is the current dependent spectral detuning of both modes above threshold and N is the amount of ECMs that are able to match within the full-width half maximum linewidth of the WM. It has to be noted that the model can only be applied to cavity lengths examined in the measurement where the current dependent spectral detuning was analyzed. To understand the reasoning behind this equation, we consider the linewidth of the solitary SM $\Delta\nu_{\text{SM}} = 174\,\text{MHz}$ and WM $\Delta\nu_{\text{WM}} = 1.21\,\text{GHz}$. When taking into account the investigated range of external cavity lengths $\tau_{\text{ext,min}} = 0.82\,\text{ns}$ to $\tau_{\text{ext,max}} = 3.4\,\text{ns}$, we find that the SM can only interact with one ECM within its linewidth, while the WM is able to couple to multiple modes as $\Delta\nu_{\text{ECM}}$ ranging from 1.22 GHz to 294 MHz. Consequently, the value of the phase difference is reduced the more ECMs are within the linewidth of the WM which is accounted for by the $\frac{1}{N}$ term. This means that non-zero values $\Delta\theta_{\text{SM-WM}}$ are more frequent for short cavities. For the shown microlaser we even find an anti-phase relation here. When increasing the external cavity length ($\tau_{\text{ext}} \gg \tau_{\text{coh}}$) the phase difference approaches zero as $N \gg 2$, see e.g. the scenario depicted in Fig. 5.6 (b). Thus, numerical simulations typically set any values related to the feedback

phase as constant in the long cavity regime [Oht13]. The variation of the external cavity length can be exploited to precisely control the phase difference of two modes. However, the limit of $\Delta\theta_{\text{SM-WM}} = 0$ can only be reached consistently in the long cavity regime. Moreover, coherent coupling as quantified by the AM is significantly reduced if more than one ECM spectrally matches the linewidth of either fundamental mode. This is attributed to spontaneous emission noise causing the lasing mode to jump between the ECMs [Mør90] as described already for conventional feedback-coupled semiconductor lasers in feedback regime II (compare section 2.5).

5.4 Relaxation oscillation measurements

The relaxation oscillation frequency $f_{\text{RO}} = \frac{1}{\tau_{\text{RO}}}$ is a crucial parameter for the investigation of feedback dynamics. Especially, the interplay between the relaxation oscillation timescale τ_{RO} and the external cavity round-trip time τ_{FB} influences the dynamics [Por14]. For very short cavities with $\tau_{\text{FB}} < \tau_{\text{RO}}$ complex dynamics such as regular pulse packages have been observed [Hei01]. In this regime the timescales of the dynamics are dominated by the external cavity round-trip time rather than by the relaxation oscillations. The latter timescale is usually the prevalent one in the long cavity regime. It has to be noted that in literature one often finds the short cavity regime being related to $\tau_{\text{FB}} < \tau_{\text{RO}}$ and the long cavity regime being defined by $\tau_{\text{FB}} > \tau_{\text{RO}}$ [Sci15]. This distinction is inspired by the long coherence lengths of classical semiconductor lasers (several 10s of meters). Spurious reflections that naturally lead to feedback in applications (e.g. fiber-coupling a semiconductor laser on a butterfly mount) are therefore often found to be in the coherent regime causing the differentiation to be made within this region. To clarify the issue in this work the different cavity length regimes are defined as follows:

- $\tau_{\text{FB}} < \tau_{\text{RO}}$: very short cavity regime
- $\tau_{\text{RO}} < \tau_{\text{FB}} < \tau_{\text{coh}}$: short cavity regime
- $\tau_{\text{coh}} < \tau_{\text{FB}}$: long cavity regime.

In classical semiconductor lasers f_{RO} is commonly determined by acquiring the relative intensity noise spectrum with a photo diode and an electrical spectrum analyzer [Kuc93]. This method fails at the light levels well below 1 µW, like those

present in the investigated QD microlasers. To overcome this difficulty, we developed a technique where one injects picosecond optical pulses from a Ti:Sa laser to off-resonantly excite the electrically pre-biased microlaser, which is similar to the approach of Schneider et al. [Sch94]. The optical pulses are injected into the first reflectivity-minimum sideband of the DBR mirror ($\sim$849 nm). This off-resonant excitation scheme utilizes low pulse intensities so that the system is not effectively pumped. The injection pulse effectively serves as a perturbation that pushes the microlaser out of its stable CW operation. It has to be highlighted that the microlaser does not instantaneously follow the external force of the optical pulse. The time delay between optical pulse and the response of the laser is called turn-on delay τ_{TO}. Subsequently, the laser relaxes back to this stable operating condition after the pulse duration. This damped oscillatory process is called relaxation oscillation (RO). These ROs also naturally occur, e.g. when the pump power fluctuates or just through spontaneous emission events [Pet86], as the oscillations are caused by the coupling between the fluctuations of the intracavity photon number and the density of charge carriers [Coh88]. Therefore, knowing the frequency f_{RO} and its damping rate give insight into the stability of a laser as well as the dynamical response in the presence of optical feedback or injection, which can be considered external perturbations.

Figure 5.9 depicts the results of determining τ_{TO} and f_{RO} with the streak camera. As shown in panels (a) and (c), two different time ranges are used to analyze these figures of merit. We choose trace lengths of 200 ps for the turn-on delay as high temporal resolution is needed here. The relaxation oscillation timescale on the other hand exceeds this value. Therefore, longer traces of 1200 ps are chosen. In order to correctly determine the delay between the Ti:Sa pulse and the microlaser response, we detect both signals simultaneously on the streak camera with 5 ps time resolution. Here the grating spectrometer (situated in front of the streak camera) enables the spatial separation of the two signals. By determining the time difference between the maximum of the Ti:Sa pulse and the microlaser response, one yields τ_{TO}. Panel (b) displays the result of the evaluated turn-on delay as a function of the pump current. We observe a decrease of the delay with increasing pump current down to 36 ps. In order to find possible fundamental limitations for this non-vanishing timescale, a pillar diameter series is performed later in this chapter.

The relaxation oscillation frequency is calculated from the inverse time difference

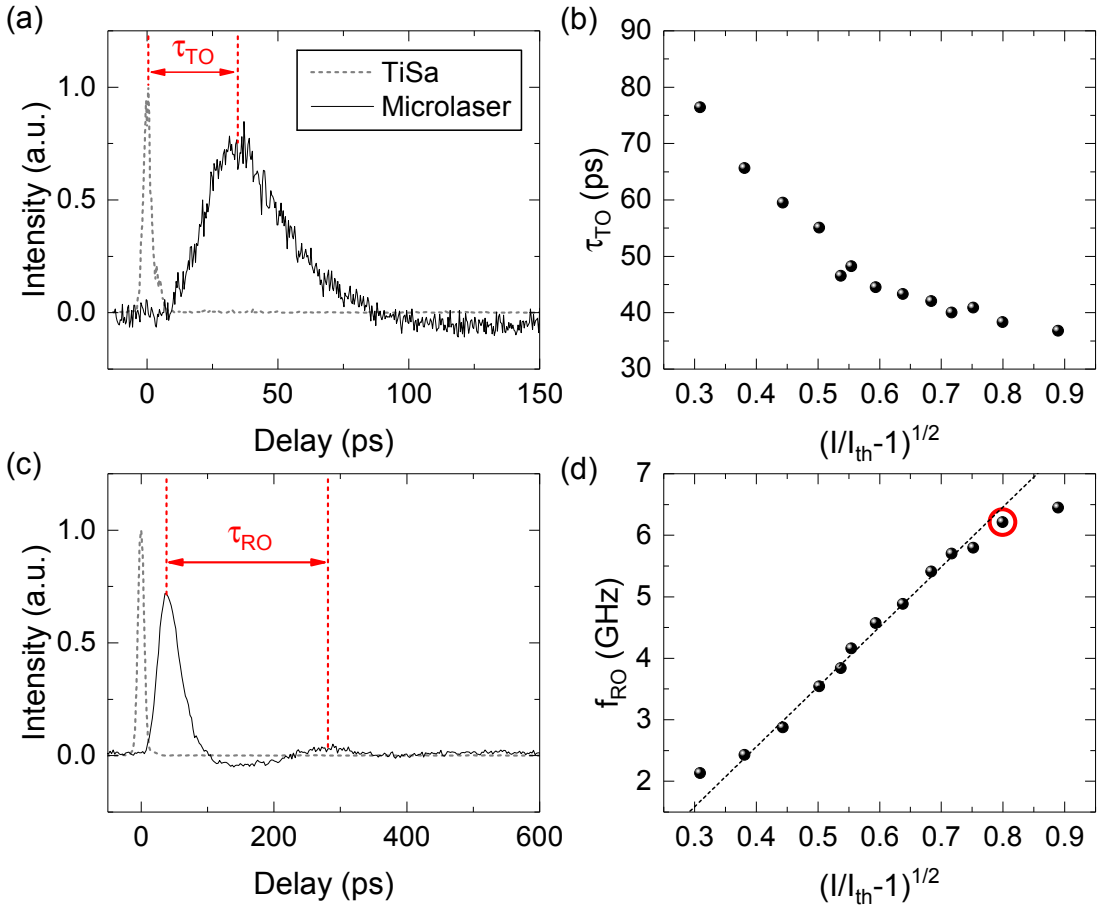

Figure 5.9: (a) and (c) depict exemplary streak camera traces in different time ranges. The high-resolution time range as seen in panel (a) is used to determine τ_{TO} while (c) longer traces are needed to determine τ_{RO}. Panels (b) and (d) depict the evaluated result for microlaser C for various pump conditions. The data point used for future feedback experiments (see Fig. 5.12) is marked with a red circle.

of the first and second maximum of the micropillar response. Panel (d) depicts f_{RO} as a function of the excitation current. f_{RO} is found to be proportional to $(I/I_{\mathrm{th}} - 1)^{1/2}$ [Ern10]. Therefore, this term is also chosen as the x-axis scaling to analyze the dependence. It has to be noted that this relation is only accurate for an ideal single-mode semiconductor laser. In the experiment one finds deviations for low pump currents close to threshold as the broad linewidth and low side mode suppression ratio are in contrast to the previously mentioned assumption that the laser spectrum comprises only a single frequency [Ext92]. For higher pump currents we be attribute the discrepancies to sample heating which is shifting the QD gain

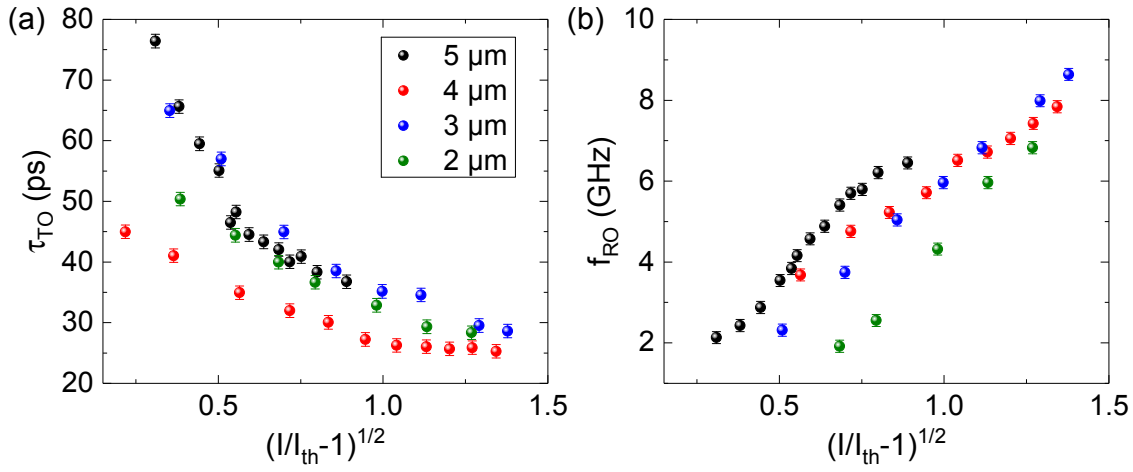

Figure 5.10: (a) Turn-on delay τ_{TO} and (b) relaxation oscillation frequency f_{RO} as a function of the pump current. The graphs highlight the comparison for various diameters.

to lower energies [Bjö05]. This issue is highlighted in panel (d) by a linear fit of the all but the two outermost data points in the low and high pump regime each. Noteworthy, the relaxation oscillation frequencies we determined for microlaser C are still considerably lower than the ones found in single cavity VCSELs emitting in the near infrared. The lower relaxation oscillation frequencies in the investigated microlasers has the following reasons: In our experiments we pump 120 microlasers jointly via one common gold contact which leads to a worse RC-constant. Moreover, in VCSELs further techniques have been applied to increase the modulation bandwidth such as electrical contacts in ground-signal-ground (GSG) configuration, ideal number of quantum wells or dots and optimized doping profiles of the DBRs. That is why in VCSELs e.g. bandwidths of 35 GHz have been reported [Hag18]. This work on VCSELs also highlights a diameter dependency of the modulation bandwidth. Thus, we compare the pump dependence of both the turn-on delay and the relaxation oscillation frequency for several micropillar diameters.

Figure 5.10 depicts these two figures of merit for microlasers of the following diameters: 5 µm (microlaser C), 4 µm, 3 µm and 2 µm. The microlaser with a diameter of 4 µm consistently depicts the lowest values of τ_{TO}. We find this value to saturate around $\tau_{TO} \sim 25$ ps. This non-vanishing turn-on delay has been previously reported in macroscopic QD based semiconductor lasers [Sok12]. While quantum well-based lasers depict a hyperbolical decay of τ_{TO} to zero with increasing pump current, QD

based devices show a turn-on that cannot go faster than a fixed value which is independent of the pump current. This behavior limits the modulation bandwidth of QD-lasers and can be explained by the fact that charge carriers are not instantaneously captured by the QD. Here the scattering from the wetting layer into the QD has to be taken into account. For the capturing time the authors of [Sok12] assume a typical value of 10 ps which is on the same order of magnitude as the value of τ_{TO} found for the 4 µm microlaser.

As previously discussed, the micropillar with 4 µm diameter exhibits the best performance with respect to τ_{TO} while also showing relaxation oscillation frequencies of up to 7.8 GHz. In contrast, the microlaser with 5 µm diameter already saturates around $f_{RO} = 6.5$ GHz which is attributed to sample heating. The heating of the sample leads to a reduction of the bandgap which detunes the peak of the gain spectrum from the cavity mode resulting in a reduction of f_{RO} [Bjö05]. Therefore, higher pump currents were avoided to prevent damage to the microlaser. In order to evaluate the performance of the lasers with respect to τ_{TO} and f_{RO}, one has to compare not only the absolute threshold currents of the microlasers but also corresponding threshold current densities as depicted in Fig. 5.11 (a) and (b), respectively. As the amount of QDs increases quadratically with the diameter of microlaser one expects also the pump current to reach inversion to increase. Here the 2 µm pillar is an exception as it does not exhibit minimal threshold current. This pillar even possesses the highest threshold current density. This behavior is attributed to the fact that microlasers with small diameters experience significant side wall losses [Rei08]. Therefore, microlasers with 3 and 4 µm diameter exhibit the lowest values of the threshold current density $j_{th} < 50\,\mathrm{Acm}^{-2}$ which leads to the best performance with regard to f_{RO}. This behavior is also in agreement with findings in VCSELs where the reduction of the oxide aperture down to 1.5 µm (which exhibits the lowest threshold current of the investigated VCSELs) leads to an increase of f_{RO} [Ros17]. In this paper the authors also find a deviation from this trend for the smallest diameters which is attributed to an increased series resistance, self-heating and mode scattering at the sidewalls.

In the following, optical feedback is applied to get also insight into its possible effects on the relaxation oscillations. This experiment provides additional information on the dynamics for a better characterization with regard to feedback regimes. Therefore, we return to the previously characterized micropillar with 5 µm diameter

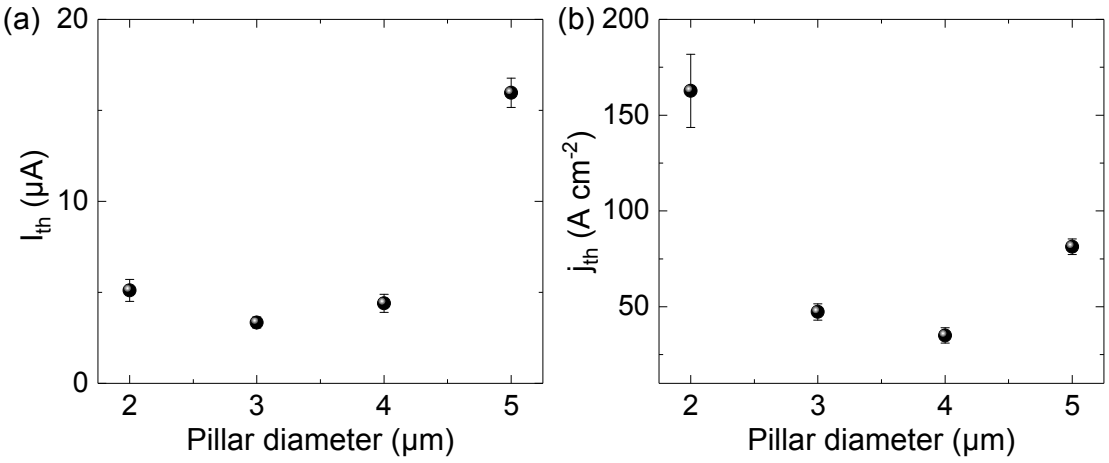

Figure 5.11: (a) Threshold pump current I_{th} and (b) and threshold current density j_{th} are compared for the different examined diameters.

and choose the pump condition $I/I_{\mathrm{th}} = 1.64$ which results in $f_{\mathrm{RO}} = 6.2\,\mathrm{GHz}$ to avoid masking of feedback effects by thermal heating of the sample (marked data point with red circle in Fig. 5.9 (d)). We again choose an external cavity round-trip time of $\tau_{\mathrm{FB}} = 0.97\,\mathrm{ns}$ as in the experiments shown in sections 5.1 and 5.2. In order to both observe the effects of feedback on the relaxation oscillations as well as effects that occur after one cavity round-trip, a trace length of 2 ns is chosen for the streak camera (which is the maximum in the synchroscan operation mode). The pump current of the micropillar is precisely tuned so that an in-phase and out of phase position can be addressed. We would like to emphasize that the injected laser pulse has to be so weak that the microlaser is not effectively pumped as this changes the feedback phase.

Figure 5.12 displays the streak camera time trace both in absence and presence of feedback for the WM. Panel (a) depicts the WM being out of phase with an ECM while (b) shows the in-phase condition. Optical feedback does not significantly influence the relaxation oscillation frequency or its damping. This behavior can be explained by the strong damping of the relaxation oscillations that is also typically found in macroscopic QD lasers [Mal06, Lüd09]. This damping is proportional to the critical feedback strength needed to destabilize the CW laser operation [Mør92, Lev95, Lin15]. The preservation of this strong damping in the microlaser system makes nanolasers using QDs as an active medium ideal candidates for lasers in applications such as super-resolution imaging [Cho16] where robustness against

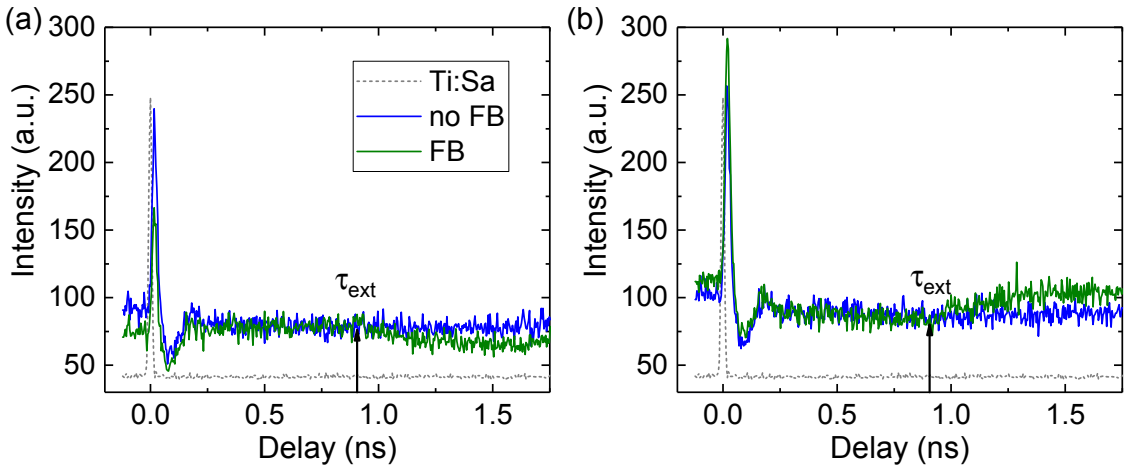

Figure 5.12: Streak camera measurements depicting the WM without and with feedback for both (a) out of phase and (b) in phase conditions. As a timing reference the Ti:Sa pulse is shown as a gray dashed line. Vertical black arrows indicate the external cavity round-trip time.

spurious reflections is required.

The determined relaxation oscillation timescale is equal to $\tau_{RO} = 161\,\text{ps}$ which significantly smaller than the external cavity round-trip times used in the experiments above. Feedback effects in the regime of these very short cavities on the order of τ_{RO} have been identified to exhibit interesting dynamics such as regular pulse packages [Hei01] which are sensitive to the external cavity round-trip time. These dynamics can be explained by an undamping of the relaxation oscillations for external cavity round-trip times close to low multiples of f_{RO} [Coh88]. However, taking into account τ_{RO}, cavity lengths of about 2 cm are required. These are not feasible in the present experimental configuration. In order to naturally access these ranges of very short cavities in micro and nanoscale devices, integrated photonic circuits may provide an attractive option [Too15].

In these feedback experiments no undamping of relaxation oscillations is found, which would have been accompanied by revival peaks in $g^2(\tau)$ as shown for micro-laser A. It has been found that dynamical instabilities are related to the presence of undamped relaxation oscillations [Ack84]. The undamping would also be accompanied by side modes in the optical spectrum [Pet88], which were not observed in our experiments. This can be explained by an insufficient feedback strength as these so called satellite modes are typical for feedback regime IV (see section 2.5). The

phase sensitivity recorded in the previous measurements hints at a behavior that is rather typical for regime II. The chosen approach to examine the relaxation oscillations, however, unveils a fascinating effect related to the used optical pulse. The microlaser is driven with pump currents where feedback leads to a reduction or an increase of the output power. The optical pulse pushes the microlaser out of its stable oscillation effectively resetting the system to its state where no feedback is present. After one external cavity round-trip time we find a decrease or an increase of the laser intensity depending on the feedback phase condition. This means that the stationary feedback state is build up again after one cavity round-trip.

It has to be noted that the microlasers as presented in this work rather offer a testbed system for studying the fundamental physics at the crossroads of nonlinear laser dynamics and nanophotonics than being commercially minded devices. Cryogenic cooling represents a huge practical drawback of this system. However, by optimizing the gain-medium, one can ensure room temperature operation when focusing on applications. To circumvent this issue, one could use long-wavelength InGaAs QDs [Lot00, Sch13] or other low-dimensional gain materials [Jag18, Yan17]. Here the feedback phase could be exploited in the mentioned regime to realize intensity bits. This is in contrast to topological solitons in semiconductor lasers with optical feedback which are a potential candidate for coherent optical communication networks as these would be used as phase bits [Gar15]. The possibility of resetting the stationary feedback state with an external laser pulse can be used for clock recovery. Here, the clocking bandwidth can be increased by further reducing the external cavity length. Therefore, realizing such schemes with integrated photonic circuits is very attractive.

When comparing micropillar lasers to VCSELs used in high speed communication schemes, one still needs to improve the microlasers in terms of modulation bandwidth. One approach could be decreasing the Q-factor which results in an increased modulation bandwidth as it is limited by the inverse cavity lifetime [Bjö91]. Moreover, as VCSELs are an already established technology in data communication, further growth and processing techniques are applied such as the aforementioned electrical contacts in GSG-configuration and the optimization of the doping profiles of the DBRs and of the active medium.

5.5 Summary of chapter 5

This chapter extended our study on high-β QD microlasers for the first time towards coherent optical feedback from a short external cavity. The relative phase difference between the fundamental lasing mode and ECMs can either be controlled by precisely tuning the pump current of the microlaser or by varying the length of the external cavity with a piezo mirror. Thus, one can approach both (in and out of phase) feedback configurations for each mode leading to an increase or decrease in coherence time, respectively. The former scenario is characterized by linewidth narrowing which results in a stabilization of the respective mode, while the latter can be identified by linewidth broadening leading to mode destabilization. Therefore, the external cavity length constitutes another tuning mechanism for tailoring the input-output characteristics as well as the dynamics of microlasers.

Moreover, we examine another fundamental timescale of the microlaser, namely the relaxation oscillations frequency, by the injection of ps-length optical pulses. Even though optical feedback is not able to modify f_{RO} or its damping rate, one can observe a resetting effect of the feedback state. Here the optical pulse causes the microlaser to oscillate in its solitary condition. Interestingly, the "stationary" feedback state is built up again after one cavity round-trip. Integrated photonic circuits may provide a promising platform in order to exploit fast switching between the solitary and the feedback state.

6 Combined lateral and axial excitation and detection schemes

In this chapter we study the effects of optical feedback and injection locking on QD micropillar lasers by utilizing a 90° excitation and detection scheme such as the one presented in [Mus15]. In that paper the authors have already highlighted the benefits of simultaneous lateral and axial detection, enabling a precise extraction of the lasing threshold in the high-β regime. Here, we depict further applications of this powerful measurement configuration. Firstly, we demonstrate a novel method of determining the linewidth enhancement factor α using the lateral detection scheme to determine the modal QD gain which we apply to extract this important parameter for the first time for a QD-microlaser. Furthermore, we prove that injection locking can also be achieved by lateral injection. Finally, the lateral injection is combined with axial feedback, which is significantly enhancing the injection locking range.

6.1 Determining the linewidth enhancement factor α

This chapter discusses different methods for determining the linewidth enhancement factor α which is a crucial parameter for describing the spectral and dynamical behavior of semiconductor lasers [Hen82, Osi87]. After a basic characterization of the used micropillar, we firstly evaluate the results of two established methods with respect to the extraction of α, namely the comparison of the linewidths above and below threshold and injection locking. Then, we propose a novel method which is based on a direct measurement of the change in the modal gain as well as the emission spectrum when subject to delayed optical feedback. Finally, we confirm the validity of the used method by simulations based on a quantum optical model and explain its importance for accessing α in micro- and nanolasers. Figure 6.1 shows an overview of all the experimental techniques of determining α used in this

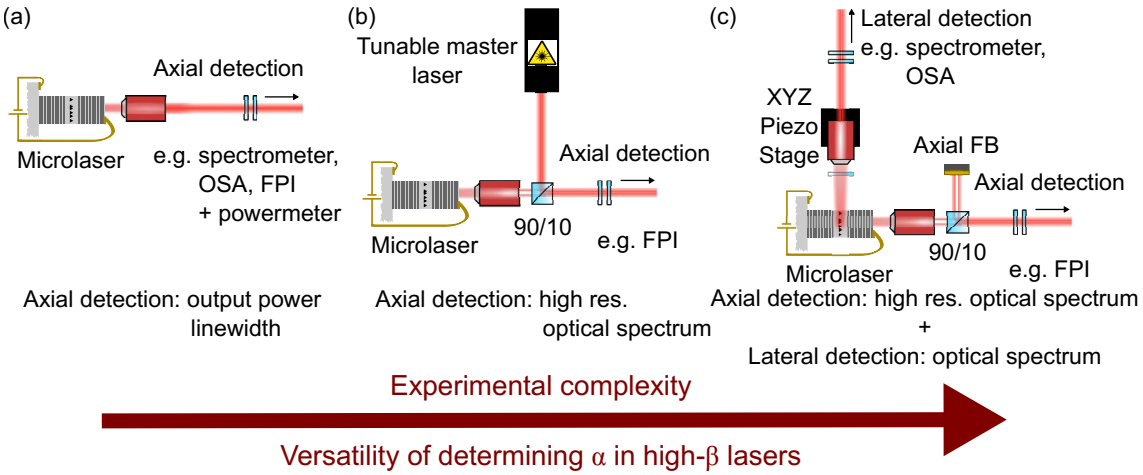

Figure 6.1: Overview of the experimental methods used in this work to determine α. As the methods increase in experimental complexity, they simultaneously become more versatile in the field of high-β lasers and gain additional information such as the pump power dependence: (a) The Schawlow-Townes method only requires measurements of the output power and linewidth of the lasing mode but below and above threshold. (b) The injection locking method additionally needs a tunable external laser and high-resolution measurements of the optical spectrum. (c) Our novel feedback method requires an advanced setup allowing for lateral and axial detection of the optical spectrum.

chapter.

6.1.1 Basic sample characterization

Analogous to previous chapters, we firstly carry out a basic sample characterization in form of the input-output characteristics. It has to be noted that the micropillar sample used for the studies in this chapter had to be cleaved close ($\lesssim 100\,\mu m$) to the micropillar array (consequently, the sample was changed compared to the ones used in previous chapters) to allow for lateral access as required for further experiments. The used microlaser (which is labeled microlaser D) has a diameter of $5\,\mu m$ and a Q-factor of about 20000. Microlaser D is based on the same planar microcavity as micropillar A and exhibits a similar energy of the fundamental mode of $E = 1.37\,eV$. The side mode suppression ratio of this microlaser again exceeds 30 dB above threshold so that higher order transverse modes can be neglected.

Figure 6.2 (a) depicts the input-output characteristics of the used microlaser. It clearly resembles the behavior of microlaser A discussed in chapter 4. At threshold

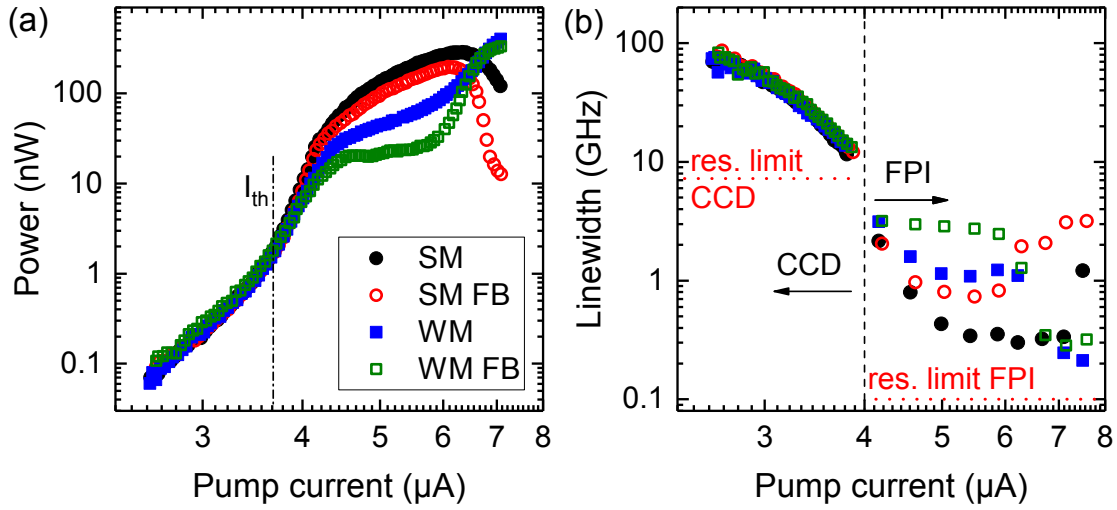

Figure 6.2: (a) Input-output characteristics of the investigated micropillar laser with and without feedback. The lasing threshold current (I_{th}) is marked by a dashed-dotted line. (b) Linewidth as a function of pump current. Measurements below threshold are carried out by a grating spectrometer (CCD) while the ones above are performed with an FPI for a higher spectral resolution of 100 MHz (indicated by red dotted lines). The change of devices as marked by a black dashed line.

we find one mode dominating the lasing action (SM), while the other mode (WM) does not reach the lasing threshold in the intermediate excitation range and shows significant thermal emission properties. For high pump currents we find a crossing in the intensities of SM and WM which is attributed to a change in roles induced by intermode kinetics [Ley17]. In this excitation regime the SM exhibits a significant amount of thermal emission while the WM becomes more coherent. Applying optical feedback leads to a shift of this crossing point to lower pump currents which is consistent with the observations discussed in section 4.1 for microlaser A. This behavior is also confirmed by a measurement of the linewidth of the modes (see 6.2 (b)). Near threshold, the SM undergoes a stronger decrease in linewidth than the WM. Ramping up the pump current results eventually in an increase of the SM's linewidth. Thus, a crossing of both modes is observed also in linewidth at an injection current of 6.7 μA.

One interesting difference when comparing the investigated microlaser D with microlaser A is the decrease of the output power of the WM for currents below the intensity crossing point in the presence of feedback. Additionally, taking into account the increased linewidth compared to the solitary case, this difference is attributed

to stabilization of the WM as a thermal emitter and the SM as a coherent emitter as also previously observed in microlaser A.

6.1.2 Established methods of determining α

In semiconductor lasers the refractive index and the modal gain are two fundamental parameters that cannot be treated independently. The coupling of those parameters to the carrier density is evident by an enhanced emission linewidth above threshold [Fle81, Hen82, Hen85]. This effect is described by the linewidth enhancement factor α:

$$\alpha = \frac{\Delta n'}{\Delta n''} , \tag{6.1}$$

where $\Delta n'$ and $\Delta n''$ denote changes in the real and imaginary parts of the refractive index, respectively. In experiment $\Delta n'$ leads to an optical frequency shift, while $\Delta n''$ causes a change in carrier density. The latter also alters $\Delta n'$ explaining the coupling of both parameters [Hen82]. Even though at first glance only the spectral characteristics of a laser are influenced by the refractive index-gain coupling, α also has a crucial impact on the emission dynamics as well as the sensitivity to optical injection and feedback [Osi87]. Since the first introduction of α by Henry in 1982 [Hen82], several different methods of determining it have been proposed [For07]. As these different methods can even yield different results for the same laser the dependence of α on the operating conditions of a laser as well as limitations of respective methods have to be taken into account [Giu06, Vas00, Lin12, Her16]. In the following, we discuss two established methods which are based on the Schawlow-Townes law and injection locking. Further methods and their limitations in determining α for the first time in QD microlasers are discussed at the end of this chapter.

Schawlow-Townes law

The Schawlow-Townes law states that the linewidth of a laser is inversely proportional to the output power P [Sch58]. At high excitation currents the linewidth is limited by occupation fluctuations of the wetting layer and QD states to a minimal linewidth $\Delta\nu_0$. Therefore, the linewidth of a mode $\Delta\nu$ can be written as follows [Tof92]:

$$\Delta\nu = \Delta\nu_0 + \frac{\zeta_{\lessgtr}}{P} , \tag{6.2}$$

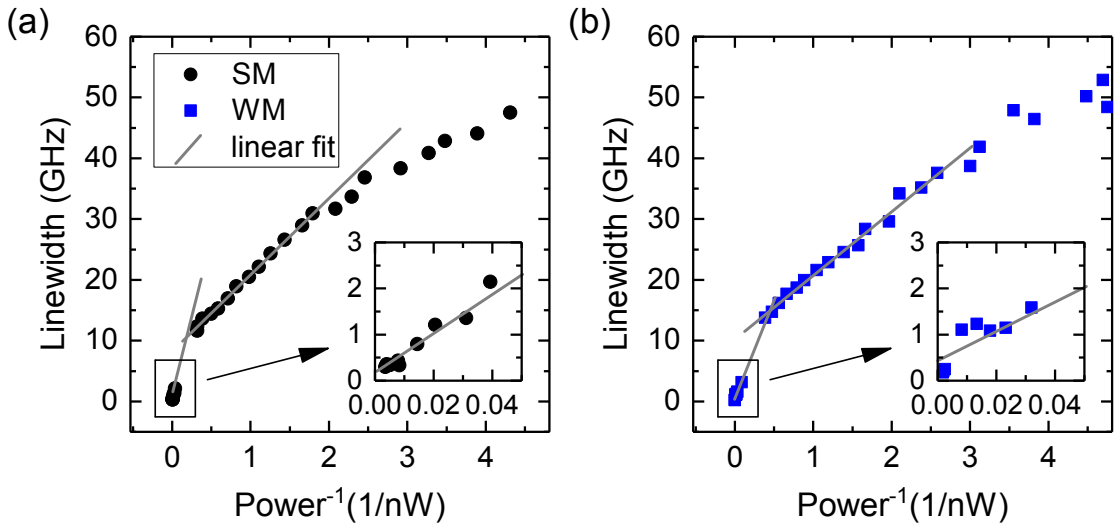

Figure 6.3: Emission linewidth of (a) SM and (b) WM of microlaser D displayed as a function of the inverse optical output power. The α-factor is determined from the slopes $\zeta_{\lessgtr}$ of the linear fits (gray lines) of the linewidths below and above threshold (see inset) with the following parameters: $\zeta_{>,\mathrm{SM}} = (48.6 \pm 3.9)$ GHz·nW, $\zeta_{<,\mathrm{SM}} = (12.8 \pm 0.1)$ GHz·nW, $\zeta_{>,\mathrm{WM}} = (37.8 \pm 5.3)$ GHz·nW and $\zeta_{<,\mathrm{WM}} = (10.2 \pm 0.1)$ GHz·nW

where $\zeta_<$ and $\zeta_>$ denote the characteristic slopes of the linewidth below and above threshold, respectively. Henry later found that the Schawlow-Townes linewidth above threshold is broadened by the factor $1+\alpha^2$ [Hen82]. This behavior is attributed to the coupling of amplitude and phase of the oscillator. It also has to be considered that below threshold the contribution of amplitude noise is comparable to phase noise. Thus, below threshold the absence of this coupling ($\alpha = 0$) leads to $\zeta_< = 2\zeta_>$ as above threshold only frequency modulation noise is prevalent [Tof92]. Consequently, we are able to determine α by the following equation:

$$\alpha = \sqrt{2\frac{\zeta_>}{\zeta_<} - 1}\,. \tag{6.3}$$

Thus, one is able to extract α by combining the information of the output power obtained from the input-output characteristics with the measurement of the corresponding linewidth in the optical spectrum. In order to directly determine the slopes $\zeta_<$ and $\zeta_>$, we plot $\Delta\nu(\frac{1}{P})$ as depicted in Fig. 6.3 (parameters included in caption). Here, $\zeta_>$ exhibits the largest error bars as this slope is determined once

only for data points taken with the FPI and again also including the data point from the spectrometer with the highest output power. As already indicated in Fig. 6.2 (b) the measurements below threshold are carried out by a grating spectrometer with attached CCD while the ones above threshold are performed with an FPI. Even though both the input-output characteristics and the evolution of the linewidth differ for the SM and WM, we find similar values of the linewidth enhancement factor $\alpha_{\text{S-T}}$ acquired with the Schawlow-Townes method that agree within their error bars:

$$\alpha_{\text{S-T,SM}} = 2.4 \pm 0.2 \qquad \alpha_{\text{S-T,WM}} = 2.3 \pm 0.3\,.$$

The agreement of the value of α is not surprising as both modes compete for the common gain and experience the same refractive index fluctuations. Moreover, when comparing our results to literature, we conclude that even though there has been several reports of a change in α with emission wavelength [Vah83, Osi87, Miy89], these dependences are only relevant when the mode energy varies in the range of multiple meV. Thus, when taking into account the mode splitting between SM and WM being only 65 µeV we can expect the same value of α for both modes which is consistent with the experimental results. Hence, in the following α will be determined only for the SM.

Injection Locking

Injection locking constitutes another long-established method for determining the linewidth enhancement factor. For this experiment the feedback mirror is removed, and we instead couple a tunable master laser to the optical path which was previously forming the external cavity. In a previous study on injection locked high-β micropillar lasers that the author carried out in collaboration with Elisabeth Schlottmann [Sch16] we found a striking difference compared to conventional locking of classical semiconductor lasers with β on the order of 10^{-4} to 10^{-6}. While in classical lasers synchronization of the slave laser to the master laser is found with respect to both frequency and phase locking, high-β micropillar lasers exhibit a regime of partial locking. This regime is characterized by a simultaneous oscillation of the emission locked to the master laser as well as emission at the solitary frequency of the microlaser which is mainly driven by spontaneous emission.

Figure 6.4 depicts high-resolution FPI spectra of microlaser D for a pump cur-

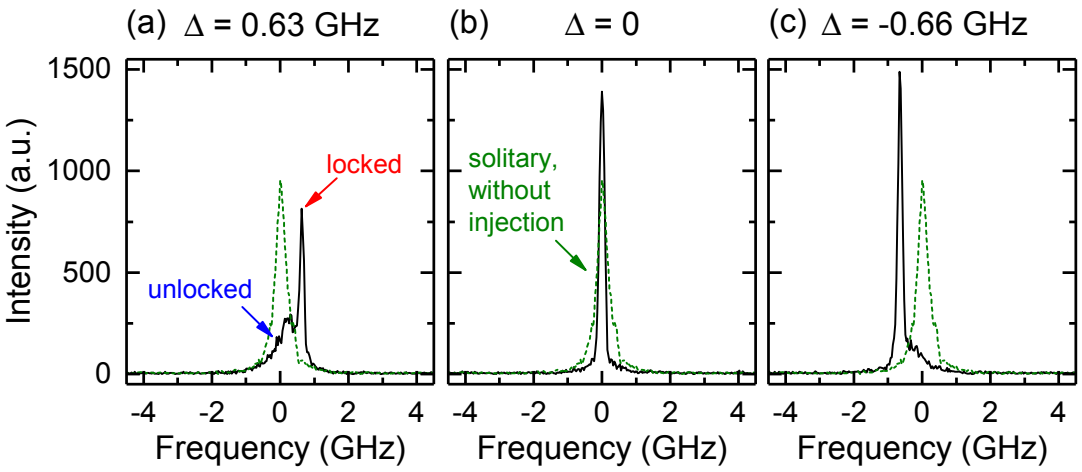

Figure 6.4: High-resolution FPI spectra showing the partial locking phenomenon for different detunings Δ (a) 0.63 GHz, (b) 0 and (c) -0.66 GHz for $I = 1.5\,I_{\mathrm{th}}$. For comparison the solitary laser spectrum is presented with a green dashed line.

rent of $I = 1.5\,I_{\mathrm{th}}$ highlighting the partial locking behavior in the investigated microlaser. For positive detuning of $\Delta = 0.63$ GHz (see panel (a)) we observe the expected superposition of simultaneous locked and unlocked oscillation of the fundamental mode. For reference the solitary slave laser mode is shown as a green dashed line. Here we find the locked mode exhibiting a resolution limited linewidth of 122 MHz, while the unlocked mode with a linewidth of 636 MHz decreases in intensity, slightly broadens and is pulled towards the injected frequency by 0.20 GHz. Panel (b) depicts the case of zero detuning which only exhibits minimal contributions of the unlocked mode as the majority of the oscillation is transferred to the locked mode. Such clear locking is only found when Δ is smaller than the solitary linewidth (379 MHz) of the microlaser. At negative detuning of $\Delta = -0.66$ GHz (see panel (c)) we do not find a mirrored spectrum of panel (a). Instead, we find a scenario with an increased amount of locked oscillation that also leads to stronger injection pulling of 0.35 GHz. Interestingly, this asymmetry enables us to determine the linewidth enhancement factor α from this measurement.

Even though the microlaser emission is phase locked to the master laser and partially unlocked simultaneously, it is still possible to define a region where this partial locking is present. This is usually done by a locking map which is depicted in Fig. 6.5. Here we plot the normalized intensity of the frequency-locked oscillation as a function of the solitary detuning Δ between the master laser and slave microlaser

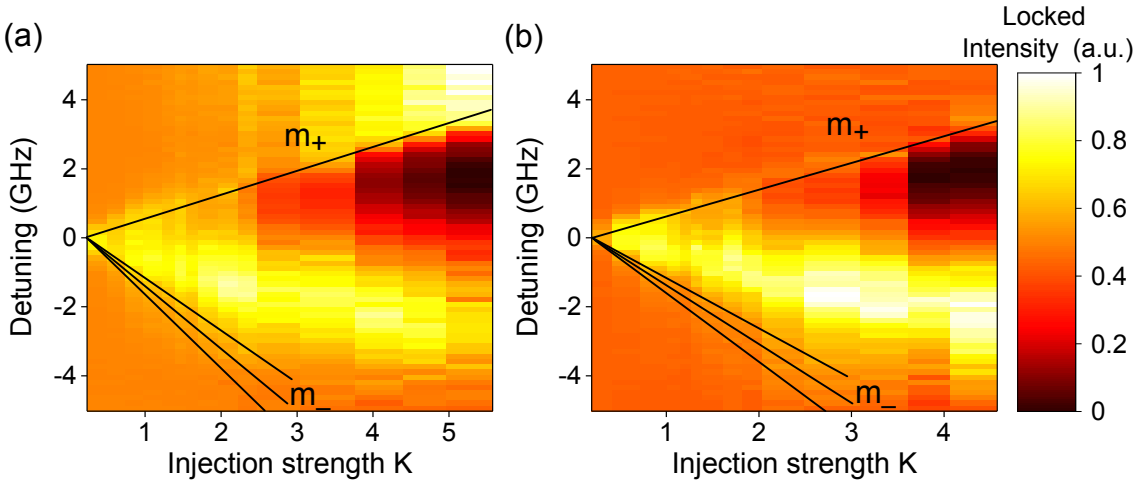

Figure 6.5: Extracting α from injection locking experiments. Normalized intensity of the frequency-locked oscillation as a function of detuning Δ between the master laser and slave microlaser for different pump currents (a) $I = 1.5\,I_{\mathrm{th}}$ and (b) $I = 1.7\,I_{\mathrm{th}}$. The edges of the locking cones with their slopes m_- and m_+ are determined from the points of abrupt change in the locked intensity, are depicted by solid lines. For negative detuning it is difficult to find the exact edge of the cone. Therefore, a range of three slopes is given for m_-.

D for different pump currents, which are $I = 1.5\,I_{\mathrm{th}}$ in Fig. 6.5 (a) and $I = 1.7\,I_{\mathrm{th}}$ in Fig. 6.5 (b). The locking range is then given by the following inequality explaining the aforementioned asymmetry related to the α-factor [Lan82]:

$$C \cdot K\sqrt{1+\alpha^2} < \nu_{\mathrm{locking}} < C \cdot K\,, \tag{6.4}$$

where C is a constant related only to device parameters and K is the injection strength. The latter is the square-root of the ratio of injected power P_{inj} to the free-running slave laser power P_{in} (inside the slave laser cavity), which consequently is very challenging to determine quantitatively in the experiment. Thus, using an effective value is beneficial as the exact value does not have to be explicitly known to determine the α-factor. Therefore, we define $K_{\mathrm{eff}} = \sqrt{\frac{P_{\mathrm{inj}}}{P_{\mathrm{out}}}}$, which is used for the visualization of the data in Fig. 6.5, where P_{out} is the measured optical output power of the microlaser. The α-factor can then be directly calculated from the slopes of the edges of the locking cone m_- and m_+ for negative and positive detunings,

respectively using equation 6.4 [Liu01]:

$$\alpha = \sqrt{\left(\frac{m_-}{m_+}\right)^2 - 1}\,. \tag{6.5}$$

Here we would like to note that the locked intensity for high values of K_{eff} is extraordinarily high outside of the locking cone for positive detunings. This can be attributed to a partial locking region outside locking cone which is accompanied by injection pushing [Hua96]. As this effect is only present at high injection strengths it does not affect the calculation of α. For the two pump currents this measurement was carried out we obtain the following values (with the following parameters extracted from Fig. 6.5: $m_-^{1.5I_{\text{th}}} = (1.7 \pm 0.2)$ GHz, $m_+^{1.5I_{\text{th}}} = (0.66 \pm 0.05)$ GHz, $m_-^{1.7I_{\text{th}}} = (1.6 \pm 0.2)$ GHz and $m_-^{1.7I_{\text{th}}} = (0.75 \pm 0.05)$ GHz):

$$\alpha_{\text{IL}}^{1.5I_{\text{th}}} = 2.3 \pm 0.4 \qquad \alpha_{\text{IL}}^{1.7I_{\text{th}}} = 1.9 \pm 0.3\,.$$

Interestingly, the injection locking experiment indicates different values of α for the two used pump conditions. The existence of a pump power dependent linewidth enhancement factor has previously been reported for QD [Vaz06], submonolayer QD [Her16] and quantum well devices [Nak91] as well as quantum cascade lasers [Jum16]. These works relate an increase of α with pump current to a reduction of the gain caused by spectral hole burning [Agr89]. Consequently, the value of α that was previously determined by the Schawlow-Townes law should be considered as an average or effective value for the used pump current range.

6.1.3 Determining the pump dependence of α in micropillar lasers

As explained in chapter 3.2, our µEL setup is equipped for the simultaneous detection of both axial and lateral emission of the microlaser. This advanced lateral detection scheme allows us to access the active region gain without any filtering carried out by the DBR cavity in the vertical direction. Taking advantage of this experimental configuration, we propose a new method of determining the linewidth enhancement factor which is based on the definition of α (eq. 6.1). This definition

can be rewritten by observables of our experiment:

$$\alpha = 4\pi \frac{\Delta\nu}{\Delta G} , \tag{6.6}$$

namely an optical frequency shift $\Delta\nu$ and a change in modal gain ΔG. Importantly, optical feedback (in axial direction as in previous chapter) is used to induce a change in the optical spectrum as well as the gain by modifying the laser losses.

Firstly, we focus on how to extract modal gain G from the lateral emission spectra. Therefore, the relevant part of the experimental setup is presented in detail in Fig. 6.6. Taking a polarization scan in axial detection (analogous to Fig. 4.5), we are able to determine the polarization basis of the strong and weak mode. The absolute polarization angle is not relevant when working with axial detection but plays an important role in the lateral detection scheme. Figure 6.6 (b) and (c) depict this issue for the polarization of the used microlaser in the experiment. Microlaser D is chosen for this experiment because only the SM can be detected as the orientation of the WM polarization prohibits photons from being emitted in the direction of the microscope objective. Adding a linear polarizer to the lateral detection path ensures that all stray light of the WM is suppressed. When applying a linear polarizer in axial detection that only allows the SM to pass, we are able to compare the spectra of both detection arms in the same polarization basis.

Figure 6.7 depicts this comparison for five different pump currents from below threshold ($I/I_{\mathrm{th}} = 0.85$) to a scenario well above threshold ($I/I_{\mathrm{th}} = 1.86$). Panel (a) shows the µEL spectra of microlaser D in the lateral detection scheme. Here we measure the emission of the QDs that constitute the gain of the microlaser. From these spectra it is evident that the gain is clamped when increasing the pump beyond threshold [Ern10]. Panels (b) to (f) show respective µEL spectra in axial detection. We find a constantly increasing intensity of the lasing mode as expected from the input-output characteristics (see Fig. 6.2). As both spectrometers are calibrated so that they record identical photon energies, we can identify the peak at $E = 1.3664\,\mathrm{eV}$ that is present in panel (a) as scattered light of the lasing mode. It has to be noted that spatial filtering cannot be effectively applied to suppress this emission, because the cavity mode stray light originating from sidewall scattering of the micropillar coincides spatially with the lateral emission [Mus15]. Consequently, this scattered light has to be disregarded when determining the modal gain G.

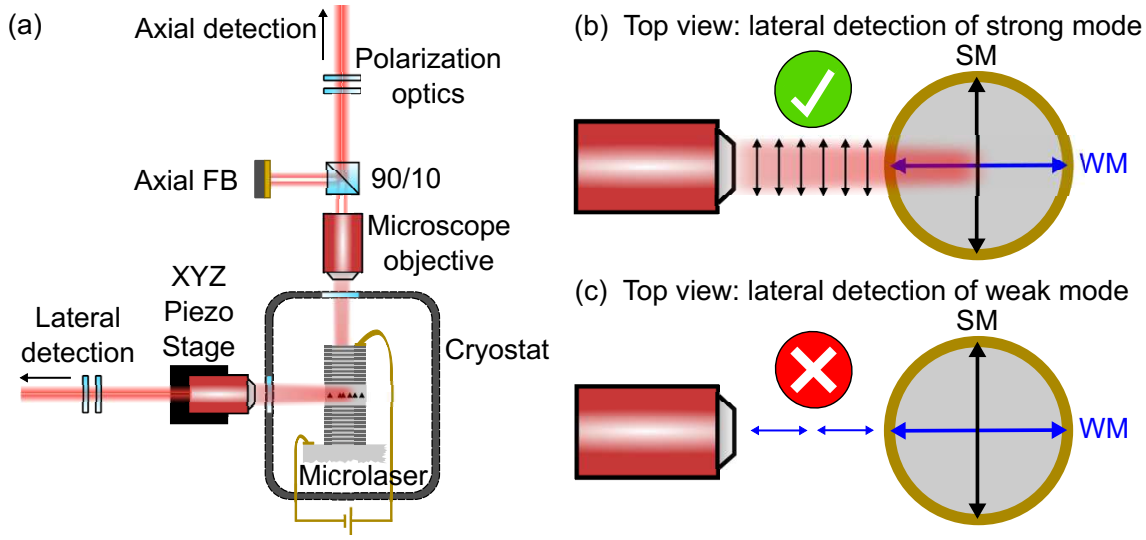

Figure 6.6: (a) Sketch of the experimental setup allowing for simultaneous detection of axial and lateral emission. (b) and (c) depict the top view of the microlaser explaining that only the SM can be detected in the lateral detection scheme taking into account the orientation of the polarization basis of the microlaser.

In order to quantify G, we integrate the measured QD gain-intensity around the lasing mode (shaded gray area in Fig. 6.7 (a)). For a correct estimation of the spectral region of QDs contributing to the modal gain of the lasing mode we analyze the effect of gain clamping for different integration ranges. Figure 6.8 depicts the resulting QD gain for integration ranges extending from 1.2 to 45.6 meV centered to the energy of the laser mode. We choose the minimum integration range from the lateral spectrum of 9.7 meV (highlighted as a thick line) that both exhibits a clear kink as well as apparent carrier clamping. Too small integration ranges depict only a very shallow kink as not enough gain was included in the integration, while too large ranges do not exhibit clear gain clamping due to excess of amplified spontaneous emission. The more detuned the QD gain is from the mode, the less clamped its contribution to the gain. Therefore, the lack of gain clamping is more related to weak mode-gain coupling than to gain compression. Gain compression is a power dependent effect that can lead to non-pinning of the carrier density and consequently to variations in the linewidth enhancement factor with pump current [Jum14]. Nevertheless, this effect is related to spontaneous emission and leads to gain compression of the lasing mode because the injected carriers may recombine in the spatially and spectrally far-off gain regions, before they can fill the spatial or

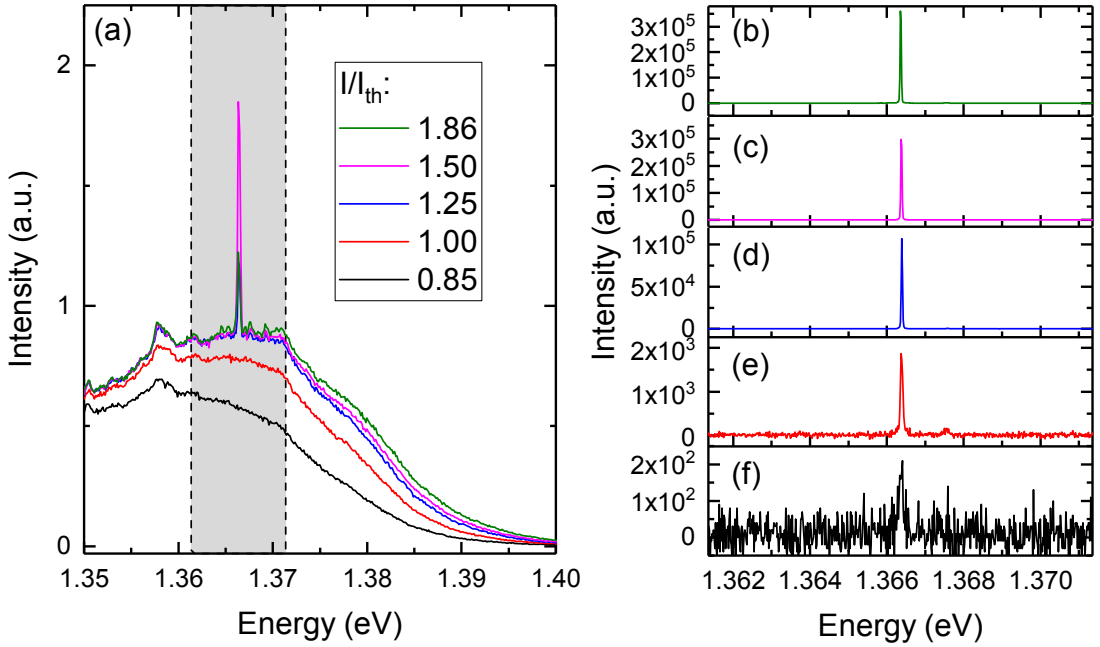

Figure 6.7: (a) Spectra of the QD emission measured in lateral detection. The shaded gray area indicates the integration range of the gain contributing to the lasing mode. (b)-(f) Corresponding spectra of the fundamental mode in axial detection. A higher lateral mode that is still visible at I_{th} is suppressed for higher pump currents.

spectral hole that was burned by the lasing mode. This means QDs with a large spectral detuning do not strongly contribute to the mode via stimulated emission but mainly by spontaneous emission.

By now we have only extracted an integrated value proportional to the QD gain. In order to quantify the modal gain in terms of an absolute number, we utilize two assumptions from [Bjö94]: the modal gain is zero at inversion and the maximum modal gain is clamped to the cavity loss rate κ with

$$\kappa = \frac{2\pi\nu_0}{Q} = 106\,\mathrm{ns}^{-1}\,, \tag{6.7}$$

where $\nu_0 = 331\,\mathrm{THz}$ denotes the frequency of the fundamental mode (SM) with $Q \simeq 20000$. By applying optical feedback, the effective cavity loss rate of the coupled cavity κ_{eff} is reduced in comparison to the solitary case. Therefore, also the maximal modal gain is reduced as depicted in Fig. 6.9 (a). It has to be noted that we compare two scenarios here: In one case feedback is absent while in the other case the maximal feedback strength is applied (as explained in section 4.4).

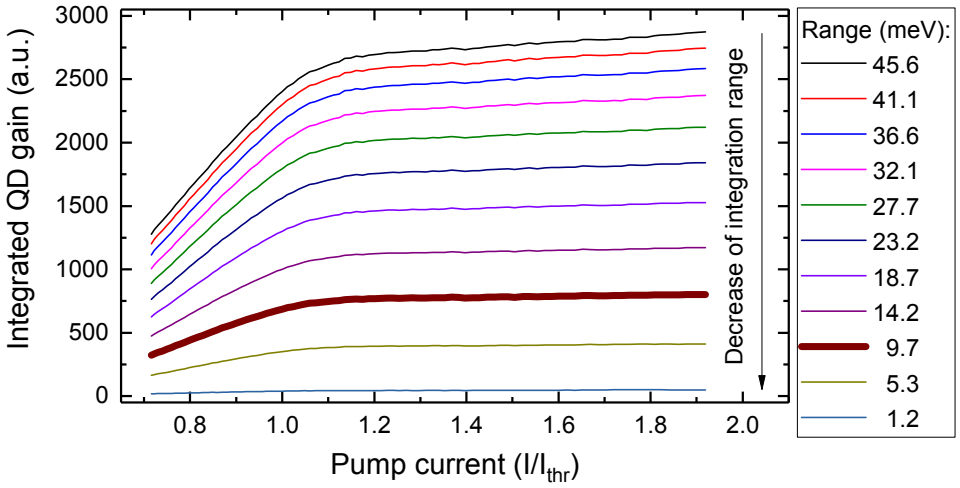

Figure 6.8: Determining of the correction integration range. The integrated QD gain as a function of the pump current is shown for different integration ranges and extends from 1.2 to 45.6 meV centered to $E = 1.366$ eV. The chosen range is highlighted as a thick line.

In order to calculate α with equation 6.6, one needs to evaluate the corresponding frequency shift that is induced by feedback. This frequency shift is dependent on the pump current as well as the feedback strength [Ack84, Len84]. For practical reasons we keep the latter constant while varying the former. Figure 6.9 (b) depicts optical spectra measured by the FPI both in absence and presence of feedback. From fitting of a Lorentzian to the spectra of the SM, we are able to determine the frequency shift. This process is then repeated for several pump current conditions.

It has to be noted that this fitting procedure only provides reliable results when narrow lineshapes are preserved under the influence of feedback. Therefore, feedback parameters (cavity length, feedback strength) and pump currents must be chosen accordingly to meet this condition (compare feedback regimes in section 2.5). Especially in the case of coherence collapse, the linewidth broadens up to multiple GHz and a strong asymmetry in the optical spectrum can be found [Len85]. Consequently, it would be challenging to define a precise shift of the lasing frequency. In the presented experiment an external cavity length of 1.58 m ($\tau_{FB} = 5.3$ ns) is used which is greater than the maximum coherence length of the lasing mode of 33 cm ($\tau_{coh} = 1.1$ ns). Thus, our novel method of determining α is not limited to coherent feedback.

For a first estimate we can now calculate α with our method by averaging the

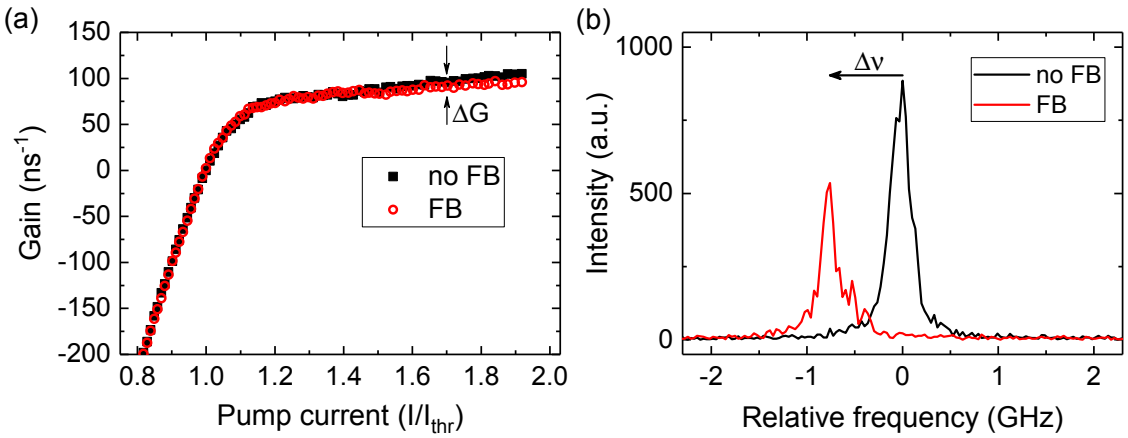

Figure 6.9: (a) Modal gain (extracted from lateral QD gain spectra) as a function of the pump current with and without optical feedback. (b) Exemplary high-resolution FPI spectra of the microlaser exhibiting a feedback-induced shift of the lasing mode at $I = 1.9\,I_{\mathrm{th}}$.

feedback-induced mode shift $\Delta\nu_{\mathrm{avg}} = (0.79 \pm 0.03)\,\mathrm{GHz}$ (average of all frequency shifts in the FPI spectra from the pump current $I = 1.23\,I_{\mathrm{th}}$ to $1.84\,I_{\mathrm{th}}$) and change in modal gain $\Delta G_{\mathrm{avg}} = (4.33 \pm 0.54)\,\mathrm{ns}^{-1}$ (average of all data points of the QD gain evaluated from lateral emission spectra for $I > 1.2\,I_{\mathrm{th}}$) using equation 6.6:

$$\alpha_{\mathrm{FB,\,avg}} = 2.3 \pm 0.3.$$

While this value agrees with the previously discussed methods of Schawlow-Townes law and injection locking, it does not include a possible pump current dependence.

In order to evaluate the pump current dependence, one must not take the averaged frequency and gain shifts but determine them point by point along the input-output curve. As the density of measured data points of spectra in lateral detection is higher than the number of FPI spectra for determining the wavelengths shift, ΔG is still averaged around the pump current of respective spectrum to minimize error bars. Additionally, the proposed method is supported by a quantum optical model. Details on this model which was developed by Brett H. Hokr (U.S. Army Space and Missile Defense Command, Huntsville, USA) and Weng W. Chow (Sandia National Laboratories, Albuquerque, USA) can be found in Appendix A.2.

Figure 6.10 gives an overview of the proposed method comparing it with both the quantum optical model as well as the results acquired with the established methods.

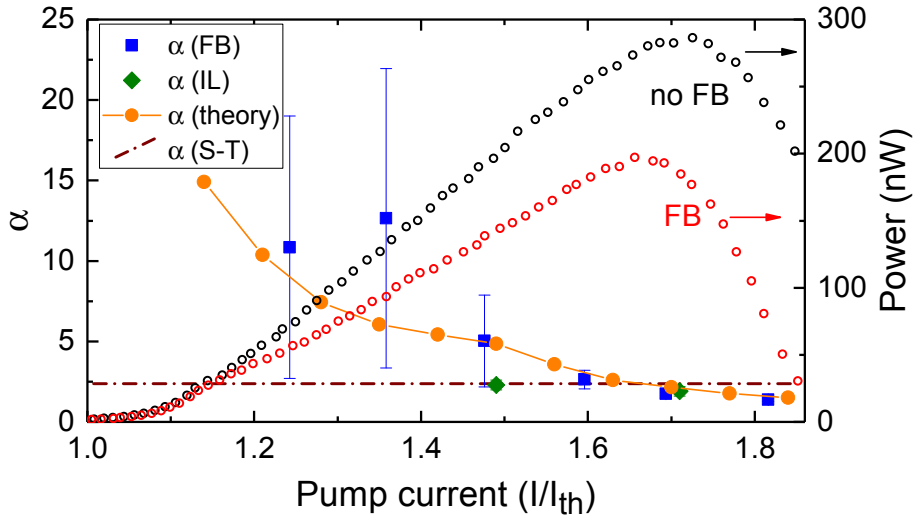

Figure 6.10: Pump current dependence of the α-factor for all presented methods. The proposed method (blue squares), theory (orange circles), injection locking (green diamonds) and the Schawlow-Townes-like law (dash-dotted brown line) are compared. The input-output characteristics is depicted in linear scale referring to the right y-axis as a reference (red and black open circles for feedback and no feedback scenarios, respectively).

In order to visualize the pump current dependence, we display the input-output characteristics of the investigated mode as a reference. The different methods as well as the simulations are in agreement with each other. More importantly, the feedback method unveils a clear pump power dependence of α, which was already indicated by the injection locking method.

As the change in modal gain is very small close to threshold, we find larger error bars in this regime. It also has to be taken into account that $g^{(2)}(\tau = 0)$ does not reach unity in high-β lasers at threshold. Accordingly, the threshold given by the jump in intensity does not coincide with the one defined by second-order coherence [Loh18], so defining α for this condition is problematic. For low pump currents, we obtain large values of $\alpha > 10$ indicating significant broadening of the spectrum for QD microlasers close to threshold. When increasing the excitation current, α decreases approaching a constant value of ∼1.5. The quantum optical model precisely matches this behavior. Thus, the Schawlow-Townes as well as the averaged feedback method yields values that are representative for the moderate to high pump currents used in the experiment.

These high values of α at low pump currents can be explained with the quantum optical model. A decrease of the refractive index is caused by frequency pulling towards the wetting layer gain which is a 2D quantum well (QW). Frequency pulling here describes the pulling of the lasing frequency towards the spectral region where the population inversion occurs [Sar74].

In our case, the frequency pulling was identified by looking at the polarization. As explained in more detail in [Lor07], there are two parts to the susceptibility that correspond to the QD polarization and to the QW polarization, respectively. One has to note that in the presence of Coulomb interaction, the division is not strictly true because of mixing of QD and QW states by the Coulomb potential which leads to Hartree-Fock interaction terms [Lor07]. However, in the regime of low excitation, when the gain peak is at the QD resonance, the QW polarization has a significant effect on the refractive index at the frequency of the QD resonance, when the QD resonance and QW band edge separation is small (10 to 20 meV). This means that even for low pump currents we find a significant population in the QW states which causes high values of $\alpha > 10$. Moreover, the accurate model pump-dependence reveals two different decay constants for α. To explain these two different constants, one has to take into account that for different currents the dominant contributions to the gain changes. For low pump conditions the gain is predominantly influenced by the QDs. However, for increasing pump current the QW gain starts to dominate, leading to a shallower decay of α around $\sim 1.5\, I/I_{\mathrm{th}}$.

Noteworthy, this gain transition effect is unique for our type of QDs with low indium content. Here the energy levels of the QDs have only a small separation to those of the QW. From numerical modeling (W. Chow, see Appendix A.2) we obtain an electron (hole) distance of 10 meV (19 meV) to the conduction (valence) band edge of the wetting layer. When the QD confinement is large, e.g. in long wavelength InAs QDs, this frequency pulling contribution is smaller and α reduces considerably. Moreover, this pump dependent decrease of α depends on the specific gain characteristics of the considered semiconductor laser. For instance the quantum cascade laser described in [Jum16] exhibits increase of the α with pump current which is caused by gain compression. Additionally, when further increasing the pump current beyond the thermal rollover (which is not reached in our experiments to avoid sample degradation) may lead to an increase of α which can be attributed to gain saturation [Agr89]. Taking into account that the linewidth de-

creases with increasing pump current (see Fig. 6.2), we find good agreement with the dependencies between α and linewidth found in [Giu05, Giu06] for various types of lasers.

Noteworthy, the value of α is related to the inhomogeneous broadening of the QDs. In the limiting case of a single QD laser, which can be described by a two-level system, α becomes zero as the gain spectrum would be symmetric [Lüd11]. Therefore, a large inhomogeneous broadening increases the sensitivity to optical feedback for QD microlasers [Ott10].

6.1.4 Evaluation of the different methods

In this section we discuss how the technique introduced in 6.1.3 compares to other methods of determining α. We are not only going beyond the two methods from 6.1.2 but evaluate these in the scope of their applicability in QD microlasers as well as nanolasers in general.

Schawlow-Townes law

As discussed in the previous section the main drawback of this technique is related to the power-averaged value of α. Generally, these averaged values are nevertheless used in rate equation models (such as the one used in chapter 4) when more precisely measured data are not available. It has to be highlighted that this method shines because of its simplicity, requiring only information about the output power and linewidth. Thus, it is in principle applicable to various types of lasers from semiconductor lasers to nanolasers. Especially, for the latter where multi-GHz linewidth are expected, measurements with grating spectrometers or optical spectrum analyzers are sufficient. However, one has to note that deviations from the Schawlow-Townes law occur for very low optical output powers when the β-factor approaches unity [Els84]. Therefore, further numerical modeling will be required in the field of nanolasers to acquire an accurate value of α. Additionally, nanolasers often suffer from thermally induced linewidth broadening at high pump powers [Gon10, Jag18]. Thus, the linewidth method will yield too small values of α as $\zeta_>$ is underestimated by this linewidth broadening.

Injection-based techniques

The injection locking technique as presented in section 6.1.2 has the advantage of mapping the current dependency of α. Furthermore, it is not limited to any special geometry of lasers unlike e.g. the Hakki-Paoli method [Hak75] that is not applicable in case of vertical emitting lasers. Therefore, injection-based techniques of determining α are very well suited for QD microlaser. The main drawback of this method is the decreasing precision for nanolasers with high β-factors. Here the partial locking causes the spontaneous emission to remain unlocked in the solitary laser mode. Thus, determining the locking range becomes more difficult when increasing β. Additionally, one needs higher injection intensities to reach locked oscillation which in turn will rather lead to coherent pumping than locking. We would like to point out that under constant output power as well as constant injection strength one expects the locking range to scale with $\frac{1}{Q}$ [Ern10, Wie05]. As a result, applying this method becomes more challenging for nanolasers based on high Q-factor cavities.

In literature we find further injection-based methods such as measuring the change in device voltage under injection [Hui90]. As this method only works with very low injection strengths where the regime of locking can be approximated to be symmetrical it is also not suitable for high-β nanolasers. Furthermore, to use this technique with our QD microlasers, we need to apply individual contacting of these lasers. This can be easily achieved by using contacting needles (as commonly applied for VCSELs) which also opens up the possibility of current modulation [Vil09].

Feedback-based methods

Firstly, we introduce another established technique based on feedback, the so called self-mixing interferometry. This method is also able to determine the power dependency of α. Here one relies on coherent effects of mixing the feedback with the solitary lasing field to generate a modulation of the optical output power in form of an interferometric waveform [Yu04]. The shape of the interferogram exhibits a hysteresis from which one can determine α. In nanolasers, this coherence requirement typically requires very short external cavities. The publication of Hayenga et al. [Hay16] presents metallic nanolasers with a minimum linewidth of $\sim$0.7 nm. Taking into account the emission wavelength of 1300 nm this results in a coherence length 0.8 mm. Implementing a feedback mirror at such short distances would be

technologically very challenging, especially at cryogenic temperatures.

The technique that was introduced in 6.1.3 does not have any requirements on the feedback strength or cavity length as long as narrow microlaser emission lines are preserved. In comparison to self-mixing interferometry, being able to work in the regime of incoherent feedback is beneficial. Therefore, our technique constitutes an ideal candidate for investigating vertically emitting lasers from VCSELs to nanolasers as the key requirement is given by the accessibility of the gain medium perpendicular to emission direction of the laser.

6.2 Simultaneous optical injection and feedback

Simultaneous optical injection and feedback constitutes a powerful technique to e.g. improve the timing jitter as well as the time-bandwidth product of a mode-locked semiconductor lasers [Soo13]. Each individual approach is only capable of significantly enhancing one of these figures of merit. Here, we apply this technique by utilizing the lateral access to the microlaser for the optical injection part. Similar to the mentioned publication [Soo13], feedback has to be filtered in order to suppress interference effects of the injected laser. This is done in our case by using a linear polarizer in the axial feedback cavity. Therefore, we first explain the behavior of microlaser D in the presence of polarized feedback. Before investigating the combined system, the differences between axial and lateral injection are highlighted. Finally, we prove that pulsed injection enables storing of optical pulses in the external cavity. Figure 6.11 shows an overview of the experimental setups used in this section.

6.2.1 Polarized feedback

When combining optical injection and feedback one problem arises. The injected laser pulse is also fed back into the microlaser. As the coherence length of the used master laser is in the range of µs, the laser light that is reflected from the external cavity mirror can lead to interference effects in the microlaser.

In order to investigate this issue, we perform a detuning sweep of the master laser as depicted in Fig. 6.12 (a). The master laser is laterally injected into the unbiased microlaser and axially fed back from the external cavity mirror. We measure the output power during the detuning sweep with the FPI. One can clearly observe

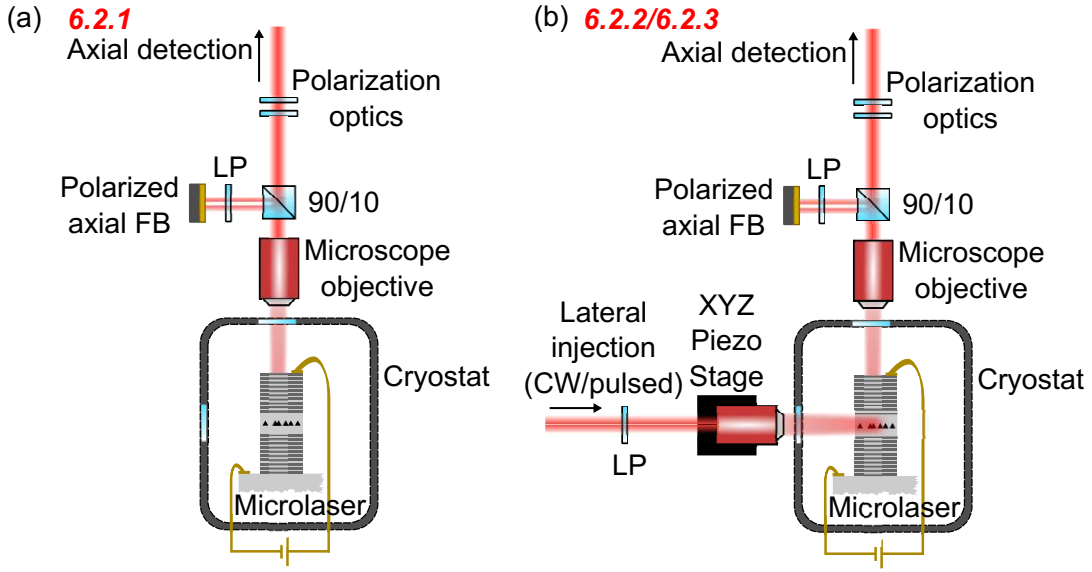

Figure 6.11: Overview of the experimental techniques presented in this section: (a) Basic configuration of polarized feedback as presented in 6.2.1. (b) Simultaneous lateral optical injection and polarized axial feedback as explained in 6.2.2 and 6.2.3 for CW and pulsed injection, respectively.

that the laser oscillates in its output intensity with changing frequency. This is attributed to interference effects in the microlaser as the intensity modulation frequency is equal to the inverse external cavity round-trip time. This issue is very problematic for injection locking experiments as one requires a constant injection strength when recording e.g. locking maps. Therefore, in the following experiments we limit ourselves to polarized optical feedback. We are injecting into the SM of the microlaser, consequently, a linear polarizer aligned to the WM has to be inserted into the external cavity. Figure 6.12 (b) depicts the resulting laser sweep under polarized feedback. Here the intensity modulation vanishes, and a constant injection strength can be retrieved.

One has to repeat the basic sample characterization when polarized feedback is applied. Figure 6.13 (a) depicts the input-output characteristics of microlaser D. When comparing the results with Fig. 6.2 (standard feedback) one observes a clearly different behavior. Only feeding back the WM leads to a strong decrease of the SM intensity at the point where SM and WM diverge in the absence of feedback while the WM intensity increases. This causes the intensity crossing point with polarized

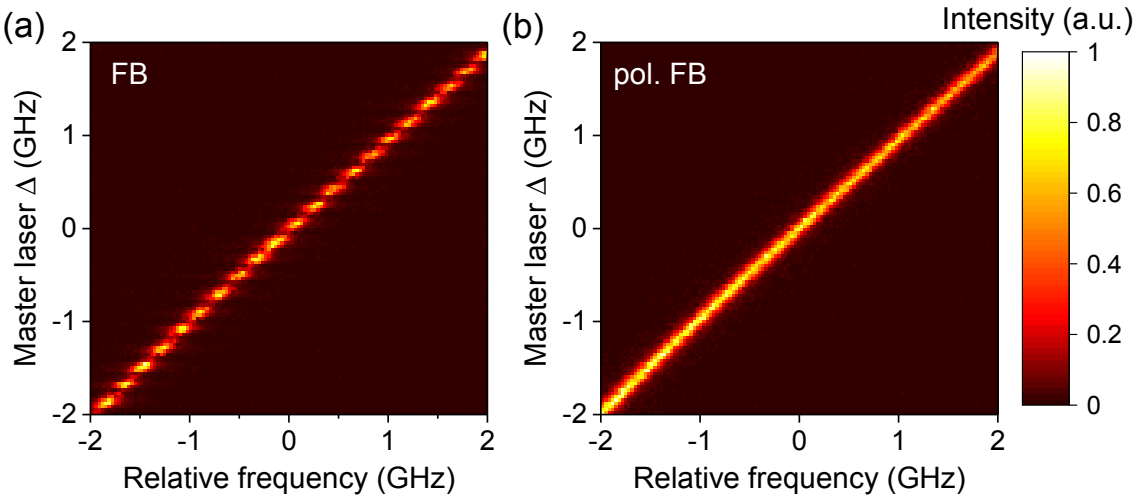

Figure 6.12: Heatmaps of FPI spectra depicting a frequency sweep of the master laser while the microlaser is turned off. Panel (a) shows the case of standard FB leading to a modulation of the recorded laser intensity. This can be eliminated by using polarized feedback (perpendicular to the injected laser) as highlighted in panel (b).

feedback to be significantly lower than in the case of standard feedback:

$$I_{\mathrm{X}}^{\mathrm{polFB}} = (4.85 \pm 0.05)\mathrm{mA} \quad < \quad I_{\mathrm{X}}^{\mathrm{FB}} = (6.47 \pm 0.05)\mathrm{mA}\ .$$

Therefore, polarized feedback causes the WM to be the dominant lasing mode for $I > I_{\mathrm{X}}^{\mathrm{polFB}}$. This behavior is also indicated by a clear linewidth reduction of the WM as illustrated in Fig. 6.13 (b). Considering that exclusively the WM is coupled back, means that only the intracavity photon population of respective mode gets enhanced which results in stimulated emission of this mode. The SM on the other hand shows an increase of the linewidth indicating mainly thermal emission. This can be related to a reduction in the gain of the mode orthogonal to the one coupled back, which is in agreement to previous findings in the QD micropillar laser system [Hop13].

One has to note that a difference between standard and polarized feedback in the investigated microlasers is found only to be crucial when bimodal switching dynamics are already present in the solitary microlaser. When one mode dominates the lasing oscillation, polarized feedback of the dominant mode and standard feedback lead to similar results. In case of microlaser D the WM is generally enhanced by feedback. This polarized feedback experiment shows that only feeding back the

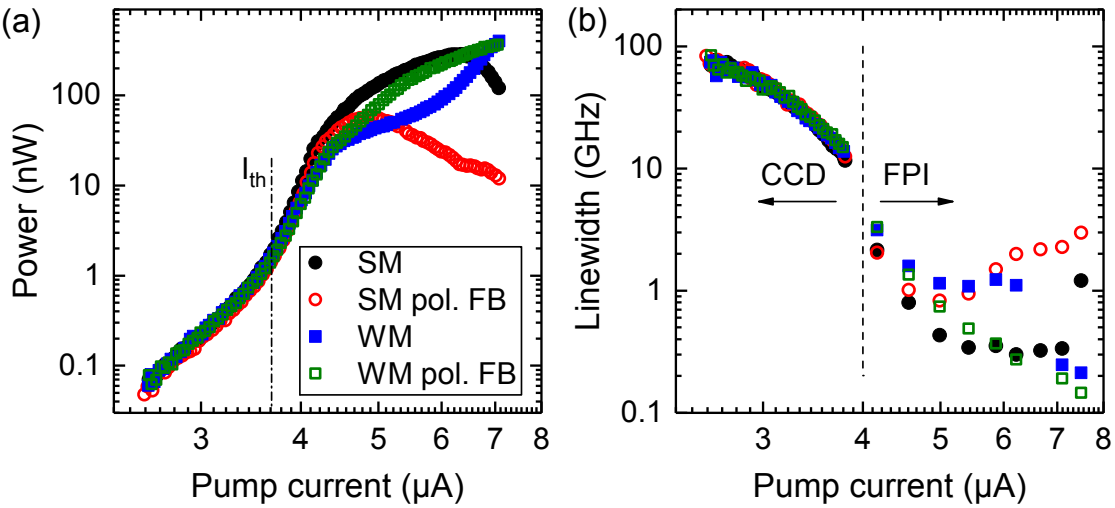

Figure 6.13: (a) Input-output characteristics of micropillar laser D without and with polarized feedback of only the WM. The lasing threshold current (I_{th}) is marked by a dashed-dotted line. (b) Linewidth as a function of pump current. The change of recording devices is again marked by a dashed line.

mode that gets enhanced leads to a stronger effect. Thus, WM feedback stabilizes the lasing oscillation of the same mode. This is in contrast to standard feedback for which pump conditions can be found where one mode is stabilized or destabilized, respectively. In case of microlaser D standard feedback causes first the SM to be stabilized in its lasing oscillation directly above threshold, while the WM is stabilized only for high currents close to and above the intensity crossing point. As SM and WM are fed back, both modes have to be taken into account for a stability analysis.

6.2.2 Combination of polarized feedback and lateral injection

In this section we combine axial polarized feedback from the WM with lateral injection into the SM. Figure 6.14 depicts detuning scans of the master laser over the slave microlaser. Firstly, we focus on panels (a) and (c) which are recorded in absence of feedback to get an understanding of the lateral injection process. Therefore, we define a lateral injection strength

$$K^* = C_{\mathrm{scaling}} \cdot \eta_{\mathrm{inj}} \cdot K, \tag{6.8}$$

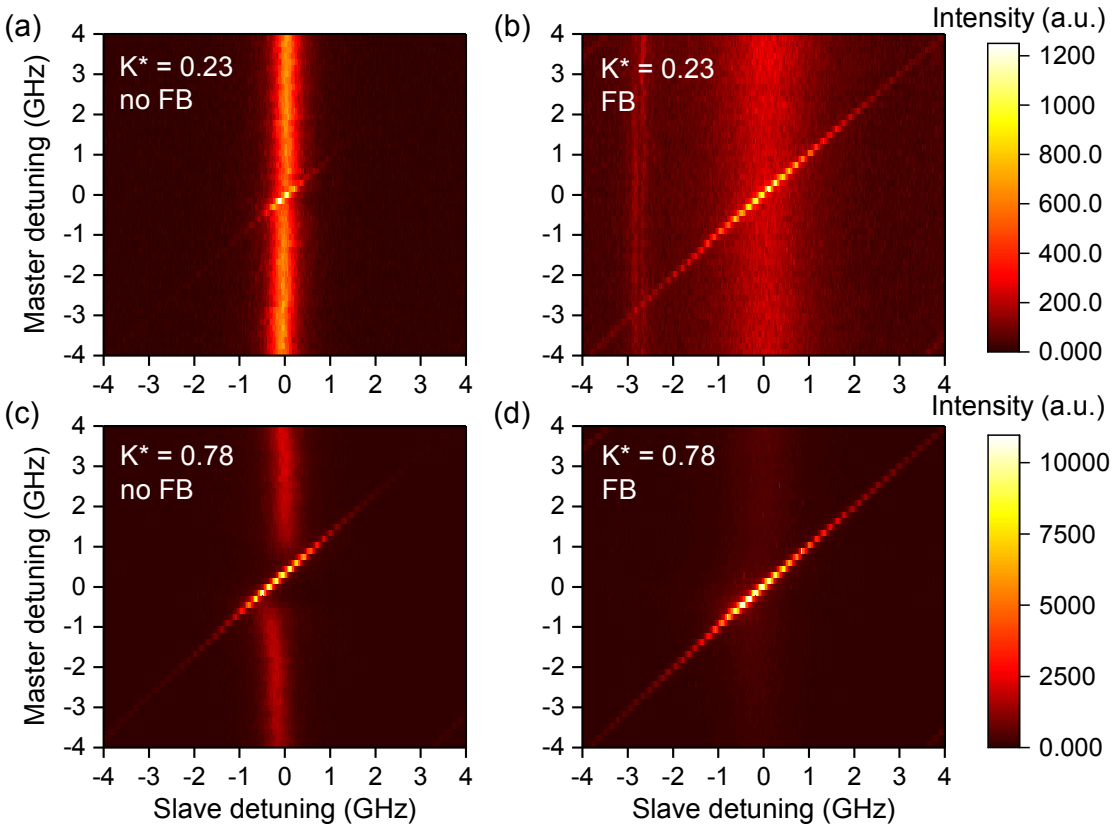

Figure 6.14: Lateral injection locking of the SM at $I = 1.5\, I_{\mathrm{th}}$ illustrated by heatmaps of the detuning scans. The upper panels (a) and (b) depict the results for $K^* = 0.23$ in absence and presence of polarized feedback, respectively, while the lower panels (c) and (d) present corresponding cases at $K^* = 0.78$.

where C_{scaling} denotes a scaling parameter and η_{inj} describes the lateral injection efficiency. In this lateral injection scheme one cannot extract an exact value of η_{inj} as there are not only losses from scattering of the laser beam at the sample edge and the benzocyclobuthene but mode matching is worse than in the case of conventional locking. It has to be highlighted that the microlasers should in the best case be closer than $\sim 10\,\mu\mathrm{m}$ to the cleaved edge to prevent shadowing of the excitation beam by the edge when taking into account the numerical aperture of the objective $NA = 0.4$ and the height of the microlaser $h_{\mathrm{ML}} = 8.2\,\mu\mathrm{m}$. In experiment this distance is $\sim 80\,\mu\mathrm{m}$ which means the master laser is partly blocked by the substrate. Thus, we introduce C_{scaling} to rescale the lateral injection strength. Here, $K^* = 1$ represents the maximum of the injection strength used in the experiment. Interestingly, the

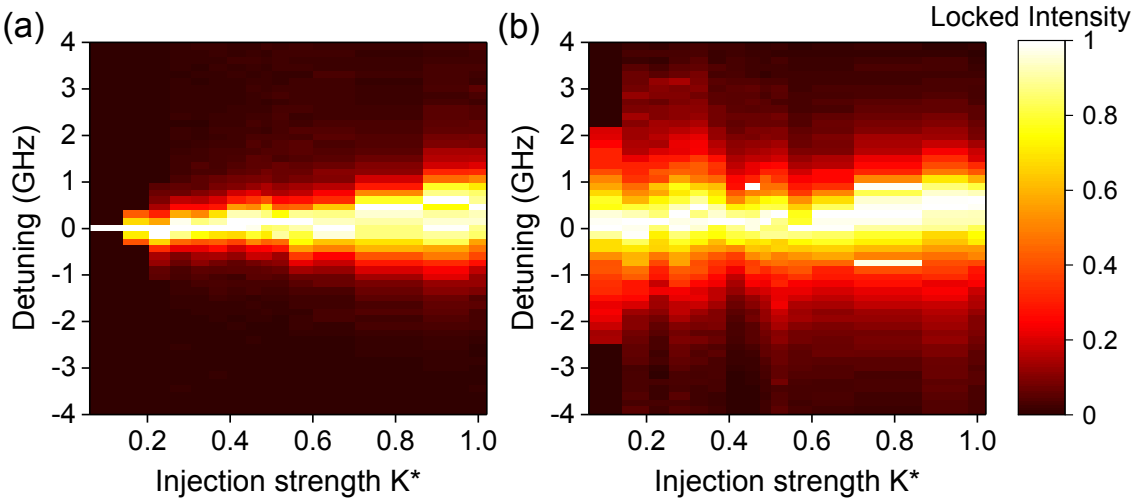

Figure 6.15: Locking maps of microlaser D. Lateral injection of the SM in (a) absence and (b) presence of polarized feedback at $I = 1.5\, I_{\mathrm{th}}$. The color code depicts the normalized intensity of the locked oscillation.

conventional locking experiment the injected master laser power is comparable to the solitary output power of the microlaser ($K \sim 1$). In case of lateral locking the master laser power has to be about two orders of magnitude higher. This is attributed to poor mode matching between the laterally injected field and the axial field of the microlaser cavity.

Figure 6.14 (a) depicts the lateral locking scenario at $K^* = 0.23$. Here one finds an increase of the intensity at the master laser frequency indicating a locking region within a detuning range of ± 0.5 GHz. When increasing the injection strength to $K^* = 0.78$ we record a significantly larger locking region of about ± 1 GHz as illustrated in panel (c).

In the following, we apply axial polarized feedback of the WM as depicted in panel (b) and (d). As previously explained in Fig. 6.13 (b) feedback leads to a strong increase in linewidth of the SM as the WM is stabilized in its lasing oscillation. This effect is counteracted by optical injection into the SM, which not only locks the SM but also reduces the available gain of the WM causing its intensity to drop [Sch19]. In this case we find a significantly higher locking range of ± 1.5 GHz. Increasing the injection strength beyond $K^* = 0.78$ as illustrated in Fig. 6.14 (d) does not further increase the locking range in the presence of feedback (see Fig. 6.15).

To understand the behavior of the microlaser under simultaneous injection and polarized feedback, one has to investigate the full locking map. Figure 6.15 com-

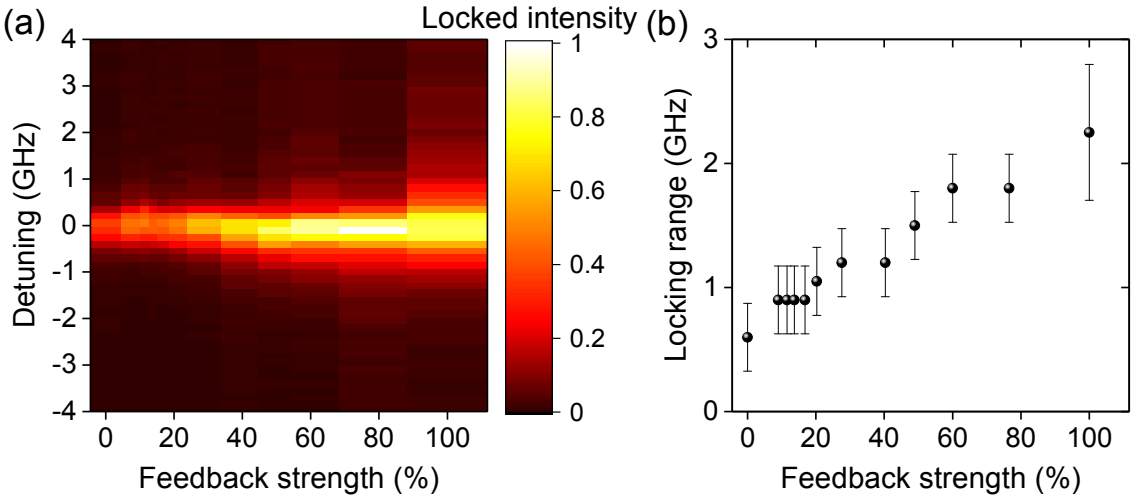

Figure 6.16: (a) Feedback strength series of microlaser D at $K^* = 0.5$. Increasing the amount of polarized feedback increases the locking range which is shown quantitatively in panel (b). 100 % feedback strength refers to the maximum available in the used experimental setup.

pares the two scenarios of lateral locking in (a) absence and (b) presence of polarized feedback. Firstly, one can directly compare lateral and axial injection when examining Fig. 6.15 (a) and Fig. 6.5. In case of lateral injection we find clearly smaller locking ranges. This can be attributed to the smaller effective injection strength under lateral injection. This also explains that the instability region where locking leads to a decrease in the slave laser output power is not reached. Furthermore, the strong asymmetry of the conventional locking map with leads to $\alpha_{\mathrm{IL}}^{1.5I_{\mathrm{th}}} = 2.3 \pm 0.3$ cannot be found in Fig. 6.15 (a). This means that equation 6.4 is not accurate in describing the locking range in the case of lateral injection as we would obtain $\alpha = 0$ for identical slopes of the locking cone. Adding polarized feedback changes the locking map significantly as depicted in Fig. 6.15 (b). Here the locking range increases to a value of about ± 1.5 GHz and is constant for all values of K^*.

This poses the question of how strongly the locking range is influenced by the intensity of the light field coupled back to the microlaser. Figure 6.16 (a) depicts the locking map of a feedback strength series which is taken at an injection strength of $K^* = 0.5$. Increasing feedback leads to an increase of the locking range which is also depicted quantitatively in Fig. 6.16 (b). Therefore, the technique of simultaneous injection and polarized feedback can be used to precisely tune the locking range. This behavior can be understood when examining the locking scenario in the presence of

spontaneous emission noise as discussed for ring-laser gyros in a series of papers by Cresser et al. [Cre82a, Cre82b, Cre82c]. Here the authors make two main claims: Firstly, in the presence of noise the locked region is no longer well defined which is in agreement to finding a partial locking regime in our microlasers. Secondly, in the presence of noise the (partial) locking region is broadened. The latter is explaining the behavior observed in Fig. 6.15 (b). Polarized feedback of the WM leads to a broadening of the SM which can effectively be understood as an increase in spontaneous emission noise. By increasing the amount of feedback also the ratio of spontaneous emission noise and coherent oscillation increases leading to a broadening of the locking cone as described by the above-mentioned theory.

6.2.3 Pulsed injection: storing optical pulses in the external cavity

As previously explained injection into the SM not only locks the latter but also reduces the available gain of the WM while polarized feedback of the WM stabilizes the respective mode. Injection and feedback have opposite influence on the stability of the SM. Thus, it is interesting to study whether pulsed injection is able to drive the microlaser back to a coherent emission state and to relay this effect with feedback.

In order to find the correct operating current of the microlaser for studying this scenario, we have to record the second-order autocorrelation both in the absence and presence of feedback as shown in Fig. 6.17. Panel (a) highlights that the pump condition $I = 1.5\, I_{\mathrm{th}}$ already used previously is ideal. Here the solitary system exhibits lasing with $g^{(2)}(0) < 1.05$ while switching with $g^{(2)}(0) = 1.45$ is found in the presence of WM feedback. When adding continuous wave injection into the SM, $g^{(2)}(0)$ slightly lowers while the temporal dynamics in form of revival peaks is still present. Increasing the pump current to $I = 1.8\, I_{\mathrm{th}}$ we find a different scenario. Even in the solitary state the microlaser exhibits a switching-induced bunching of $g^{(2)}(0) = 1.52$. When applying feedback we find a lowering of the bunching accompanied by a strong decrease of the correlation time from $\tau_{\mathrm{corr,\,noFB}} = (5.3 \pm 0.1)$ ns to $\tau_{\mathrm{corr,\,WMFB}} = (0.34 \pm 0.05)$ ns. Therefore, this observation is related to the SM becoming a thermal emitter as the correlation time is on the order of the coherence time of the microlaser. Consequently, the dynamics that are indicated by revival peaks for lower pump currents vanish making this operating point impractical for pulsed injection experiments.

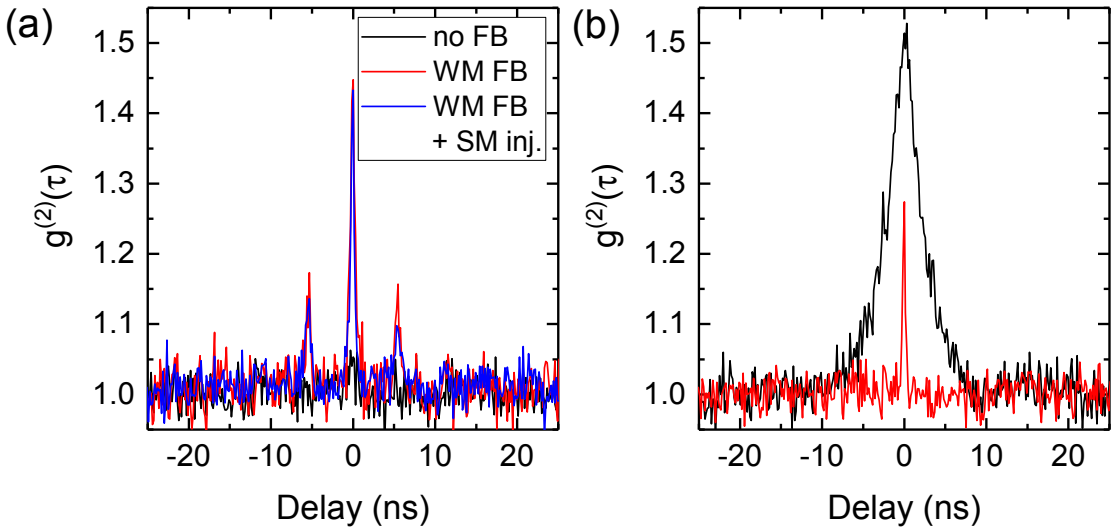

Figure 6.17: (a) Second-order autocorrelation function of the SM of microlaser D taken at $I = 1.5\, I_{\mathrm{th}}$ with and without polarized feedback as well as added pulse injection. (b) Pump current is increased to $I = 1.8\, I_{\mathrm{th}}$ causing all feedback dynamics to vanish.

Figure 6.18 depicts the second-order autocorrelation function in the presence of polarized feedback and pulsed injection taken at the previously used pump condition $I = 1.5\, I_{\mathrm{th}}$. Panel (a) illustrates injection pulses with a repetition time $\tau_{\mathrm{rep}} = 50\,\mathrm{ns}$ and a pulse duration of 3 ns. Even though only the WM is reflected back to the microlaser, one finds bunching peaks at the delays $\pm\tau_{\mathrm{rep}}$. This means that SM injection pulse is reducing the gain of the WM during the pulse duration and causes the SM to become the dominant lasing mode. Moreover, this "turn-on" behavior of the SM is stored by the external cavity, i.e. repeated every round-trip time of $\tau_{\mathrm{FB}} = 5.3\,\mathrm{ns}$. One has to note that the pulse duration should be shorter than the external cavity round-trip time to observe this effect. Figure 6.18 (b) illustrates this issue for a pulse duration of 5 ns. Here the revival peaks of the bunching at τ_{rep} fade as the periods of SM turn-on are overlapping. This indicates that while the revival peaks at zero delay can be related to polarized feedback, the ones at τ_{rep} represent a relayed turn-on of the SM caused by the injected pulse.

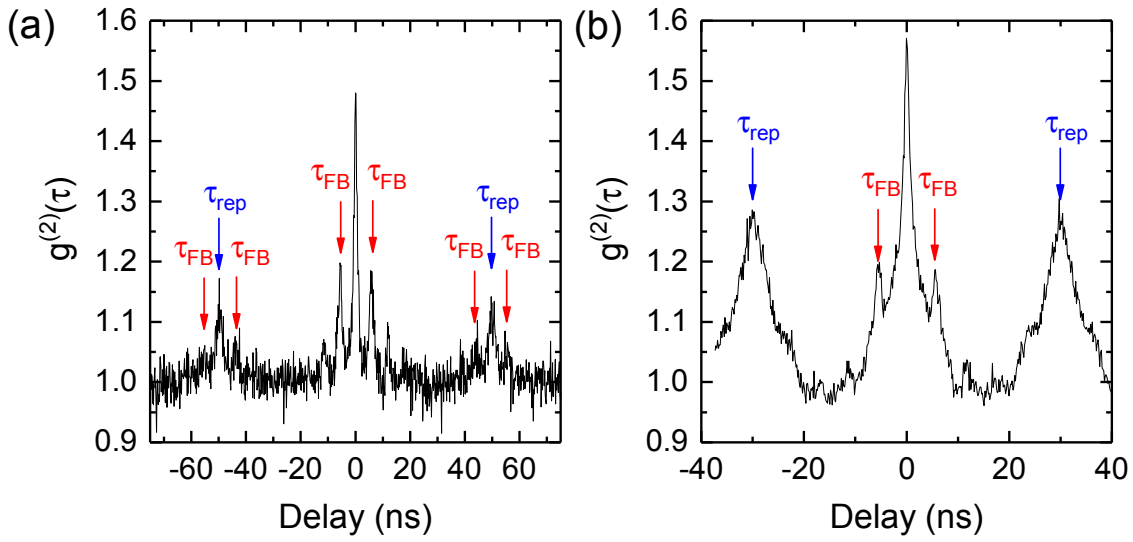

Figure 6.18: (a) Second-order autocorrelation function of microlaser D taken at $I = 1.5\, I_{\mathrm{th}}$ in the presence of polarized feedback and pulsed injection with a repetition timescale $\tau_{\mathrm{rep}} = 50\,\mathrm{ns}$ (3 ns pulse length). (b) The pulse length is increased to 5 ns (repetition timescale is reduced to $\tau_{\mathrm{rep}} = 30\,\mathrm{ns}$)

6.3 Summary of chapter 6

This chapter presented the powerful measurement technique of lateral detection and excitation. First, we demonstrated that lateral detection enables a direct measurement of the modal QD gain. When combined with axial feedback this method can be used to extract the linewidth enhancement factor α, which we demonstrated for the first time for a microlaser. In comparison to established methods of determining α, our novel method not only showed agreement but also unveiled a pump power dependence. The latter is in agreement to a quantum optical model that also explains the reduction of α in the investigated microlaser. Our method is also very suited for future investigations of α in various types of nanolasers that allow lateral access.

In the second part of this section we combine polarized optical feedback with lateral injection locking. We find an increase of the locking range with feedback that is explained by enhanced spontaneous emission noise. Furthermore, pulsed injection into the SM can lock and bring back respective mode to a coherent emission state and relay this effect with feedback. Optimizing the sample structures so that the microlasers are directly situated at the edge of the sample could enable coupling of

the axial laser emission directly via the pillar sidewall into the QD gain medium (using the lateral access). This should result in an incoherent feedback scheme similar to optoelectronic feedback which was realized on-chip in the micropillar laser system [Mun17].

7 Outlook: towards feedback-coupled nanophotonic quantum systems

The findings presented in previous chapters have significantly improved the understanding of nonlinear dynamics and the photon statistics of high-β microlasers at ultra-low light levels.

This outlook first presents results of feedback-coupled micropillar lasers with a controlled number of about 1 to 20 positioned QDs and proposes possible future experiments that could expand research in this field towards the quantum regime of single photons and single emitters.

As discussed in section 4.1 micropillar lasers with site-controlled quantum dots (SCQDs) as the gain medium realized by the so called buried-stressor technique (for more details see [Kag18]) provide an appealing technology platform for feedback experiments with only few emitters in the cavity. This approach combines precise lateral positioning of the QDs in the center of the cavity with the control of the number of emitters in the range of 1 to 20 emitters via the diameter of an integrated oxide aperture in the fabrication process [Kag19]. Figure 7.1 (a) depicts the input-output characteristics of such a microlaser with 15 site-controlled QDs constituting the active medium. The microlaser exhibits a pillar diameter of 5.2 µm, while the oxide aperture that controls the numbers of QDs has a diameter of 975 nm [Kag19]. It has to be noted that these structures are optically pumped. We find that due to the strongly limited gain provided by the low number of positioned QDs only the SM has sufficient gain to overcome the transition to lasing which is indicated by a clear kink in the input-output characteristics. The WM only depicts thermal characteristics and eventually saturates in intensity for high excitation power. This behavior is attributed to the very high mode splitting of SM and WM of 185 µeV. Therefore, the WM is mostly excluded from the following discussion.

Applying optical feedback leads to a clear reduction of the lasing threshold which is

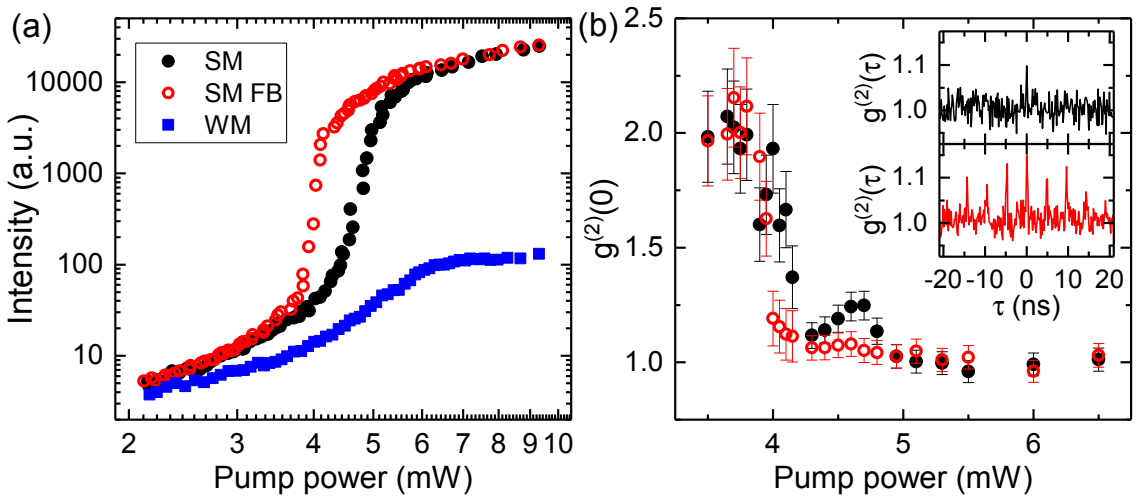

Figure 7.1: (a) Input-output characteristics of an optically pumped microlaser with 15 site-controlled QDs in the active medium. Only the SM exhibits a transition to lasing. (b) Pump power dependence of $g^{(2)}(0)$ of the SM in absence and presence of optical feedback. The inset illustrates a comparison of the full $g^{(2)}$-function for $P = 3.9\,\mathrm{mW}$ exhibiting revival peaks in the presence of feedback (red) which are indicating feedback-induced dynamics.

in contrast to the observations made for the electrically pumped standard micropillar lasers. In order to understand this phenomenon, we have to consider the differences between the two types of samples. The pillar diameter of the optically pumped microlaser is slightly larger and its Q-factor of ~ 8000 is lower than the ones of the electrically pumped counterparts (discussed in chapters 4 to 6) with diameters of 4 to 5 µm and $Q \simeq 20000$, respectively. Consequently, the former enables a higher effective feedback sensitivity due to reduced reflectivity of the top DBR mirror. Even though the number of emitters is reduced by more than one order of magnitude, the microlaser has a moderate β-factor of $\sim 10^{-3}$ which is evident from the strong nonlinear increase of the output power at threshold. This is explained mainly by the rather large mode volume and not too high Q-factor.

Moreover, we find an interesting behavior in the second-order autocorrelation function that is depicted in Fig. 7.1 (b). As expected from the input-output characteristics optical feedback leads to a transition from thermal emission with $g^{(2)}(0) = 2$ to coherent oscillation with $g^{(2)}(0) = 1$ at a lower pump power. Additionally, the switching dynamics are suppressed for $P \sim 4.7\,\mathrm{mW}$. For higher pump powers and for the feedback-coupled case this switching is strongly suppressed as the two modes

diverge in intensity. When investigating the full $g^{(2)}$-function we observe another striking difference to the previously investigated microlasers. As depicted in the inset, feedback-induced revival peaks occur in the transition region to lasing (here: $P = 3.9\,\mathrm{mW}$). In the electrically pumped microlasers these peaks have been only observed significantly above threshold. The dynamics in this interesting intermediate region, which connects the entirely incoherent emission and the pure lasing oscillation, has been the focus of recent research in VCSELs [Wan16]. The observed spiking dynamics in this regime can be enhanced by optical feedback and lead to e.g. low-frequency fluctuations, which could be the cause of the observed revival peaks.

Overall the dynamics of these optically pumped lasers with a low number of QDs is still governed by the moderately low β-factor ultimately resulting in dynamics closer to classical semiconductor lasers. In order to combine high β-factors and a low number of emitters, the diameter of the micropillars has to be reduced and their Q-factor has to be improved for instance by an even higher number of mirror pairs in the DBRs. AlAs/GaAs micropillar cavities with Q-factors exceeding 150000 and standard self-assembled QDs in the active have been demonstrated [Rei07] but it will be very challenging to achieve such high values for micropillars based on site-controlled QDs because of the complex fabrication process including two epitaxial growth steps [Kag18, Kag19].

Moreover, high quality cavities also allow for strong light-matter coupling. A recent work has shown that strong coupling and lasing can coexist if background emitters compensate the cavity losses [Gie17]. Therefore, it would be interesting to explore whether optical feedback could reduce the need for background emitters or increase the coexistence regime for the ultimate goal of pure single emitter lasing.

Finally, recent theoretical works that are based on fully quantum-mechanical calculations suggest a significant impact of single-photon feedback on the emission properties of single quantum emitters and cQED systems. In the regime of weak coupling, optical feedback could be exploited for enhancing the photon entanglement from a biexciton cascade [Hei14] that is present not only in QDs but has also been shown for monolayers of transition metal dichalcogenides [He16]. Additionally, theory has shown that a single-emitter cavity system that operates in the weak coupling regime, can be driven into strong coupling by an external cavity [Car13]. Furthermore, by placing an emitter in a one-dimensional waveguide, quantum in-

terference is expected between the two-level system and the photon-field leading to an increased probability of two-photon emission [Dro19]. Here, a change in the cavity length has to be realized by placing the emitter at different distances from the edge of the waveguide. By covering the regime of feedback-coupled cQED systems, this thesis paves the way towards the aforementioned interesting future steps at the crossroads between nanophotonics, nonlinear dynamics and quantum optics.

Bibliography

[Ack84] G. Acket, D. Lenstra, A. D. Boef and B. Verbeek, *The influence of feedback intensity on longitudinal mode properties and optical noise in index-guided semiconductor lasers*, IEEE Journal of Quantum Electronics **20**, pp. 1163 (1984).

[Ada85] S. Adachi, *GaAs, AlAs, and $Al_xGa_{1-x}As$: Material parameters for use in research and device applications*, Journal of Applied Physics **58**, pp. R1 (1985).

[Agr89] G. Agrawal, *Intensity Dependence of the Linewidth Enhancement Factor and Its Implications for Semiconductor Lasers*, IEEE Photonics Technology Letters **1**, pp. 212 (1989).

[Alb11] F. Albert, C. Hopfmann, S. Reitzenstein, C. Schneider, S. Höfling, L. Worschech, M. Kamp, W. Kinzel, A. Forchel and I. Kanter, *Observing chaos for quantum-dot microlasers with external feedback*, Nature Communications **2**, p. 366 (2011).

[Alf69] Z. I. Alferov, M. V. Andreev, E. I. Korol'kov, E. L. Portnoi and D. N. Tret'yakov, *Injection properties of n-$Al_xGa_{1-x}As$ − p-GaAs heterojunctions*, Soviet Phyics: Semiconductors **2**, p. 1289 (1969).

[Alf70] Z. I. Alferov, V. M. Andreev, D. Z. Garbuzov, Y. V. Zhilyaev, E. P. Morozov, E. L. Portnoi and V. G. Trofim, *Effect of heterostructure parameters on the laser threshold current and the realization of continuous generation at room temperature*, Soviet Physics: Semiconductors **4**, p. 1573 (1970).

[Alf96] Z. I. Alferov, *The history and future of semiconductor heterostructures from the point of view of a Russian scientist*, Physica Scripta **T68**, pp. 32 (1996).

[Bac05] A. G. Baca and C. I. H. Ashby, *Fabrication of GaAs Devices*, The Institution of Electrical Engineers, London (2005).

[Bau04] S. Bauer, O. Brox, J. Kreissl, B. Sartorius, M. Radziunas, J. Sieber, H.-J. Wünsche and F. Henneberger, *Nonlinear dynamics of semiconductor lasers with active optical feedback*, Physical Review E **69**, p. 016206 (2004).

[Bay01] M. Bayer, T. L. Reinecke, F. Weidner, A. Larionov, A. McDonald and A. Forchel, *Inhibition and Enhancement of the Spontaneous Emission of Quantum Dots in Structured Microresonators*, Physical Review Letters **86**, pp. 3168 (2001).

[Ben90] B. R. Bennett, R. A. Soref and J. A. Del Alamo, *Carrier-induced change in refractive index of InP, GaAs and InGaAsP*, IEEE Journal of Quantum Electronics **26**, pp. 113 (1990).

[Bim99] D. Bimberg, M. Grundmann and N. N. Ledentsov, *Quantum Dot Heterostructures*, Wiley VCH (1999).

[Bjö91] G. Björk and Y. Yamamoto, *Analysis of semiconductor microcavity lasers using rate equations*, IEEE Journal of Quantum Electronics **27**, pp. 2386 (1991).

[Bjö94] G. Björk, A. Karlsson and Y. Yamamoto, *Definition of a laser threshold*, Physical Review A **50**, pp. 1675 (1994).

[Bjö05] E. S. Björlin, J. Geske, M. Mehta, J. Piprek and J. E. Bowers, *Temperature dependence of the relaxation resonance frequency of long-wavelength vertical-cavity lasers*, IEEE Photonics Technology Letters **17**, pp. 944 (2005).

[Böc08] C. Böckler, S. Reitzenstein, C. Kistner, R. Debusmann, A. Löffler, T. Kida, S. Höfling, A. Forchel, L. Grenouillet, J. Claudon and J. M. Gérard, *Electrically driven high-Q quantum dot-micropillar cavities*, Applied Physics Letters **92**, p. 091107 (2008).

[Car13] A. Carmele, J. Kabuss, F. Schulze, S. Reitzenstein and A. Knorr, *Single Photon Delayed Feedback: A Way to Stabilize Intrinsic Quantum Cavity Electrodynamics*, Physical Review Letters **110**, p. 013601 (2013).

[CH91] C. J. Chang-Hasnain, J. P. Harbison, G. Hasnain, A. C. V. Lehmen, L. T. Florez and N. G. Stoffel, *Dynamic, polarization, and transverse mode characteristics of vertical cavity surface emitting lasers*, IEEE Journal of Quantum Electronics **27**, pp. 1402 (1991).

[Cha04] Y. Chan, J.-M. Caruge, P. T. Snee and M. G. Bawendi, *Multiexcitonic two-state lasing in a CdSe nanocrystal laser*, Applied Physics Letters **85**, pp. 2460 (2004).

[Cho75] A. Cho and J. Arthur, *Molecular beam epitaxy*, Progress in Solid State Chemistry **10**, pp. 157 (1975).

[Cho13] W. W. Chow and F. Jahnke, *On the physics of semiconductor quantum dots for applications in lasers and quantum optics*, Progress in Quantum Electronics **37**, pp. 109 (2013).

[Cho14] W. W. Chow, F. Jahnke and C. Gies, *Emission properties of nanolasers during the transition to lasing*, Light: Science & Applications **3**, p. e201 (2014).

[Cho16] S. Cho, M. c. v. Humar, N. Martino and S. H. Yun, *Laser Particle Stimulated Emission Microscopy*, Physical Review Letters **117**, p. 193902 (2016).

[CN92] R. Centeno Neelen, D. M. Boersma, M. P. van Exter, G. Nienhuis and J. P. Woerdman, *Spectral filtering within the Schawlow-Townes linewidth of a semiconductor laser*, Physical Review Letters **69**, pp. 593 (1992).

[Coh88] J. S. Cohen, R. R. Drenten and B. H. Verbeeck, *The effect of optical feedback on the relaxation oscillation in semiconductor lasers*, IEEE Journal of Quantum Electronics **24**, pp. 1989 (1988).

[Col93] L. Collot, V. Lefèvre-Seguin, M. Brune, J. M. Raimond and S. Haroche, *Very High-Q Whispering-Gallery Mode Resonances Observed on Fused Silica Microspheres*, Europhysics Letters **23**, pp. 327 (1993).

[Cre82a] J. D. Cresser, *Quantum noise in ring-laser gyros. III. Approximate analytic results in unlocked region*, Physical Review A **26**, pp. 398 (1982).

[Cre82b] J. D. Cresser, D. Hammonds, W. H. Louisell, P. Meystre and H. Risken, *Quantum noise in ring-laser gyros. II. Numerical results*, Physical Review A **25**, pp. 2226 (1982).

[Cre82c] J. D. Cresser, W. H. Louisell, P. Meystre, W. Schleich and M. O. Scully, *Quantum noise in ring-laser gyros. I. Theoretical formulation of problem*, Physical Review A **25**, pp. 2214 (1982).

[Cti10] G. Ctistis, A. Hartsuiker, E. van der Pol, J. Claudon, W. L. Vos and J.-M. Gérard, *Optical characterization and selective addressing of the resonant modes of a micropillar cavity with a white light beam*, Physical Review B **82**, p. 195330 (2010).

[DE14] J. Dreyling-Eschweiler, *A superconducting microcalorimeter for low-flux detection of near-infrared single photons*, dissertation, Universität Hamburg (2014).

[Din16] X. Ding, Y. He, Z.-C. Duan, N. Gregersen, M.-C. Chen, S. Unsleber, S. Maier, C. Schneider, M. Kamp, S. Höfling, C.-Y. Lu and J.-W. Pan, *On-Demand Single Photons with High Extraction Efficiency and Near-Unity Indistinguishability from a Resonantly Driven Quantum Dot in a Micropillar*, Physical Review Letters **116**, p. 020401 (2016).

[Dro19] L. Droenner, N. L. Naumann, E. Schöll, A. Knorr and A. Carmele, *Quantum Pyragas control: Selective control of individual photon probabilities*, Physical Review A **99**, p. 023840 (2019).

[Dru07] D. Drung, C. Assmann, J. Beyer, A. Kirste, M. Peters, F. Ruede and T. Schurig, *Highly Sensitive and Easy-to-Use SQUID Sensors*, IEEE Transactions on Applied Superconductivity **17**, pp. 699 (2007).

[Eis17] G. Eistenstein and D. Bimberg, *Green Photonics and Electronics*, Springer (2017).

[Ell07] B. Ellis, I. Fushman, D. Englund, B. Zhang, Y. Yamamoto and J. Vuckovic, *Dynamics of quantum dot photonic crystal lasers*, Applied Physics Letters **90**, p. 151102 (2007).

[Els84] W. Elsässer, *Power dependence of the linewidth enhancement term in semiconductor lasers*, Applied Physics Letters **44**, pp. 1126 (1984).

[Ern10] T. Erneux and P. Glorieux, *Laser Dynamics*, Cambridge University Press (2010).

[Ext92] M. P. van Exter, W. A. Hamel, J. P. Woerdman and B. R. P. Zeijlmans, *Spectral signature of relaxation oscillations in semiconductor lasers*, IEEE J. Quantum Electron **28**, pp. 1470 (1992).

[Fis00] I. Fischer, Y. Liu and P. Davis, *Synchronization of chaotic semiconductor laser dynamics on subnanosecond time scales and its potential for chaos communication*, Phyiscal Review A **62**, p. 011801 (2000).

[Fle81] M. W. Fleming and A. Mooradian, *Fundamental line broadening of single-mode (GaAl)As diode lasers*, Applied Physics Letters **38**, pp. 511 (1981).

[For07] T. Fordell and A. M. Lindberg, *Experiments on the Linewidth-Enhancement Factor of a Vertical-Cavity Surface-Emitting Laser*, IEEE Journal of Quantum Electronics **43**, pp. 6 (2007).

[Fox06] M. Fox, *Quantum optics: an introduction*, Oxford University Press (2006).

[Gar15] B. Garbin, J. Javaloyes, G. Tissoni and S. Barland, *Topological solitons as addressable phase bits in a driven laser*, Nature Communications **6**, p. 5915 (2015).

[Gay03] B. Gayral and J.-M. Gérard, *Comment on "Single-Mode Spontaneous Emission from a Single Quantum Dot in a Three-Dimensional Microcavity"*, Physical Review Letters **90**, p. 229701 (2003).

[Gay08] B. Gayral and J. M. Gérard, *Photoluminescence experiment on quantum dots embedded in a large Purcell-factor microcavity*, Physical Review B **78**, p. 235306 (2008).

[Gaz13] O. Gazzano, S. M. D. Vasconcellos, C. Arnold, A. Nowak, E. Galopin, I. Sagnes, L. Lanco, A. Lemaitre and P. Senellart, *Bright solid-state sources of indistinguishable single photons*, Nature Communications **4**, p. 1425 (2013).

[Gér98] J. Gérard, B. Sermage, B. Gayral, B. Legrand, E. Costard and V. Thierry-Mieg, *Enhanced Spontaneous Emission by Quantum Boxes in a Monolithic Optical Microcavity*, Physical Review Letters **81**, pp. 1110 (1998).

[Gér99] J. Gérard and B. Gayral, *Strong Purcell effect for InAs quantum boxes in three-dimensional solid-state microcavities*, Journal of Lightwave Technology **17**, pp. 2089 (1999).

[Gér01] J. Gérard and B. Gayral, *InAs quantum dots: artificial atoms for solid-state cavity-quantum electrodynamics*, Physica E: Low-dimensional Systems and Nanostructures **9**, pp. 131 (2001).

[Gie17] C. Gies, F. Gericke, P. Gartner, S. Holzinger, C. Hopfmann, T. Heindel, J. Wolters, C. Schneider, M. Florian, F. Jahnke, S. Höfling, M. Kamp and S. Reitzenstein, *Strong light-matter coupling in the presence of lasing*, Physical Review A **96**, p. 023806 (2017).

[Giu05] G. Giuliani, S. Donati and W. Elsässer, *Measurement of linewidth enhancement factor variations in external cavity semiconductor lasers*, in *European Quantum Electronics Conference, EQEC '05*, p. 13 (2005).

[Giu06] G. Giuliani, S. Donati and W. Elsässer, *Measurement of linewidth enhancement factor of different semiconductor lasers in operating conditions*, Proc. SPIE 6184, Semiconductor Lasers and Laser Dynamics II pp. 61841D–1–61841D–9 (2006).

[Gla63] R. J. Glauber, *The Quantum Theory of Optical Coherence*, Physical Review **130**, pp. 2529 (1963).

[Gon10] Y. Gong, B. Ellis, G. Shambat, T. Sarmiento, J. S. Harris and J. Vuckovic, *Nanobeam photonic crystal cavity quantum dot laser*, Optics Express **18**, pp. 8781 (2010).

[Hag18] N. Haghighi, G. Larisch, R. Rosales, M. Zorn and J. A. Lott, *35 ghz bandwidth with directly current modulated 980 nm oxide aperture single cavity vcsels*, in *2018 IEEE International Semiconductor Laser Conference (ISLC)*, pp. 1–2 (2018).

[Hak75] B. W. Hakki and T. L. Paoli, *Gain spectra in GaAs double heterostructure injection lasers*, Journal of Applied Physics **46**, pp. 1299 (1975).

[Hal62] R. N. Hall, G. E. Fenner, J. D. Kingsley, T. J. Soltys and R. O. Carlson, *Coherent Light Emission From GaAs Junctions*, Phyiscal Review Letters **9**, pp. 366 (1962).

[Ham08] Hamamatsu Photonics, *Guide to streak cameras*, 812 Joko-cho, Higashi-ku, Hamamatsu City, 431-3196, Japan (2008).

[Ham15] P. Hamel, S. Haddadi, F. Raineri, P. Monnier, G. Beaudoin, I. Sagnes, A. Levenson and A. M. Yacomotti, *Spontaneous mirror-symmetry breaking in coupled photonic-crystal nanolaser*, Nature Photonics **9**, p. 311 (2015).

[Ham18] Hamamatsu Photonics, *Universal streak camera C10910 series*, 812 Joko-cho, Higashi-ku, Hamamatsu City, 431-3196, Japan (2018), URL `https://www.hamamatsu.com/resources/pdf/sys/SHSS0016E_C10910s.pdf`.

[Hay70] I. Hayashi and M. B. Panish, *$GaAs - Ga_xAl_{1-x}As$ Heterostructure Injection Lasers which Exhibit Low Thresholds at Room Temperature*, Journal of Applied Physics **41**, pp. 150 (1970).

[Hay16] W. E. Hayenga, H. Garcia-Gracia, H. Hodaei, C. Reimer, R. Morandotti, P. LiKamWa and M. Khajavikhan, *Second-order coherence properties of metallic nanolasers*, Optica **3**, pp. 1187 (2016).

[HB56] R. Hanbury Brown and R. Q. Twiss, *Correlation between photons in two coherent beams of light*, Nature **49**, p. 27 (1956).

[He16] Y.-M. He, O. Iff, N. Lundt, V. Baumann, M. Davanco, K. Srinivasan, S. Höfling and C. Schneider, *Cascaded emission of single photons from the biexciton in monolayered WSe_2*, Nature Communications **7**, p. 13409 (2016).

[Hec17] E. Hecht, *Optics*, Pearson, 5th edition (2017).

[Hei01] T. Heil, I. Fischer, W. Elsäßer and A. Gavrielides, *Dynamics of Semiconductor Lasers Subject to Delayed Optical Feedback: The Short Cavity Regime*, Physical Review Letters **87**, p. 243901 (2001).

[Hei14] S. M. Hein, F. Schulze, A. Carmele and A. Knorr, *Optical feedback-enhanced photon entanglement from a biexciton cascade*, Physical Review Letters **113**, pp. 1 (2014).

[Hen82] C. Henry, *Theory of the linewidth of semiconductor lasers*, IEEE Journal of Quantum Electronics **18**, pp. 259 (1982).

[Hen85] C. Henry, N. Olsson and N. Dutta, *Locking range and stability of injection locked 1.54 um InGaAsp semiconductor lasers*, IEEE Journal of Quantum Electronics **21**, pp. 1152 (1985).

[Her16] B. Herzog, B. Lingnau, M. Kolarczik, Y. Kaptan, D. Bimberg, A. Maaßdorf, U. W. Pohl, R. Rosales, J.-H. Schulze, A. Strittmatter, M. Weyers, U. Woggon, K. Lüdge and N. Owschimikow, *Strong amplitude-phase coupling in submonolayer quantum dots*, Applied Physics Letters **109**, p. 201102 (2016).

[Hol62] N. Holonyak and S. F. Bevacqua, *Coherent (Visible) Light Emission from $Ga(As_{1-x}P_x)$ Junctions*, Applied Physics Letters **1**, pp. 82 (1962).

[Hol18a] S. Holzinger, S. Kreinberg, B. H. Hokr, C. Schneider, S. Höfling, W. W. Chow, X. Porte and S. Reitzenstein, *Determining the linewidth enhancement factor via optical feedback in quantum dot micropillar lasers*, Optics Express **26**, pp. 31363 (2018).

[Hol18b] S. Holzinger, C. Redlich, B. Lingnau, M. Schmidt, M. von Helversen, J. Beyer, C. Schneider, M. Kamp, S. Höfling, K. Lüdge, X. Porte and S. Reitzenstein, *Tailoring the mode-switching dynamics in quantum-dot micropillar lasers via time-delayed optical feedback*, Optics Express **26**, pp. 22457 (2018).

[Hop13] C. Hopfmann, F. Albert, C. Schneider, S. Höfling, M. Kamp, A. Forchel, I. Kanter and S. Reitzenstein, *Nonlinear emission characteristics of quantum-dot micropillar lasers in the presence of polarized optical feedback*, New Journal of Physics **15**, p. 025030 (2013).

[Hua96] Hua Li, T. Lucas, J. McInerney, M. Wright and R. Morgan, *Injection locking dynamics of vertical cavity semiconductor lasers under conventional*

and phase conjugate injection, IEEE Journal of Quantum Electronics **32**, pp. 227 (1996).

[Hui90] R. Hui, A. Mecozzi, A. D'Ottavi and P. Spano, *Novel measurement technique of alpha factor in DFB semiconductor lasers by injection locking*, Electronics Letters **26**, pp. 997 (1990).

[Hum15] P. C. Humphreys, B. J. Metcalf, T. Gerrits, T. Hiemstra, A. E. Lita, J. Nunn, S. W. Nam, A. Datta, W. S. Kolthammer and I. A. Walmsley, *Tomography of photon-number resolving continuous-output detectors*, New Journal of Physics **17**, p. 103044 (2015).

[Ima17] *Laser diode market: Global industry trends, share, size, growth, opportunity and forecast 2018-2023*, `https://www.imarcgroup.com/laser-diode-market` (2017), accessed: March 18th, 2019.

[Irw05] K. D. Irwin and G. C. Hilton, *Cryogenic Particle Detection*, chapter Transition-Edge Sensors, pp. 63–149, Springer, Heidelberg (2005).

[Jag18] S. T. Jagsch, N. V. Triviño, F. Lohof, G. Callsen, S. Kalinowski, I. M. Rousseau, R. Barzel, J.-F. Carlin, F. Jahnke, R. Butté, C. Gies, A. Hoffmann, N. Grandjean and S. Reitzenstein, *A quantum optical study of thresholdless lasing features in high-β nitride nanobeam cavities*, Nature Communications **9**, p. 564 (2018).

[Jeo06] Y. D. Jeong, J. S. Cho, Y. H. Won, H. J. Lee and H. Yoo, *All-optical flip-flop based on the bistability of injection locked Fabry-Perot laser diode.*, Optics express **14**, pp. 4058 (2006).

[Joh01] J. C. Johnson, H. Yan, R. D. Schaller, L. H. Haber, R. J. Saykally and P. Yang, *Single Nanowire Lasers*, The Journal of Physical Chemistry B **105**, pp. 11387 (2001).

[Joh08] J. Johansen, S. Stobbe, I. S. Nikolaev, T. Lund-Hansen, P. T. Kristensen, J. M. Hvam, W. L. Vos and P. Lodahl, *Size dependence of the wavefunction of self-assembled InAs quantum dots from time-resolved optical measurements*, Physical Review B **77**, p. 073303 (2008).

[Jum14] L. Jumpertz, M. Carras, K. Schires and F. Grillot, *Regimes of external optical feedback in 5.6 μm distributed feedback mid-infrared quantum cascade lasers*, Applied Physics Letters **105** (2014).

[Jum16] L. Jumpertz, F. Michel, R. Pawlus, W. Elsässer, K. Schires, M. Carras and F. Grillot, *Measurements of the linewidth enhancement factor of mid-infrared quantum cascade lasers by different optical feedback techniques*, AIP Advances **6**, p. 015212 (2016).

[Kag18] A. Kaganskiy, F. Gericke, T. Heuser, T. Heindel, X. Porte and S. Reitzenstein, *Micropillars with a controlled number of site-controlled quantum dots*, Applied Physics Letters **112**, p. 071101 (2018).

[Kag19] A. Kaganskiy, S. Kreinberg, X. Porte and S. Reitzenstein, *Micropillar lasers with site-controlled quantum dots as active medium*, Optica **6**, pp. 404 (2019).

[Kar09] M. Karl, B. Kettner, S. Burger, F. Schmidt, H. Kalt and M. Hetterich, *Dependencies of micro-pillar cavity quality factors calculated with finite element methods*, Optics Express **17**, pp. 1144 (2009).

[Kav07] A. V. Kavokin, J. J. Baumberg, G. Malpuech and F. P. Laussy, *Microcavities*, Oxford University Press (2007).

[Kel12] B. Kelleher, S. P. Hegarty and G. Huyet, *Optically injected lasers: The transition from class B to class A lasers*, Physical Review E **86**, p. 066206 (2012).

[Kha12] M. Khajavikhan, A. Simic, M. Katz, J. H. Lee, B. Slutsky, A. Mizrahi, V. Lomakin and Y. Fainman, *Thresholdless nanoscale coaxial lasers*, Nature **482**, pp. 204 (2012).

[Khi34] A. Khintchine, *Korrelationstheorie der stationären stochastischen Prozesse*, Mathematische Annalen **109**, pp. 604 (1934).

[Kle06] E. Klein, N. Gross, M. Rosenbluh, W. Kinzel, L. Khaykovich and I. Kanter, *Stable isochronal synchronization of mutually coupled chaotic lasers*, Physical Review E **73**, p. 066214 (2006).

[Kre17] S. Kreinberg, W. W. Chow, J. Wolters, C. Schneider, C. Gies, F. Jahnke, S. Höfling, M. Kamp and S. Reitzenstein, *Emission from quantum-dot high-β microcavities: transition from spontaneous emission to lasing and the effects of superradiant emitter coupling*, Light: Science & Applications **6**, p. e17030 (2017).

[Kre19] S. Kreinberg, X. Porte, D. Schicke, B. Lingnau, C. Schneider, S. Höfling, I. Kanter, K. Lüdge and S. Reitzenstein, *Mutual coupling and synchronization of optically coupled quantum-dot micropillar lasers at ultra-low light levels*, Nature Communications **10**, p. 1539 (2019).

[Kuc93] D. M. Kuchta, J. Gamelin, J. D. Walker, J. Lin, K. Y. Lau, J. S. Smith, M. Hong and J. P. Mannaerts, *Relative intensity noise of vertical cavity surface emitting lasers*, Applied Physics Letters **62**, pp. 1194 (1993).

[Lan80] R. Lang and K. Kobayashi, *External optical feedback effects on semiconductor injection laser properties*, IEEE Journal of Quantum Electronics **16**, pp. 347 (1980).

[Lan82] R. Lang, *Injection locking properties of a semiconductor laser*, IEEE Journal of Quantum Electronics **18**, pp. 976 (1982).

[Len84] D. Lenstra, M. V. Vaalen and B. Jaskorzyńska, *On the theory of a single-mode laser with weak optical feedback*, Physica B+C **125**, pp. 255 (1984).

[Len85] D. Lenstra, B. Verbeek and A. D. Boef, *Coherence collapse in single-mode semiconductor lasers due to optical feedback*, IEEE Journal of Quantum Electronics **21**, pp. 674 (1985).

[Ler12] M. Lermer, N. Gregersen, F. Dunzer, S. Reitzenstein, S. Höfling, J. Mørk, L. Worschech, M. Kamp and A. Forchel, *Bloch-Wave Engineering of Quantum Dot Micropillars for Cavity Quantum Electrodynamics Experiments*, Physical Review Letters **108**, p. 057402 (2012).

[Lev95] A. M. Levine, G. H. M. van Tartwijk, D. Lenstra and T. Erneux, *Diode lasers with optical feedback: Stability of the maximum gain mode*, Physical Review A **52**, pp. R3436 (1995).

[Ley13] H. A. M. Leymann, C. Hopfmann, F. Albert, A. Foerster, M. Khanbekyan, C. Schneider, S. Höfling, A. Forchel, M. Kamp, J. Wiersig and S. Reitzenstein, *Intensity fluctuations in bimodal micropillar lasers enhanced by quantum-dot gain competition*, Physical Review A **87**, p. 053819 (2013).

[Ley17] H. A. M. Leymann, D. Vorberg, T. Lettau, C. Hopfmann, C. Schneider, M. Kamp, S. Höfling, R. Ketzmerick, J. Wiersig, S. Reitzenstein and A. Eckardt, *Pump-Power-Driven Mode Switching in a Microcavity Device and Its Relation to Bose-Einstein Condensation*, Physical Review X **7**, p. 021045 (2017).

[Lin12] B. Lingnau, K. Lüdge, W. W. Chow and E. Schöll, *Failure of the α factor in describing dynamical instabilities and chaos in quantum-dot lasers*, Physical Review E **86**, p. 065201 (2012).

[Lin15] B. Lingnau and K. Lüdge, *Analytic Characterization of the Dynamic Regimes of Quantum-Dot Lasers*, Photonics **2**, pp. 402 (2015).

[Lit08] A. E. Lita, A. J. Miller and S. W. Nam, *Counting near-infrared single-photons with 95% efficiency*, Optics Express **16**, p. 3032 (2008).

[Lit10] A. E. Lita, B. Calkins, L. A. Pellouchoud, A. J. Miller and S. Nam, *Superconducting transition-edge sensors optimized for high-efficiency photon-number resolving detectors*, Proceedings SPIE: Advanced Photon Counting Techniques **4**, p. 7681 (2010).

[Liu01] G. Liu, X. Jin and S. L. Chuang, *Measurement of linewidth enhancement factor of semiconductor lasers using an injection-locking technique*, IEEE Photonics Technology Letters **13**, pp. 430 (2001).

[LL13] A. Lamas-Linares, B. Calkins, N. A. Tomlin, T. Gerrits, A. E. Lita, J. Beyer, R. P. Mirin and S. Woo Nam, *Nanosecond-scale timing jitter for single photon detection in transition edge sensors*, Applied Physics Letters **102**, p. 231117 (2013).

[Löf08] A. Löffler, *Selbstorganisiertes Wachstum von (Ga)InAs/GaAs-Quantenpunkten und Entwicklung von Mikroresonatoren höchster*

Güte für Experimente zur starken Exziton-Photon-Kopplung, dissertation, Julius-Maximilians-Universität Würzburg (2008).

[Loh18] F. Lohof, R. Barzel, P. Gartner and C. Gies, *Delayed Transition to Coherent Emission in Nanolasers with Extended Gain Media*, Physical Review Applied **10**, p. 054055 (2018).

[Lor07] M. Lorke, F. Jahnke and W. W. Chow, *Excitation dependences of gain and carrier-induced refractive index change in quantum-dot lasers*, Applied Physics Letters **90**, p. 051112 (2007).

[Lot00] J. A. Lott, N. N. Ledentsov, V. M. Ustinov, N. A. Maleev, A. E. Zhukov, A. R. Kovsh, M. V. Maximov, B. V. Volovik, Z. I. Alferov and D. Bimberg, *InAs-InGaAs quantum dot VCSELs on GaAs substrates emitting at 1.3 μm*, Electronics Letters **36**, pp. 1384 (2000).

[Lou00] R. Loudon, *The Quantum Theory of Light*, Oxford University Press, 3rd edition (2000).

[Lüd09] K. Lüdge and E. Schöll, *Quantum-Dot Lasers—Desynchronized Nonlinear Dynamics of Electrons and Holes*, IEEE Journal of Quantum Electronics **45**, pp. 1396 (2009).

[Lüd11] K. Lüdge, *Nonlinear Laser Dynamics*, Wiley VCH (2011).

[Lüd12] K. Lüdge, B. Lingnau, C. Otto and E. Schöll, *Understanding Electrical and Optical Modulation Properties of Semiconductor Quantum-Dot Lasers in Terms of Their Turn-On Dynamics*, Nonlinear Phenomena in Complex Systems **15**, pp. 350 (2012).

[Ma19] R.-M. Ma and R. F. Oulton, *Applications of nanolasers*, Nature Nanotechnology **14**, pp. 12 (2019).

[Mai60] T. H. Maiman, *Optical and Microwave-Optical Experiments in Ruby*, Phyiscal Review Letters **4**, pp. 564 (1960).

[Mal06] E. Malić, K. J. Ahn, M. J. P. Bormann, P. Hövel, E. Schöll, A. Knorr, M. Kuntz and D. Bimberg, *Theory of relaxation oscillations in semiconductor quantum dot lasers*, Applied Physics Letters **89**, p. 101107 (2006).

[McC92] S. L. McCall, A. F. J. Levi, R. E. Slusher, S. J. Pearton and R. A. Logan, *Whispering-gallery mode microdisk lasers*, Applied Physics Letters **60**, pp. 289 (1992).

[Mic00] P. Michler, A. Kiraz, C. Becher, W. V. Schoenfeld, P. M. Petroff, L. Zhang, E. Hu and A. Imamoglu, *A Quantum Dot Single-Photon Turnstile Device*, Science **290**, pp. 2282 (2000).

[Mic09] P. Michler, *Single Semiconductor Quantum Dots*, Springer (2009).

[Mic13] R. Michalzik, *VCSELs: Fundamentals, Technology and Applications of Vertical-Cavity Surface-Emitting Lasers*, Springer (2013).

[Mil11] A. J. Miller, A. E. Lita, B. Calkins, I. Vayshenker, S. M. Gruber and S. W. Nam, *Compact cryogenic self-aligning fiber-to-detector coupling with losses below one percent*, Optics Express **19**, pp. 9102 (2011).

[Miy89] Y. Miyake and M. Asada, *Spectral Characteristics of Linewidth Enhancement Factor α of Multidimensional Quantum Wells*, Japanese Journal of Applied Physics **28**, p. 1280 (1989).

[Moo18] G. Moody, M. Segnon, I. Sagnes, R. Braive, A. Beveratos, I. Robert-Philip, N. Belabas, F. Jahnke, K. L. Silverman, R. P. Mirin, M. J. Stevens and C. Gies, *Delayed formation of coherence in the emission dynamics of high-Q nanolasers*, Optica **5**, pp. 395 (2018).

[Mør90] J. Mørk, J. Mark and B. Tromborg, *Route to chaos and competition between relaxation oscillations for a semiconductor laser with optical feedback*, Physical Review Letters **65**, pp. 1999 (1990).

[Mør92] J. Mørk, B. Tromborg and J. Mark, *Chaos in semiconductor lasers with optical feedback: theory and experiment*, IEEE Journal of Quantum Electronics **28**, pp. 93 (1992).

[Mun17] P. Munnelly, B. Lingnau, M. M. Karow, T. Heindel, M. Kamp, S. Höfling, K. Lüdge, C. Schneider and S. Reitzenstein, *On-chip optoelectronic feedback in a micropillar laser-detector assembly*, Optica **4**, p. 303 (2017).

[Mus15] A. Musiał, C. Hopfmann, T. Heindel, C. Gies, M. Florian, H. A. M. Leymann, A. Foerster, C. Schneider, F. Jahnke, S. Höfling, M. Kamp and S. Reitzenstein, *Correlations between axial and lateral emission of coupled quantum dot–micropillar cavities*, Physical Review B **91**, p. 205310 (2015).

[Nak91] H. Nakajima and J. . Bouley, *Observation of power dependent linewidth enhancement factor in 1.55 μm strained quantum well lasers*, Electronics Letters **27**, pp. 1840 (1991).

[Nat62] M. I. Nathan, W. P. Dumke, G. Burns, F. H. Dill and G. Lasher, *Stimulated Emission of Radiation from GaAs p-n Junctions*, Applied Physics Letters **1**, pp. 62 (1962).

[Nau03] A. V. Naumenko, N. A. Loiko, M. Sondermann and T. Ackemann, *Description and analysis of low-frequency fluctuations in vertical-cavity surface-emitting lasers with isotropic optical feedback by a distant reflector*, Phyiscal Review A **68**, p. 033805 (2003).

[Nod06] S. Noda, *Seeking the Ultimate Nanolaser*, Science **314**, pp. 260 (2006).

[Oht13] J. Ohtsubo, *Semiconductor Lasers: Stability, Instability and Chaos*, Springer (2013).

[Osi87] M. Osiński and J. Buus, *Linewidth broadening factor in semiconductor lasers–An overview*, IEEE Journal of Quantum Electronics **23**, pp. 9 (1987).

[Ott10] C. Otto, K. Lüdge and E. Schöll, *Modeling quantum dot lasers with optical feedback: sensitivity of bifurcation scenarios*, physica status solidi (b) **247**, pp. 829 (2010).

[Pai99] O. Painter, R. K. Lee, A. Scherer, A. Yariv, J. D. O'Brien, P. D. Dapkus and I. Kim, *Two-Dimensional Photonic Band-Gap Defect Mode Laser*, Science **284**, pp. 1819 (1999).

[Pet86] I. Petitbon, P. Gallion, G. Debarge and C. Chabran, *Locking bandwidth and relaxation oscillations of an injection-locked semiconductor laser*, Electronics Letters **22**, pp. 889 (1986).

[Pet88] I. Petitbon, P. Gallion, G. Debarge and C. Chabran, *Locking bandwidth and relaxation oscillations of an injection-locked semiconductor laser*, IEEE Journal of Quantum Electronics **24**, pp. 148 (1988).

[Por14] X. Porte, M. C. Soriano and I. Fischer, *Similarity properties in the dynamics of delayed-feedback semiconductor lasers*, Physical Review A **89**, p. 023822 (2014).

[Pur46] E. M. Purcell, *Spontaneous emission probabilities at radio frequencies*, Proceedings of the American Physical Society **69**, p. 681 (1946).

[Rai37] D. Raikov, *On the decomposition of Poisson laws*, Comptes Rendus de l'Academie des Sciences de l'URSS **14**, pp. 9 (1937).

[Red16] C. Redlich, B. Lingnau, S. Holzinger, E. Schlottmann, S. Kreinberg, C. Schneider, M. Kamp, S. Höfling, J. Wolters, S. Reitzenstein and K. Lüdge, *Mode-switching induced super-thermal bunching in quantum-dot microlasers*, New Journal of Physics **18**, p. 063011 (2016).

[Rei04] J. P. Reithmaier, G. Sek, A. Löffler, C. Hofmann, S. Kuhn, S. Reitzenstein, L. V. Keldysh, V. D. Kulakovskii, T. L. Reinecke and A. Forchel, *Strong coupling in a single quantum dot-semiconductor microcavity system.*, Nature **432**, pp. 197 (2004).

[Rei07] S. Reitzenstein, C. Hofmann, A. Gorbunov, M. Strauß, S. H. Kwon, C. Schneider, A. Löffler, S. Höfling, M. Kamp and A. Forchel, *AlAs/GaAs micropillar cavities with quality factors exceeding 150.000*, Applied Physics Letters **90**, p. 251109 (2007).

[Rei08] S. Reitzenstein, T. Heindel, C. Kistner, A. Rahimi-Iman, C. Schneider, S. Höfling and A. Forchel, *Low threshold electrically pumped quantum dot-micropillar lasers*, Applied Physics Letters **93**, p. 061104 (2008).

[Rei11] S. Reitzenstein, T. Heindel, C. Kistner, F. Albert, T. Braun, C. Hopfmann, P. Mrowinski, M. Lermer, C. Schneider, S. Höfling, M. Kamp and A. Forchel, *Electrically Driven Quantum Dot Micropillar Light Sources*, IEEE Journal of Selected Topics in Quantum Electronics **17**, pp. 1670 (2011).

[Ric94] P. R. Rice and H. J. Carmichael, *Photon statistics of a cavity-QED laser: A comment on the laser–phase-transition analogy*, Physical Review A **50**, pp. 4318 (1994).

[Riv99] T. Rivera, J.-P. Debray, J. M. Gérard, B. Legrand, L. Manin-Ferlazzo and J. L. Oudar, *Optical losses in plasma-etched AlGaAs microresonators using reflection spectroscopy*, Applied Physics Letters **74**, pp. 911 (1999).

[Ros17] R. Rosales, M. Zorn and J. A. Lott, *30-GHz Bandwidth With Directly Current-Modulated 980-nm Oxide-Aperture VCSELs*, IEEE Photonics Technology Letters **29**, pp. 2107 (2017).

[Sal95] T. E. Sale, *Cavity and reflector design for vertical cavity surface emitting lasers*, IEE Proceedings - Optoelectronics **142**, pp. 37 (1995).

[San94] T. Sano, *Antimode dynamics and chaotic itinerancy in the coherence collapse of semiconductor lasers with optical feedback*, Physical Review A **50**, pp. 2719 (1994).

[San02] C. Santori, D. Fattal, J. Vučković, G. S. Solomon and Y. Yamamoto, *Indistinguishable photons from a single-photon device*, Nature **419**, pp. 594 (2002).

[Sar74] M. Sargent, M. Scully and W. Lamb, *Laser Physics*, Addison-Wesley, London, 2nd edition (1974).

[Sch58] A. L. Schawlow and C. H. Townes, *Infrared and Optical Masers*, Physical Review **112**, pp. 1940 (1958).

[Sch94] H. Schneider, J. D. Ralston, E. P. O'Reilly, S. Weisser and E. C. Larkins, *Gain switching in high-speed semiconductor lasers: Intermediate-signal analysis*, Applied Physics Letters **65**, pp. 661 (1994).

[Sch05] E. Schöll, A. G. Balanow, N. B. Janson and A. Neiman, *Controlling Stochastic Oscillations Close to a Hopf Bifurcation by Time-Delayed Feedback*, Stochastics and Dynamics **05**, pp. 281 (2005).

[Sch10] J. A. Schuller, E. S. Barnard, W. Cai, Y. C. Jun, J. S. White and M. L. Brongersma, *Plasmonics for extreme light concentration and manipulation*, Nature Materials **9**, p. 193 (2010).

[Sch11] C. Schneider, *Konzepte zur skalierbaren Realisierung von effizienten, halbleiterbasierten Einzelphotonenquellen*, dissertation, Julius-Maximilians-Universität Würzburg (2011).

[Sch13] A. Schlehahn, F. Albert, C. Schneider, S. Höfling, S. Reitzenstein, J. Wiersig and M. Kamp, *Mode selection in electrically driven quantum dot microring cavities*, Optics Express **21**, pp. 15951 (2013).

[Sch16] E. Schlottmann, S. Holzinger, B. Lingnau, K. Lüdge, C. Schneider, M. Kamp, S. Höfling, J. Wolters and S. Reitzenstein, *Injection Locking of Quantum-Dot Microlasers Operating in the Few-Photon Regime*, Physical Review Applied **6**, p. 044023 (2016).

[Sch18a] E. Schlottmann, M. von Helversen, H. A. M. Leymann, T. Lettau, F. Krüger, M. Schmidt, C. Schneider, M. Kamp, S. Höfling, J. Beyer, J. Wiersig and S. Reitzenstein, *Exploring the Photon-Number Distribution of Bimodal Microlasers with a Transition Edge Sensor*, Physical Review Applied **9**, p. 064030 (2018).

[Sch18b] M. Schmidt, M. v. Helversen, M. López, F. Gericke, E. Schlottmann, T. Heindel, S. Kück, S. Reitzenstein and J. Beyer, *Photon-Number-Resolving Transition-Edge Sensors for the Metrology of Quantum Light Sources*, Journal of Low Temperature Physics **193**, pp. 1243 (2018).

[Sch19] E. Schlottmann, D. Schicke, F. Krüger, B. Lingnau, C. Schneider, S. Höfling, K. Lüdge, X. Porte and S. Reitzenstein, *Stochastic Polarization Switching Induced by Optical Injection in Bimodal Quantum-Dot Micropillar Lasers*, Manuscript in preparation (2019).

[Sci15] M. Sciamanna and K. A. Shore, *Physics and applications of laser diode chaos*, Nature Photonics **9**, pp. 151 (2015).

[Sęk06] G. Sęk, P. Poloczek, K. Ryczko, J. Misiewicz, A. Löffler, J. P. Reithmaier and A. Forchel, *Photoreflectance determination of the wetting layer thick-*

ness in the $In_xGa_{1-x}As/GaAs$ quantum dot system for a broad indium content range of 0.3-1, Journal of Applied Physics **100**, p. 103529 (2006).

[Sel16] F. Selmi, S. Coulibaly, Z. Loghmari, I. Sagnes, G. Beaudoin, M. G. Clerc and S. Barbay, *Spatiotemporal Chaos Induces Extreme Events in an Extended Microcavity Laser*, Physical Review Letters **116**, p. 013901 (2016).

[Sha48] C. E. Shannon, *A mathematical theory of communication*, The Bell System Technical Journal **27**, pp. 379 (1948).

[Sie86] A. E. Siegman, *Lasers*, University Science Books (1986).

[Sko98] M. S. Skolnick, T. A. Fisher and D. M. Whittaker, *Strong coupling phenomena in quantum microcavity structures*, Semiconductor Science and Technology **13**, pp. 645 (1998).

[SM95] M. San Miguel, Q. Feng and J. V. Moloney, *Light-polarization dynamics in surface-emitting semiconductor lasers*, Physical Review A **52**, pp. 1728 (1995).

[Sok12] G. S. Sokolovskii, V. V. Dudelev, E. D. Kolykhalova, A. G. Deryagin, M. V. Maximov, A. M. Nadtochiy, V. I. Kuchinskii, S. S. Mikhrin, D. A. Livshits, E. A. Viktorov and T. Erneux, *Nonvanishing turn-on delay in quantum dot lasers*, Applied Physics Letters **100**, p. 081109 (2012).

[Soo13] E. Sooudi, C. de Dios, J. G. McInerney, G. Huyet, F. Lelarge, K. Merghem, R. Rosales, A. Martinez, A. Ramdane and S. P. Hegarty, *A Novel Scheme for Two-Level Stabilization of Semiconductor Mode-Locked Lasers Using Simultaneous Optical Injection and Optical Feedback*, IEEE Journal of Selected Topics in Quantum Electronics **19**, pp. 1101208 (2013).

[Sor13] M. Soriano, J. García-Ojalvo, C. Mirasso and I. Fischer, *Complex photonics: Dynamics and applications of delay-coupled semiconductors lasers*, Reviews of Modern Physics **85**, pp. 421 (2013).

[Ste12] G. A. Steudle, S. Schietinger, D. Höckel, S. N. Dorenbos, I. E. Zadeh, V. Zwiller and O. Benson, *Measuring the quantum nature of light with a single source and a single detector*, Physical Review A **86**, p. 053814 (2012).

[Str38] I. N. Stranski and L. Krastanow, *Zur Theorie der orientierten Ausscheidung von Ionenkristallen aufeinander*, Abhandlungen der Mathematisch-Naturwissenschaftlichen Klasse IIb. Akademie der Wissenschaften Wien **146**, pp. 797 (1938).

[Tar95a] G. H. M. van Tartwijk and D. Lenstra, *Semiconductor lasers with optical injection and feedback*, Quantum and Semiclassical Optics: Journal of the European Optical Society Part B **7**, pp. 87 (1995).

[Tar95b] G. H. M. V. Tartwijk, A. M. Levine and D. Lenstra, *Sisyphus effect in semiconductor lasers with optical feedback*, IEEE Journal of Selected Topics in Quantum Electronics **1**, pp. 466 (1995).

[Tho04] J. J. Thorn, M. S. Neel, V. W. Donato, G. S. Bergreen, R. E. Davies and M. Beck, *Observing the quantum behavior of light in an undergraduate laboratory*, American Journal of Physics **72**, pp. 1210 (2004).

[Tka86] R. Tkach and A. Chraplyvy, *Regimes of feedback effects in 1.5-μm distributed feedback lasers*, Journal of Lightwave Technology **4**, pp. 1655 (1986).

[Tof92] Z. Toffano, A. Destrez, C. Birocheau and L. Hassine, *New linewidth enhancement determination method in semiconductor lasers based on spectrum analysis above and below threshold*, Electronics Letters **28**, pp. 9 (1992).

[Too15] J. P. Toomey, D. M. Kane, C. McMahon, A. Argyris and D. Syvridis, *Integrated semiconductor laser with optical feedback: transition from short to long cavity regime*, Optics Express **23**, pp. 18754 (2015).

[Tre85] J. R. Tredicce, F. T. Arecchi, G. L. Lippi and G. P. Puccioni, *Instabilities in lasers with an injected signal*, Journal of the Optical Society of America B **2**, pp. 173 (1985).

[Uch08] A. Uchida, K. Amano, M. Inoue, K. Hirano, S. Naito, H. Someya, I. Oowada, T. Kurashige, M. Shiki, S. Yoshimori, K. Yoshimura and P. Davis, *Fast physical random bit generation with chaotic semiconductor lasers*, Nature Photonics **2**, pp. 728 (2008).

[Ulu00] G. Ulu, A. V. Sergienko and M. S. Ünlü, *Influence of hot-carrier luminescence from avalanche photodiodes on time-correlated photon detection*, Optics Letters **25**, pp. 758 (2000).

[Uns16] S. Unsleber, Y.-M. He, S. Gerhardt, S. Maier, C.-Y. Lu, J.-W. Pan, N. Gregersen, M. Kamp, C. Schneider and S. Höfling, *Highly indistinguishable on-demand resonance fluorescence photons from a deterministic quantum dot micropillar device with 74% extraction efficiency*, Optics Express **24**, pp. 8539 (2016).

[Vah83] K. Vahala, L. C. Chiu, S. Margalit and A. Yariv, *On the linewidth enhancement factor β in semiconductor injection lasers*, Applied Physics Letters **42**, pp. 631 (1983).

[Vah03] K. J. Vahala, *Optical microcavities*, Nature **424**, p. 839 (2003).

[Vas00] P. P. Vasil'ev, I. H. White and J. Gowar, *Fast phenomena in semiconductor lasers*, Reports on Progress in Physics **63**, pp. 1997 (2000).

[Vaz06] J. M. M. Vazquez, H. H. Nilsson, J. Z. Zhang and I. Galbraith, *Linewidth Enhancement Factor of Quantum-Dot Optical Amplifiers*, IEEE Journal of Quantum Electronics **42**, pp. 986 (2006).

[Vil09] A. Villafranca, A. Villafranca, G. Giuliani and I. Garces, *Mode-Resolved Measurements of the Linewidth Enhancement Factor of a Fabry-Perot Laser*, IEEE Photonics Technology Letters **21**, pp. 1256 (2009).

[Vir12] M. Virte, K. Panajotov, H. Thienpont and M. Sciamanna, *Deterministic polarization chaos from a laser diode*, Nature Photonics **7**, pp. 1 (2012).

[Vur01] I. Vurgaftman, J. R. Meyer and L. R. Ram-Mohan, *Band parameters for III–V compound semiconductors and their alloys*, Journal of Applied Physics **89**, pp. 5815 (2001).

[Wan16] C. Wang, K. Schires, M. Osiński, P. J. Poole and F. Grillot, *Thermally insensitive determination of the linewidth broadening factor in nanostructured semiconductor lasers using optical injection locking*, Scientific Reports **6**, p. 27825 (2016).

[Wie05] S. Wieczorek, B. Krauskopf, T. B. Simpson and D. Lenstra, *The dynamical complexity of optically injected semiconductor lasers*, Physics Reports **416**, pp. 1 (2005).

[Wil99] M. B. Willemsen, M. U. F. Khalid, M. P. van Exter and J. P. Woerdman, *Polarization Switching of a Vertical-Cavity Semiconductor Laser as a Kramers Hopping Problem*, Physical Review Letters **82**, pp. 4815 (1999).

[Yam91] Y. Yamamoto, S. MacHida and G. Björk, *Microcavity semiconductor laser with enhanced spontaneous emission*, Physical Review A **44**, pp. 657 (1991).

[Yam00] Y. Yamamoto, T. Tassone and H. Cao, *Semiconductor Cavity Quantum Electrodynamics*, Springer (2000).

[Yan17] Z. Yang, M. Pelton, I. Fedin, D. V. Talapin and E. Waks, *A room temperature continuous-wave nanolaser using colloidal quantum wells*, Nature Communications **8**, p. 143 (2017).

[Yok92] H. Yokoyama, K. Nishi, T. Anan, Y. Nambu, S. D. Brorson, E. P. Ippen and M. Suzuki, *Controlling spontaneous emission and threshold-less laser oscillation with optical microcavities*, Optical and Quantum Electronics **24**, pp. S245 (1992).

[Yu04] Y. Yu, G. Giuliani and S. Donati, *Measurement of the linewidth enhancement factor of semiconductor lasers based on the optical feedback self-mixing effect*, IEEE Photonics Technology Letters **16**, pp. 990 (2004).

[Yua02] Z. Yuan, B. E. Kardynal, R. M. Stevenson, A. J. Shields, C. J. Lobo, K. Cooper, N. S. Beattie, D. A. Ritchie and M. Pepper, *Electrically Driven Single-Photon Source*, Science **295**, pp. 102 (2002).

A Appendix

A.1 Semiclassical rate equation model

This model is based on the work of Christoph Redlich, Benjamin Lingnau and Kathy Lüdge. The description is taken and rephrased from [Hol18b].

Delayed optical feedback in the microlaser is theoretically described within the semiclassical four-variable rate equation model that was already successfully applied in [Red16]. Moreover, a quantum Langevin approach allows us to examine the microlaser system in the cQED weak coupling regime. Therefore, we set up a stochastic delay differential equation system (SDDE) for the bimodal complex electric fields $E_{\mathrm{s,w}}$ (SM and WM respectively), the occupation probability ρ of the active QDs and the reservoir carrier density n_{r}. In comparison to previous work delayed optical feedback is included in the differential equations by adding the term $-K_{\mathrm{j}}E_{\mathrm{j}}(t-\tau_{\mathrm{FB}})$ in the equation of the electric field.

$$\frac{d}{dt}E_{\mathrm{j}}(t) = \tfrac{1}{2}\tfrac{h\nu_0}{\epsilon_0\epsilon_{\mathrm{bg}}}\tfrac{2Z^{\mathrm{QD}}}{V}g_{\mathrm{j}}\left(1+i\alpha\right)\left[2\rho(t)-1\right]E_{\mathrm{j}}(t) - \kappa_{\mathrm{j}}\left(E_{\mathrm{j}}(t) - K_{\mathrm{j}}E_{\mathrm{j}}(t-\tau_{\mathrm{FB}})\right) + \sqrt{\tfrac{h\nu_0}{\epsilon_0\epsilon_{\mathrm{bg}}}\tfrac{2Z^{\mathrm{QD}}}{V}\beta\tfrac{\rho}{\tau_{\mathrm{sp}}}}\xi(t) \tag{A.1}$$

$$\frac{d}{dt}\rho(t) = -\sum_{\mathrm{j}\in\{\mathrm{sw}\}} g_{\mathrm{j}}[2\rho(t)-1]|E_{\mathrm{j}}(t)|^2 - \frac{\rho(t)}{\tau_{\mathrm{sp}}} + S^{\mathrm{in}}n_{\mathrm{r}}(t)[1-\rho(t)] \tag{A.2}$$

$$\frac{d}{dt}n_r(t) = \tfrac{\eta}{e_0 A}(I-I_p) - S^{\mathrm{in}}n_{\mathrm{r}}(t)\tfrac{2}{A}Z^{\mathrm{QD}}[1-\rho(t)] - S^{\mathrm{in}}\tfrac{2}{A}Z^{\mathrm{inac}}\frac{\rho^{\mathrm{inac}}}{\tau_{\mathrm{sp}}} - \frac{n_{\mathrm{r}}(t)}{\tau_{\mathrm{r}}} \tag{A.3}$$

$$\text{with } g_{\mathrm{j}} = \tfrac{|\mu_{\mathrm{j}}|^2 T_2}{2\hbar^2}\left(1+\varepsilon_{\mathrm{js}}\tilde{\epsilon}|E_{\mathrm{s}}(t)|^2 + \varepsilon_{\mathrm{jw}}\tilde{\epsilon}|E_{\mathrm{w}}(t)|^2\right)^{-1} \tag{A.4}$$

The electric field optical losses $\kappa_{\mathrm{s,w}}$ can be extracted from the experimentally measured cavity quality factor $Q_{\mathrm{s,w}}$ using $\kappa_{\mathrm{s,w}} = (\pi\nu_0)/Q_{\mathrm{s,w}}$ where ν_0 denotes the center frequency of the free running laser that is determined from the experiment.

A phenomenological linewidth enhancement factor with a value of α is introduced in the equations of both electric field modes.

In contrast to conventional semiconductor lasers which show large mode volumes V, the low mode-volume microlaser exibits cQED enhanced light-matter coupling that is taken into account by using stochastic spontaneous emission noise with a Purcell-shortened spontaneous emission lifetime τ_{sp} within one QD (compared to about a typical QD lifetime of about 1 ns in bulk) and the spontaneous coupling factor β. The value of β is extracted from fitting of both modes of the experimental input-output curve. The mode interaction is modeled using a gain compression factor of the form $g_{\mathrm{j}} \sim (1 + \epsilon_{\mathrm{js}}\tilde{\epsilon}|E_{\mathrm{s}}|^2 + \epsilon_{\mathrm{jw}}\tilde{\epsilon}|E_{\mathrm{w}}|^2)^{-1}$. The gain-compression factors are iteratively adjusted to yield best possible quantitative agreement with the experimental data, thus taking into account the mode splitting that is not specifically defined in the equations. Those factors are crucial when examining the interplay of SM and WM and therefore defining the shape of the bimodal emission characteristics. The inversion $(2\rho - 1)$ is determined by losses from the stimulated emission process, proportional to $\sum_{\mathrm{j}} g_{\mathrm{j}}(2\rho-1)|E_{\mathrm{j}}|^2$, spontaneous emission losses $\frac{\rho}{\tau_{\mathrm{sp}}}$ and effective in-scattering $S^{\mathrm{in}}n_{\mathrm{r}}(1-\rho)$ from the effective reservoir carrier density n_{r}, where one accounts for Pauli-blocking using the term $(1-\rho)$. The effective in-scattering rate S^{in} can be extracted from measurements of the relaxation oscillations of the microlaser under small-amplitude short optical perturbations. These rates can also be calculated from a microscopic computation of the Coulomb interaction between the carrier reservoir of the wetting layer and the QD [Lüd12] when no experimental data is available.

One assumes a typical densities of QDs in such materials of $n_{\mathrm{QD}} = 5 \cdot 10^9\,\mathrm{cm}^{-2}$. Using the given spatial and spectral overlap with the fundamental cavity mode, we can calculate the number of QDs Z^{QD} contributing actively to describe the mode area of A [Gér98]. The Z^{inac} inactive QDs are not resonant to the cavity mode, but have to be taken into account as they still capture carriers from the reservoir. The carrier reservoir is electrically pumped by the excitation current I. A pump efficiency η and a parasitic current I_{p} have to be included in the model, as one has to take care of the fact that several microlasers are coupled via a common current bar of the electrically pumped sample. Moreover, we include reservoir losses with a decay term $-n_{\mathrm{r}}/\tau_{\mathrm{r}}$, where the carrier life time τ_{r} is fixed to 1 ns.

A.2 Quantum optical model

This model is based on the work of Brett H. Hokr and Weng W. Chow. The description is taken and rephrased from [Hol18a].

The quantum optica model to determine α can be derived in the Heisenberg picture using a cluster expansion method. This way a closed set of equations of motion is obtained for the polarization p, photon population n_{p} and electron (hole) carrier population $n_{\mathrm{e}}(n_{\mathrm{h}})$ [Cho13, Cho14]. The linewidth enhancement factor can be extracted from calculating the gain and carrier-induced refractive spectra. One yields the amplitude gain $g(\omega)$ and carrier-induced refractive index $\delta n(\omega)$ for a QW layer embedded with QDs from the interband polarization $p_{\mathrm{ij}}(\omega)$:

$$K\delta n(\omega) + ig(\omega) = -\frac{\omega}{\varepsilon_0 n_{\mathrm{bg}} c w_{\mathrm{QW}} E(\omega)} \sum_{\mathrm{i,j}} \mu_{\mathrm{ij}} p_{\mathrm{ij}}(\omega) \tag{A.5}$$

where i,j denote the discrete and continuous labels for QD and QW states respectively, c and ε_0 stand for the speed of light and permittivity in vacuum, n_{bg} is the refractive index of the background medium (GaAs), K represents the laser field wavevector, w_{QW} is the width of the QW width embedding a sheet QD density of N_{dot}, $E(\omega)$ expresses a weak laser probe field at frequency ω. Moreover, the summations are carried out over all possible electron-hole QD and QW transitions.

In order to retrieve the polarization one has to solve the following equation of motion

$$\frac{d}{dt} p_{\mathrm{ij}} = i\omega_{\mathrm{ij}} p_{\mathrm{ij}} + i\Omega_{\mathrm{ij}}(1 - n_{\mathrm{i}}^{\mathrm{e}} - n_{\mathrm{j}}^{\mathrm{h}}) + S_{\mathrm{ij}}^{\mathrm{c-c}} + S_{\mathrm{ij}}^{\mathrm{c-p}} \ , \tag{A.6}$$

where ω_{ij} and Ω_{ij} denote the renormalized transition and Rabi frequencies , $n_{\mathrm{i}}^{\mathrm{e}}$ and $n_{\mathrm{j}}^{\mathrm{h}}$ represent the electron and hole populations in states i and j. One can describe the dephasing contributions due to carrier-carrier and carrier-phonon scatterings by the complex terms $S_{\mathrm{ij}}^{\mathrm{c-c}}(\omega)$ and $S_{\mathrm{ij}}^{\mathrm{c-p}}(\omega)$, respectively. Further details with in depth derivation and evaluation of these equations are found in previous publications [Cho13]. To finally determine α, one has to apply the steady-state solution of Eq. A.6 to Eq. A.5. It is underlined that the microlaser sample exhibits dimensional or alloy fluctuations. These can be taken into account with a statistical average over a range of band-gap energies assuming a weighting described by a normal distribution. Therefore, we introduced an inhomogeneous broadening $\Delta_{\mathrm{inh}} \simeq 30\,\mathrm{meV}$.

A.3 Sample overview

Table A.1 provides an overview of the parameters of the microlaser samples used in this thesis. Here both the investigated diameter $\varnothing_{\text{investigated}}$ and the generally available diameters $\varnothing_{\text{available}}$ on the sample piece are depicted.

Sample parameters				
Microlaser	Wafer	Part	$\varnothing_{\text{investigated}}$ (µm)	$\varnothing_{\text{available}}$ (µm)
A	M2977	21.15	4	2, 3, 4, 5
B	M4072	11.6	3.8	2 to 5.7
C	M2977	15.11	2, 3, 4, **5**	2, 3, 4, 5
D	M2977	21.15	5	2, 3, 4, 5

Table A.1: Table of microlasers investigated in this thesis. The samples of microlasers A, C and D exhibit multiple microlasers of the same diameter (60 for part 15.11 and 120 for part 21.15), while the sample of microlaser B has only 2 microlasers of the same diameter with diameters increasing in steps of 0.02 µm.

The exact layer structure of the samples is discussed in section 3.1. In particular, compare Fig. 3.1 for more details.

Acknowledgments

Hereby I would like to express my gratitude to everyone who were involved in helping me to successfully complete this work. I particularly would like to thank:

Prof. Dr. Stephan Reitzenstein for accepting me in his working group of outstanding researchers. He has given me the opportunity to investigate a both very interesting and challenging topic at the crossroads of quantum optics and nonlinear dynamics. Moreover, I would like to thank him for the enjoyable and open working environment as well as all the great support throughout the whole project.

Prof. Dr. Gian Luca Lippi and *Prof. Dr. Michael Lehmann* for taking on the duties of the second referee and chairmanship of this thesis.

Dr. Xavier Porte and *Dr. Janik Wolters* for their engaging support both in designing and carrying out the experiments. I would like to thank both my postdocs for always being available for fruitful and informative discussions. The friendly and informal atmosphere really made working with them very pleasant.

The members of the ERC team *Elisabeth Schlottmann*, *Sören Kreinberg* and *Arsenty Kaganskiy* for our collaborative effort in building the setup and writing the software. Furthermore, I am grateful for various fruitful discussions and the great support in our shared publications.

Our colleagues from the department of theoretical physics for the excellent numerical discription of the experimental data which gave significant insights into the underlying nonlinear dynamics: *Christoph Redlich*, *Dr. Benjamin Lingnau* and *Prof. Dr. Kathy Lüdge*.

My master and bachelor students *Milo Sommer* and *Ramtin Dastgheib Shirazi* for supporting me in various measurements.

The colleagues from University of Würzburg for providing samples of outstanding quality: *Monika Emmerling*, *Dr. Christian Schneider* and *Prof. Dr. Sven Höfling*.

Dr. Jörn Beyer from Physikalisch-Technische Bundesanstalt for providing state-of-the-art photon-number resolving detectors that gave insights beyond optical and statistical properties of the investigated samples.

All current and previous colleagues from the working group for various things: *Prof. Dr. Udo Pohl, Dr. Tobias Heindel, Dr. Anna Musial, Dr. Sven Rodt, Dr. Samir Bounouar, Dr. Kaisa Laiho, Dr. Pawel Mrowinski, Fabian Gericke, Pierce Munnelly, Marco Schmidt, Martin von Hellversen, Dr. Max Strauß, Ronny Schmidt, Dr. Caspar Hopfmann, Dr. Alexander Schlehahn, Dr. Alexander Thoma, Matthias Karow, Peter Schnauber, Esra Tauscher, Stefan Jagsch, Sarah Fischbach, Jan Große, Tobias Heuser, Nicole Srocka, Felix Krüger, Lucas Rickert, TImm Kupko, Marcel Hohn and Lucas Bremer.*

The colleagues from the mechanical workshop for always being helpful and providing key components for the experimental setup.

Prof. Dr. Stephan Reitzenstein and *Dr. Xavier Porte* for proof-reading and corrections to this manuscript. I am very thankful for the helpful comments and the constructive feedback.

A special thanks goes to my family who have always supported me in this long journey towards this dissertation. Especially, I want to thank my girlfriend *Branka Vukomanović* who always supported and encouraged me during the time of writing this thesis. I would also like to thank all my friends I made in the working group and during my stay in Berlin and everyone I may have forgotten on this list.

List of publications

Conference and journal publications that are relevant for this work are listed in the following. My own contribution is indicated according to §2 (4) Promotionsordnung of the Faculty II of the Technische Universität Berlin.

Peer reviewed journals

- E. Schlottmann, S. Holzinger*, B. Lingnau, K. Lüdge, C. Schneider, M. Kamp, S. Höfling, J. Wolters, and S. Reitzenstein, *Injection Locking of Quantum-Dot Microlasers Operating in the Few-Photon Regime*, Physical Review Applied **6**, p. 044023 (2016).
  *E.S. and S.H. contributed equally to this publication
  Own contribution: Experimental setup and realization, data analysis, discussion and presentation of experimental results.

- S. Holzinger, C. Redlich, B. Lingnau, M. Schmidt, M. von Helversen, J. Beyer, C. Schneider, M. Kamp, S. Höfling, K. Lüdge, X. Porte, and S. Reitzenstein, *Tailoring the mode-switching dynamics in quantum-dot micropillar lasers via time-delayed optical feedback*, Opt. Express **26**(17), pp. 22457 (2018).
  Own contribution: Experimental setup and realization, data analysis, discussion and presentation of experimental results.

- S. Holzinger, S. Kreinberg, B. H. Hokr, C. Schneider, S. Höfling, W. W. Chow, X. Porte, and S. Reitzenstein, *Determining the linewidth enhancement factor via optical feedback in quantum dot micropillar lasers*, Optics Express **26**(24), pp. 31363 (2018).
  Own contribution: Experimental setup and realization, data analysis, discussion and presentation of experimental results.

- S. Holzinger, C. Schneider, S. Höfling, X. Porte, and S. Reitzenstein, *Quantum-dot micropillar lasers subject to coherent time-delayed optical feedback from a short external cavity*, Scientific Reports **9**(1), pp. 631 (2019).
  Own contribution: Experimental setup and realization, data analysis, discussion and presentation of experimental results.

- C. Redlich, B. Lingnau, S. Holzinger, E. Schlottmann, S. Kreinberg, C. Schneider, M. Kamp, S. Höfling, J. Wolters, S. Reitzenstein, and K. Lüdge, *Mode-switching induced super-thermal bunching in quantum-dot microlasers*, New Journal of Physics **18**, 063011 (2016).
  Own contribution: Experimental setup and realization, data analysis, discussion and presentation of experimental results.

Conference presentation and posters

- S. Holzinger, E. Schlottmann, S. Kreinberg, M. Strauß, C. Schneider, S. Höfling, J. Wolters, M. Kamp, and S. Reitzenstein, *Influence of optical feedback on the characteristics of quantum dot micropillar lasers*, DPG Spring Meeting 2015, Talk (HL 25.6) March 17th, Berlin (Germany).

- S. Holzinger, E. Schlottmann, B. Lingnau, K. Lüdge, C. Schneider, S. Höfling, M. Kamp, J. Wolters, and S. Reitzenstein, *Injection Locking in the Quantum Regime*, COST MP1403 NQO-ESR Workshop 2015, Talk November 17th, Attard (Malta).

- S. Holzinger, E. Schlottmann, B. Lingnau, K. Lüdge, C. Schneider, M. Kamp, S. Höfling, J. Wolters, and S. Reitzenstein, *Injection Locking in the Quantum Regime*, OPON 2016, Poster February 18th, Wrocław (Poland).

- S. Holzinger, E. Schlottmann, B. Lingnau, K. Lüdge, C. Schneider, S. Höfling, M. Kamp, J. Wolters, and S. Reitzenstein, *Injection Locking in the Quantum Regime*, DPG Spring Meeting 2016, Talk (DY 37.2) March 9th, Regensburg (Germany).

- S. Holzinger, E. Schlottmann, B. Lingnau, K. Lüdge, C. Schneider, S. Höfling, M. Kamp, J. Wolters, and S. Reitzenstein, *Injection Locking of High-β Quantum Dot Microlasers*, CLEO 2016, Talk June 10th, San Jose (USA).

- S. Holzinger, X. Porte, C. Redlich, B. Lingnau, K. Lüdge, C. Scheider, M. Kamp, S. Höfling and, S. Reitzenstein, *Quantum dot micropillar lasers subject to time-delayed optical feedback*, DPG Spring Meeting 2017, Talk (HL 10.5) March 20th, Dresden (Germany)

- S. Holzinger, X. Porte, C. Redlich, B. Lingnau, K. Lüdge, C. Scheider, M. Kamp, S. Höfling and, S. Reitzenstein, *Quantum dot micropillar lasers subject to time-delayed optical feedback*, CLEO/Europe-ECEQ 2017, Talk June 29th, Munich (Germany)

- S. Holzinger, C. Redlich, B. Lingnau, M. Schmidt, M. von Helversen, J. Beyer, C. Scheider, S. Höfling, M. Kamp, K. Lüdge, X. Porte, and, S. Reitzenstein, *Controlling switching dynamics in quantum-dot micropillar lasers with time-delayed optical feedback*, 20th International Winterschool on New Developments in Solid State Physics 2018, Poster February 28th, Mauterndorf (Austria)

- S. Holzinger, C. Redlich, B. Lingnau, M. Schmidt, M. von Helversen, J. Beyer, C. Scheider, M. Kamp, S. Höfling, K. Lüdge, X. Porte, and, S. Reitzenstein, *Controlling switching dynamics in quantum-dot micropillar lasers with time-delayed optical feedback*, DPG Spring Meeting 2018, Talk (HL 5.9) March 12th, Berlin (Germany)

- S. Holzinger, C. Redlich, B. Lingnau, M. Schmidt, M. von Helversen, J. Beyer, C. Scheider, M. Kamp, S. Höfling, K. Lüdge, X. Porte, and, S. Reitzenstein, *Controlling switching dynamics in quantum-dot micropillar lasers with time-delayed optical feedback*, NOEKS 14 (2018), Poster September 24th, Berlin (Germany)

Berlin, November 22, 2019

Steffen Holzinger

Declaration of authorship (Eidesstattliche Erklärung)

According to §5 (1) Promotionsordnung of the Technische Universität Berlin

I hereby declare that the thesis submitted is my own unaided work. All direct sources and aids used are acknowledged as references.
This dissertation was not previously presented to another examination board and has not been published.
All statements regarding the share of my work in shared authorships are correct (§2 (4)).

Gemäß §5 (1) der Promotionsordnung der Technischen Universität Berlin

Hiermit erkläre ich an Eides statt, dass ich die Dissertation selbstständig und ohne Hilfe eines Promotionsberaters angefertigt und keine anderen als die angegebenen Quellen und Hilfsmittel benutzt habe.
Die Arbeit wurde weder einer anderen Prüfungsbehörde vorgelegt noch veröffentlicht.
Die gemachten Angaben zum Eigenanteil an bestehenden Vorveröffentlichungen in Ko-Autorenschaft sind zutreffend (§2 (4)).

Berlin, November 22, 2019

Steffen Holzinger